Sensorless control of synchronous machines

Master thesis

Johan Palmstrøm Hald

Supervisor:

Roy Nilsen

Department of Electric Power Engineering

June 2020

NTNU

Norwegian University of
Science and Technology

Problem description

With the rapid increase in the proliferation of variable energy sources and rapid dismantling of fossil fuel-based energy sources, there is an increased demand for flexibility in the European power grid. Adjustable Speed Hydro (ASH) generation using synchronous machines coupled with pumped storage offers a high degree of dispatchable generation as well as a high efficiency.

In the specialisation project carried out during the fall of 2019, an investigation into the viability of using the naturally present high-frequency component of the field current as a means to run a synchronous machine with damper windings in sensorless operation was performed. The control scheme was successfully established

for low-speed and standstill operation with the stator converter disconnected.

In this master thesis, further investigation into the control method mentioned above will be performed.

The main focus of the thesis will be:

- An investigation into the stator response due to the high-frequency component of the field excitation current with the stator converter connected.
- Implementing a complete sensorless control methodology, with the self-sensing estimation scheme operating at standstill and in the low-speed region and the voltage model for higher speed operation.

Summary

As the European continent is seeing a rapid dismantling of dispatchable power generation, in favour of intermittent renewable energy sources such as wind and solar power, the need for flexibility in the continent's electrical grid is ever increasing. With this increased demand comes increased pressure on the Norwegian grid, as Norway's well-developed suite of hydropower installations is a highly sought after commodity. However, the continent's demand for flexibility far outstretches the available Norwegian resources. One way to cover this demand is the synergy of adjustable speed hydro (ASH) synchronous machines and pumped hydro.

For the combination of pumped hydro and ASH synchronous machines to work efficiently there is a need for a robust control system. The cutting-edge in control of electrical machines over the last decades has been sensorless control, wherein the position and speed of the rotor are estimated rather than measured. Offering higher reliability and robustness, in addition to lower costs and reduced system complexity, the future of electrical motor-drives is sensorless control.

In this Master thesis, which is a continuation of the specialization project done in the fall semester of 2019, a novel approach of sensorless control of a separately excited synchronous machine with damper windings is presented. The methodology utilizes additional excitation signals in the field current to detect the rotor position, in what is called the self-sensing method. The method has been combined with the already established estimation methods based on the generation of back-EMF, called the current and voltage model. Due to a lack of back-EMF information at standstill and low-speed operation, both the current and voltage model has insufficient available data to estimate the rotor position at standstill and low-speed operation accurately. Through an extensive investigation and analysis of the self-sensing method and various phase-locked loops combinations (PLL), it was shown that the model, being solely reliant on the additional field excitation signals and its response on the stator currents, drastically reduced the error at zero-crossing and low-speed for torque-controlled operation. While the gains achieved for torque-controlled operation is dependent on the acceleration of the rotor through zero-crossing, due to inherent limits in the PLL structure, the self-sensing model has been unequivocally shown to improve the sensorless control for standstill and low-speed operation.

The same improvements have been proven under speed-controlled operation where the introduction of the self-sensing model has shown a drastic increase in the sensorless control structure's ability to hold torques through zero-hold and -crossings, where comparative testing running only the current and voltage model showed complete system collapse.

Sammendrag

Med den drastiske økningen i utbytning av regulerbar kraftproduksjon til fordel for variable, fornybare energikilder som vind- og solkraft i fastlands Europa, er etterspørselen etter fleksibilitet i kraftnettet stadig økende. Med denne økende etterspørselen følger et stadig større press på det norske nettet, ettersom Norges velutviklede vannkraftressurser er en høyt etterspurt handelsvare. En måte å dekke denne etterspørselen på er koblingen av justerbar hastighetsdrift (ASH) synkronmaskiner og pumpekraftverk.

Effektiv kobling mellom pumpekraft og ASH synkronmaskiner avhenger av et robust kontrollsystem. Det fremste innen kontroll av elektriske maskiner som har kommet fram over de siste tiårene er sensorløs kontroll, hvor posisjonen og farten til rotoren blir estimert heller enn målt. Sensorløs kontroll lover en høyere pålitelighet og robusthet, i tillegg til reduserte kostnader og systemkompleksitet.

I denne masteroppgaven, som er en videreutvikling av spesialiseringsprosjektet utført høsten 2019, presenteres en metode for sensorløs kontroll av en separat eksitert synkronmaskin med dempeviklinger, som baserer seg på å bruke ekstra eksitasjonssignaler i feltstrømmen for å estimere rotorposisjonen, kalt ”self-sensing”-metoden. Metoden har blitt kombinert med allerede etablerte estimeringsmetoder basert på motindusert spenning, kalt strøm- og spenningsmodellen. Grunnet mangel av motindusert spenningsinformasjon ved stillstand og lave motorhastigheter har verken strøm- og spenningsmodellen nok tilgjengelig data for å nøyaktig estimere rotorposisjonen. Gjennom en omfattende analyse og undersøkelse ved bruken av de ekstra eksitasjonssignalene i feltstrømmen for posisjonsestimering og flere fase-låste løkker (PLL), har det blitt vist at modellen har drastisk redusert feilen i estimater ved stillstand og lave rotorhastigheter under momentkontroll.

Implementering av ”self-sensing”-metoden ved fartskontrollert drift har vist samme forbedring. Den overordnede kontrollstrukturens evne til å opprettholde moment ved stillstand og null-fartkrysninger har økt, mens strøm- og spenningsmodellen har resultert i systemkollaps ved sammeligningstester.

Preface

This Master thesis is done as a final evaluation of a master's degree in Energy and Environmental Engineering, submitted to the Department of Electrical Power Engineering at the Norwegian University of Science and Technology. The Master thesis has been a part of the HydroCen project.

The thesis has given me invaluable experience within a vast array of different fields, and will no doubt provide a solid foundation for the next frontier of professional life.

I would like to extend a heartfelt thank you to my supervisor Roy Nilsen, who has given me close guidance in the Master thesis and specialization project over the last year. His knowledge on everything motordrives related and willingness to share from his experience has consistently given me the exact answer I am looking for when all other options have been exhausted.

Trondheim, June 15, 2020

Johan Palmstrøm Hald

Table of Contents

Problem description i

Summary ii

Sammendrag iii

Preface iv

Table of Contents vii

List of Tables viii

List of Figures xi

Abbreviations and symbols xii

1 Introduction 2
1.1 Structure of thesis 4

2 Theory 5
2.1 Synchronous Machine 5
2.2 The physical model 6
2.3 Torque control 9

3 Simulation Model 11
3.1 Pulse width modulation 12
3.2 Moving average filters 13
3.3 Controllers 13

4 Identification 14
4.1 Voltage model 14
4.2 Current model 15

4.3 Self sensing . . . 16
4.3.1 Self-sensing results . . . 18
4.3.2 Phase-locked loop . . . 21
4.3.3 Atan2-based phase-locked loop . . . 26

5 Stator converter reconnected **30**

6 Self-sensing and voltage model combination **32**
6.1 Motivation for combining the self-sensing and voltage model . . . 32
6.2 Stator flux linkage estimate by self-sensing method . . . 32
6.3 Discretization . . . 33
6.4 Tuning . . . 34
6.5 Results . . . 37
6.5.1 Low-speed and standstill operation . . . 37
6.5.2 Speed traversal . . . 40
6.6 Second-order lowpass filter . . . 43
6.6.1 Results . . . 45

7 Self-sensing, current and voltage model combination **48**
7.1 Speed dependent gain . . . 48
7.1.1 Results . . . 49
7.2 PLL alternatives . . . 52
7.3 MAF-PLL . . . 53
7.3.1 D-partition technique . . . 54
7.3.2 Speed traversal . . . 56
7.4 Re-calibration of self-sensing model and new method for improved zero-crossing estimation . . . 58
7.5 Finalized results for torque-controlled operation . . . 61

8 Sensorless operation under speed control **68**
8.1 Tuning of speed controller . . . 68
8.2 Results . . . 70
8.2.1 Speed-controlled operation under no-load conditions . . . 70
8.2.2 Speed-controlled operation under load conditions . . . 72

9 Discussion **75**

10 Conclusion and further work **80**
10.1 Conclusion . . . 80
10.2 Recommendation for further work . . . 81

Bibliography **81**

A Machine parameters **85**

B Measured and estimated electric angles at standstill **86**

C Simulink bandpass filters **87**

D Closed loop PLL **89**

E SRF-PLL results **90**

F Alternative pu-model **93**

G Discretisation **95**

H Self-sensing method for stator flux estimation **97**

I RMSD **98**

J Sensorless control under speed traversal utilising the voltage-current model combination **100**

K Speed Dependent Gain **102**

L Dual phase-locked loop **103**

M Moving Average Filter **104**

N Bandwidth as a function of controller parameters calculated using the D-partitioning technique **105**

O Finalized design **106**

List of Tables

3.1 Controller parameters, retrieved from [1] 13

4.1 PLL PI controller values from symmetric optimum 25
4.2 Closed loop PLL transfer function results for SRF-PLL 26
4.3 PLL PI controller values for atan2 based SRF-PLL 27
4.4 Closed loop PLL transfer function results for atan2 based SRF-PLL . . . 29

6.1 Feedback PI-controller and PLL PI controller values for atan2 based SRF-PLL with 1nd order LPF 36
6.2 Feedback PI-controller and PLL PI controller values for atan2 based SRF-PLL with 2nd order LPF 44

7.1 MAF-PLL values 57
7.2 Summarized self-sensing model parameters 61

8.1 Speed controller parameters 70

A.1 Machine parameters 85

C.1 Bandpass filter transfer functions for the self-sensing model 87

G.1 Discretised transfer functions for the self-sensing model 95

I.1 RMSD calculations for estimated stator flux linkage and position with varying time constant and gain. $\beta = 4/T_f = 10$ 98
I.2 RMSD calculations for estimated stator flux linkage and position with varying β-value and lowpass-filter time constant. $P = 20/I = 0.01$ . . . 98
I.3 RMSD calculations for estimated stator flux linkage and position with varying time constant and gain. $\beta = 20/T_f$=1/(2π10) 99

List of Figures

2.1 Synchronous machine with damper windings. Reprinted from Electric Drives p.134, by [2] 6
2.2 Scheme for calculating current reference for maximum torque per ampere. Reproduced from [3] 10

3.1 Simulink model. Reproduced from [3] 11

4.1 Phasor diagram showing the relation between ψ_s, i_s, dq-coordinate system and the a-phase. Reproduced from [3] 15
4.2 Rotor position, high-frequency rotor current and stator responses in the α-β frame. Reproduced from [3] 18
4.3 Measured and estimated electrical angle, with damper windings [rad]. Reproduced from [3] 20
4.4 Electric measured and estimated electric angles, with the inclusion of damper windings [rad]. Reproduced from [3] 21
4.5 Basic PLL. Adapted from [4] 22
4.6 Established rotor position evaluation by a PLL. Source: adapted from [5] 23
4.7 Estimated/measured electric angles. Bandwidth=0.21 Hz, ζ=0.707 24
4.8 Estimated/measured electric angles. Bandwidth=105.74 Hz, ζ=0.707 . . . 24
4.9 Measured and PLL estimated electrical angle. Reproduced from [3] . . . 25
4.10 Block diagram for atan2 function in conjunction with SRF-PLL for position estimation 26
4.11 Estimated electric angle using atan2 function in conjunction with SRF-PLL and measured electric angle, with an applied torque reference of 0.01 pu. 27
4.12 Estimated electrical angle, with lock-on response 28
4.13 Estimated electric angle using atan2 function in conjunction with SRF-PLL and measured electric angle, with variable torque reference. 29

5.1 Stator currents in alpha-direction. From top to bottom: nominal, high-frequency and demodulated. 31

5.2 Measured and estimated electric angle, with estimated angle error 31

6.1 The voltage self-sensing model. Adapted from [6] 34
6.2 Sensorless control with voltage and self-sensing model combination, at low-speed operation 37
6.3 Sensorless control with voltage and current model combination, at low-speed operation 37
6.4 Calculated $i_{s,ref}$ from self-sensing and voltage model combination 38
6.5 Calculated $i_{s,ref}$ current and voltage model combination 38
6.6 Stator flux linkage and position error under sensorless control utilising the voltage and self-sensing model combination, at standstill operation 39
6.7 Stator flux linkage and position error under sensorless control utilising the voltage and current model combination, at standstill operation 39
6.8 Sensorless operation with varying applied torque reference 40
6.9 Step responses for closed loop PLL, with varying lowpass filter cut-off frequency 42
6.10 Sensorless operation with voltage model and self-sensing method combination after re-tuning. Torque reference of 0.01 pu 45
6.11 Sensorless operation with varying applied torque reference, after re-tuning 46

7.1 Sensorless operation with voltage, current and self-sensing model. Torque reference of 0.01 pu 49
7.2 Sensorless operation with varying applied torque reference for wide speed range operation, self-sensing, voltage and current model combination . . 51
7.3 Calculated PI-controller parameters by Neimarks D-partition method . . . 55
7.4 PLL bandwidth as a function of K_p and K_1, calculated using the D-partitioning technique 56
7.5 Sine of i_f based MAF-PLL, with and without phase-shift, and output when corrected by RMSD calculation 60
7.6 Stator flux linkage and position error under sensorless control utilising the self-sensing, current and voltage model for varying steps in torque 62
7.7 Stator flux linkage and position error under sensorless control utilising the current and voltage model for varying steps in torque 62
7.8 Stator flux linkage and position error under sensorless control utilising the self-sensing, current and voltage model for varying steps in torque, with hand-off procedure dependent of the slope of the speed 65
7.9 Sensorless operation with the SSCMVM combination, with the synchronization failure fixed under torque-controlled operation 66

8.1 PLL bandwidth as a function of K_p and K_i, calculated using the D-partitioning technique for the speed-controller 69
8.2 Sensorless operation with varying speed reference for the self-sensing, voltage and current model combination, under speed-controlled conditions and no-load 71

8.3 Sensorless operation with varying speed reference for the self-sensing, voltage and current model combination, under speed-controlled conditions and applied torque of 0.8 pu 73

B.1 Measured and estimated electric angles [rad] 86

C.1 Magnitude and phase response: Bandpass filter for $i_{s\alpha}$ and $i_{s\beta}$ 88
C.2 Magnitude and phase response: Bandpass filter for i_f 88

D.1 Root locus plot of closed loop PLL transfer function 89

E.1 Measured and estimated electric angles. Torque reference of 0.09 pu . . . 90
E.2 Measured and estimated electric angles. Torque reference of 0.01 pu . . . 91
E.3 Measured and estimated electric angles. Torque reference of 0.11 pu . . . 91
E.4 Measured and estimated electric angles. Torque reference of 1 pu 92

G.1 Magnitude and phase response: Discrete bandpass filter for $i_{s\alpha}$ and $i_{s\beta}$ . . 96
G.2 Magnitude and phase response: Discrete bandpass filter for i_f 96

H.1 Model for estimation of stator flux linkage using the self-sensing methodology 97

J.1 Sensorless operation with low magnitude varying applied torque reference, voltage-current model combination 100
J.2 Sensorless operation with varying applied torque reference for wide speed range operation, voltage-current model combination 101

K.1 Block diagram of hand-off procedure from self-sensing to current model, where $\hat{n}$ denotes estimated speed and n_{ho} the hand-off speed from the self-sensing to current model 102

L.1 Dual phase-locked loop. Adapted from [7] 103

M.1 Moving Average Filter. Adapted from [8] 104

N.1 Bandwidth as a function of controller parameters for FOLPF-PLL, calculated using the D-partitioning technique 105
N.2 Bandwidth as a function of controller parameters for SOLPF-PLL, calculated using the D-partitioning technique 105

O.1 Block diagram for the MAF-PLL which solves the desynchronization error at speed zero crossing 106
O.2 Block diagram for the full sensing-model estimation methodology 107
O.3 Block diagram for self-sensing, current and voltage model combination, with the speed-dependent gain and speed derivative hand-off procedure . 107

Abbreviations and symbols

Symbols

a	=	phase a
b	=	phase b
c	=	phase c
d	=	Two phase axis (rotating)
I	=	Current [A]
i	=	Current [pu]
J	=	Moment of intertia [kgm^2]
K	=	Gain [-]
k	=	Torque constant [-]
L	=	Inductance [H]
M	=	Torque [Nm]
M	=	Modulation ratio [-]
n	=	speed [rpm]
p	=	number of poles
q	=	Two phase axis (rotating)
R	=	Resistance [Ω]
r	=	Resistance [pu]
T	=	Time constant [s]
U	=	Voltage [V]
u	=	Voltage [pu]
X	=	Reactance [Ω]
x	=	Reactance [pu]
α	=	Two phase axis (static)
β	=	Two phase axis (static)
κ_{rs}	=	Rotor to stator ratio
Ψ	=	Flux linkage [Wb]
ω	=	Angular velocity [rad/s]
τ_e	=	Electromagnetic torque [pu]
τ_l	=	Load torque [pu]
θ	=	Angle [rad / $^\circ$]
ζ	=	Relative damping [-]

Abbreviations

EMF	Electromotive force
MAF	Moving-average filter
PLL	Phase-locked loop
SRF	Synchronous reference frame
CMVM	Current model and voltage model
SSCMVM	Self-sensing, current model and voltage model

Subscript

a	=	Phase a
a	=	armature
avg	=	Average
b	=	Phase b
c	=	Phase c
D	=	Damper winding aligned along rotor
dc	=	DC current / voltage
d	=	d axis
e	=	Electric
f	=	Field
i	=	High-frequency component
l	=	Load
mech	=	Mechanical
n	=	Rated value
ol	=	Open loop
Q	=	Damper winding perpendicular to rotor
q	=	q axis
r	=	Rotor
ref	=	reference
s	=	Stator
tri	=	Triangular
0	=	Common mode component
α	=	See symbols
β	=	See symbols
σ	=	leakage

Chapter 1

Introduction

The world is in an era of unprecedented change. With the effects of global climate change rapidly becoming one of the most substantial issues facing an increasingly interconnected society, the need for clean, renewable energy is surging. Norway has long lead the charge in the deployment of renewable energy, in the form of large-scale hydropower installation. The focus on hydropower over other energy production technologies has ensured energy independence consisting solely of renewable power, virtually unrivalled on the global stage. However, an increased interconnection of the European and Norwegian power systems via subsea cables means that changes in continental Europe's energy production and consumption will cause a reaction in the Norwegian power system. There has been a clear trend in the last decade in the replacement of traditional fossil-based energy, with variable, renewable energy sources, such as wind and solar. The shift from dispatchable power generation in the form of coal- and gas plants, to intermittent renewable energy sources, has lead to a marked increase in Europe's demand for flexibility. The concept of flexibility as a commodity is a relatively new idea, with marketplaces for trading in flexibility just starting to emerge. An oft-cited idea is to utilize the inherent dispatchability of Norwegian hydropower to cover the growing demand for flexibility, in what has been called Europe's green battery.

However, Europe's demand for flexibility is significantly higher than the available supply in developed hydropower installations in Norway. With most of the economically and regulatory available resources for hydropower already developed, other avenues of attack must be considered. According to Lia et al. the theoretical upgrading potential of existing Norwegian hydropower is in the range of 22 and 30 TWh/year, notwithstanding environmental and political issues which may serve to reduce this estimate [9].

There are several options to increase the efficiency of hydropower plants. One possible solution is the synergy of adjustable speed hydro (ASH) machines and pumped hydro. ASH enables power stations to operate at optimal system efficiency in a range of different combinations of head and inflow, by allowing for a change in machine speed accordingly. According to Gjengedal, among the potential benefits of implementing ASH are increased

efficiency, reserve capacity as well as improved capability of load following [10].

In addition to the benefits described above, ASH is highly useful in conjunction with pumped hydro. Pumped hydro allows for the storage of surplus energy in the power grid by recharging hydropower reservoirs using a reversible turbine/generator aggregate, at times when the power supply is greater than the demand. As a result, hydropower plants can achieve a substantially higher utilization factor without the need for large-scale expansion. In a turbine/generator aggregate, the norm has been to design the system for optimal operation in pump mode. As a result, system efficiency is sub-optimal when running in generator mode. By the usage of ASH technology, the need for fixed speed operation is negated, drastically increasing the overall system efficiency.

For an optimal implementation of ASH combined with pumped hydro to materialize, there is a need for a robust control system. Sensorless control of electrical machines has over the last decades become the cutting-edge of electric drives. Traditionally, conventional speed and position sensors such as tachometers and encoders have provided the required inputs to a given control system for electrical drives. Although these technologies have a proven track record and are well established on the market, there are several disadvantages with their inclusion in electric drives. As discussed in the relevant literature, conventional sensors are known to increase system costs as well as decrease the overall system reliability [11–13].

As a result of the challenges above, there has been significant research into sensorless control, wherein the rotor speed and position are estimated rather than measured. At present, the state-of-art concerning sensorless control is mainly centred on two primary methods; estimation based on information from the back-EMF (electromotive force) and high-frequency signal injection [14, 15].

The estimation method utilizing information provided by the back-EMF is well suited for machines operating in the medium to high-speed region. However, the technique is unsuited for operation at standstill and low speeds due to insufficient generation of back-EMF and a subsequent lack of information [15].
Estimation of speed and rotor position utilizing the high-frequency signal injection method is not dependent on back-EMF, as the method require the generation of an ancillary signal. Consequently, this estimation scheme is widely used for standstill and low-speed operation. However, due to the injected high-frequency signal, the method is known to cause increased torque ripple, acoustic noise and decreased efficiency [5, 14, 15].

In this master thesis, a sensorless control strategy will be implemented for a separately excited synchronous machine with damper windings. As opposed to permanent magnet synchronous machines (PMSM), the magnetic field in the rotor is established by feeding an excitation current to the rotor coil. The presence of the field winding results in an additional degree of freedom concerning possible sensorless control methods, due to the magnetic coupling between rotor field winding and stator.

This magnetic coupling can be exploited, as in [5] where the authors note that changes

in the d-axis field excitation current, generates a response in the stator winding currents. The response caused by the field excitation current can subsequently be used to estimate rotor position and speed, facilitating for sensorless control. In other words, the method takes advantage of the fact that the separately excited synchronous machines, in essence, resembles a resolver, another commonly used position sensor. A similar approach for estimating the control parameters was investigated by Alakula in [16]. The approach for sensorless control described above is commonly referred to as self-sensing control, which has the advantage over the high-frequency signal injection method in that it utilizes naturally occurring signals in the machine, negating the adverse effects of increased torque ripple, noise and reduction in system efficiency.

This Master thesis aims to present a sensorless control strategy, with the novel technique of utilizing the additional excitation signals in the field current for standstill and low-speed operation, in what is known as the self-sensing model. As far as the author is aware, this method has never been attempted implemented for a separately excited synchronous machine with damper windings.

1.1 Structure of thesis

The Master thesis first details a brief introduction to the theory of the most significance to electric motordrives. Secondly, a brief overview of the Simulink model used throughout the present thesis is given, explaining the systems and techniques most pertinent to the simulations. An introduction into the three identification techniques used for position estimation is subsequently explored, with the most emphasis on the self-sensing model.

A brief recap of the most significant findings from the project thesis, in addition to a more detailed explanation of the PLL methodology, is then given.

The next part is a detailed investigation into the viability of using the additional field excitation signal method, first only working in unison with the voltage model and secondly with the self-sensing, current and voltage model all combined. As significant effort has been exerted concerning the PLL and self-sensing model, with new drive testing underway in the thesis continually exposing flaws with the previous iteration, relevant theory and discussion are provided throughout the thesis where relevant. Further discussion is provided in a separate chapter wherein the potential limitations of the present study are provided. Finally, the conclusion and recommendations for further work are presented.

Chapter 2

Theory

In this section, an introduction of the electrical machine investigated in the Master thesis is presented, including relevant theory. As the theory used in the Master thesis is the same as for the specialization project, the section is an adapted and revised version from [3].

2.1 Synchronous Machine

As mentioned in chapter 1, the machine on which the sensorless control will be implemented is a three-phase separately excited synchronous machine with damper windings. The machine contains a total of five windings wherein three are located in the stator, and two in the rotor, as depicted in Figure 2.1.

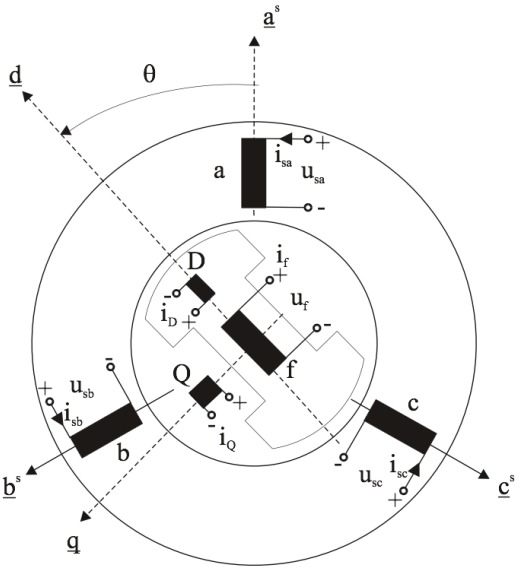

Figure 2.1: Synchronous machine with damper windings. Reprinted from Electric Drives p.134, by [2]

The stator windings are excited by a three-phase, two-level pulse width modulation (PWM) controlled inverter. The supplied three-phase sinusoidal voltages are symmetrical and displaced by 120°. The field winding is electrically excited by an external full-bridge PWM-controlled converter, which supplies DC to the winding through the use of slip-rings. The damper winding consists of short-circuited copper bars, and function similar to the squirrel cage in induction machines. The damper winding serves to dampen out any sudden oscillatory behaviour of the rotor due to sudden load changes when the machine is in synchronicity. Similarly to the squirrel cage, the winding also provides a starting torque for the machine when operating as a motor, as the synchronous machine is not self-starting.

As shown in Figure 2.1 the damper winding is represented by one winding in the direction of the field circuit's winding-axis and one perpendicular to the axis, denoted as D and Q respectively.

In addition to the three-phase abc-axis system, a new coordinate system is present in Figure 2.1. Called the direct-quadrature reference frame, this system is affixed to the rotor aligned along the peak of the field winding flux. By transforming the actual windings in the static abc-reference frame to the rotating dq-coordinate system, all currents and voltages are made to DC-quantities, which serves to simplify the control of the machine.

2.2 The physical model

The expression for the voltage induced by the flux in a given winding in the synchronous machine can be expressed as shown in Equation 2.1.

$$U = R \cdot I + \frac{d\Psi}{dt} \tag{2.1}$$

From left to right, the voltage across a given winding is given by the sum of the voltage drop in the winding and the induced electromotive force (emf). The flux linkage, Ψ, is given by Equation 2.2.

$$\Psi = L \cdot I \tag{2.2}$$

Utilising the co-energy concept as presented in [2, 17], a dynamic model for the three-phase, separately excited synchronous machine can be obtained. The voltage balance for the rotor, stator and damper windings are shown in Equation 2.3 to Equation 2.8.

$$U_{sa} = R_s \cdot I_{sa} + \frac{d\Psi_{sa}}{dt} \tag{2.3}$$

$$U_f = R_f \cdot I_f + \frac{d\Psi_f}{dt} \tag{2.4}$$

$$U_{sb} = R_s \cdot I_{sb} + \frac{d\Psi_{sb}}{dt} \tag{2.5}$$

$$0 = R_D \cdot I_D + \frac{d\Psi_D}{dt} \tag{2.6}$$

$$U_{sc} = R_s \cdot I_{sc} + \frac{d\Psi_{sc}}{dt} \tag{2.7}$$

$$0 = R_Q \cdot I_Q + \frac{d\Psi_Q}{dt} \tag{2.8}$$

As discussed in section 2.1, the damper winding is realised as two short-circuited copper bars, culminating in no voltage drop across the winding and $U_D = U_Q = 0$.

As shown in Equation 2.2, the flux linkage of the windings are dependent on current and inductance, where the inductance consists of both self- and mutual inductance between the windings.

Due to the non-uniform air-gap in a salient pole machine, the mutual inductances between rotor and stator are dependent on the position of the rotor, which in turn means that the flux linkages are dependent on rotor position. By the usage of the Park-transformation, in which the stationary, three-phase abc coordinate system is made into a rotating, two-phase direct-quadrature (dq) reference frame, the effect of periodic changes in saliency and rotor position are negated, and the flux linkages become independent of time. As a result, vector control of the machine, which will be employed in this thesis, is massively simplified.

Defining θ as the angle between the rotor and phase a, i.e. the position of the rotor, the transformation matrix is given by Equation 2.9.

$$T_{ss}^{r} = \frac{2}{3} \begin{bmatrix} \cos(\theta) & cos(\theta - \frac{2\pi}{3} & cos(\theta - \frac{4\pi}{3}) \\ -\sin(\theta) & -\sin(\theta - \frac{2\pi}{3}) & \sin(\theta - \frac{4\pi}{3}) \end{bmatrix} \tag{2.9}$$

The factor $2/3$ is utilised to scale the amplitude of the coordinate vector to be equal to the amplitude of the phase current. Furthermore, it is assumed that the phase currents sum to zero which is the case for a healthy machine, and as such the zero-sequence has been omitted.

Utilising the transformation matrix, the currents in the dq-reference frame is obtained by Equation 2.10.

$$I_{dq} = T_{ss}^{r} \cdot I \tag{2.10}$$

Finally, the voltage balance in the dq-reference frame in per-unit values is obtained by the transformation matrix, as well as dividing all parameters with chosen basis, and is shown in Equation 2.11 through 2.16.

$$u_d = r_s \cdot i_d + \frac{1}{\omega_n}\frac{d\psi_d}{dt} - n \cdot \psi_q \tag{2.11}$$

$$u_f = r_f \cdot i_f + \frac{1}{\omega_n}\frac{d\psi_f}{dt} \tag{2.12}$$

$$u_q = r_s \cdot i_q + \frac{1}{\omega_n}\frac{d\psi_q}{dt} + n \cdot \psi_d \tag{2.13}$$

$$0 = r_D \cdot i_D + \frac{1}{\omega_n}\frac{d\psi_D}{dt} \tag{2.14}$$

$$u_0 = r_s \cdot i_0 + \frac{1}{\omega_n}\frac{d\psi_0}{dt} \tag{2.15}$$

$$0 = r_Q \cdot i_Q + \frac{1}{\omega_n}\frac{d\psi_Q}{dt} \tag{2.16}$$

With the dq-reference frame established, all inductances are independent of rotor position resulting in the following simplified expressions for the flux linkages.

$$\psi_d = x_d \cdot i_d + x_{ad} \cdot i_f + x_{ad} \cdot i_D \tag{2.17}$$

$$\psi_f = x_{ad} \cdot i_d + x_f \cdot i_f + x_{ad} \cdot i_D \tag{2.18}$$

$$\psi_q = x_q \cdot i_q + x_{ad} \cdot i_Q \tag{2.19}$$

$$\psi_D = x_{ad} \cdot i_d + x_{ad} \cdot i_f + x_D \cdot i_D \tag{2.20}$$

$$\psi_0 = x_{a\sigma} \cdot i_0 \tag{2.21}$$

$$\psi_Q = x_{aq} \cdot i_q + x_Q \cdot i_Q \tag{2.22}$$

The reactances in equations 2.17 to 2.26 are given by:

$$x_d = x_{ad} + x_{a\sigma} \quad (2.23) \qquad x_D = x_{ad} + x_{D\sigma} \quad (2.24)$$

$$x_q = x_{aq} + x_{a\sigma} \quad (2.25) \qquad x_Q = x_{aq} + x_{Q\sigma} \quad (2.26)$$

$$x_f = x_{ad} + x_{f\sigma} \quad (2.27)$$

2.3 Torque control

The two main methods for controlling the torque in a synchronous machine are given as follows:

- Controlling phase angle of current to zero: $cos(\varphi) = 1$
- Controlling phase angle of current to be equal to pole wheel angle: $\varphi_p = 0°$

As the source of ohmic losses in the stator of the machine is given by $i_s^2 \cdot r_s$, an aim for the torque control is to minimise the stator currents to keep the losses sufficiently small, while producing the desired torque. Not only does this increase the overall system efficiency, but the lower stator currents enables for the usage of a lower power rated stator converter, reducing system costs.

The maximum torque per ampere control method is generally realised by controlling the phase angle of the stator current to zero, which entails unity power factor and stator currents and voltages in phase. A potential drawback related to this method of control is the inability to govern the power factor, however, for the given application the added benefits of achieving maximum torque per ampere outweigh the need for control of power factor.

The generated electromagnet torque is expressed in Equation 2.28, where the subscripts denote stator values in the dq-reference frame.

$$\tau_e = \frac{p}{2}(\psi_{sq} i_{sd} - \psi_{sd} i_{sq}) \quad (2.28)$$

With the introduction of the α-β coordinate system, Equation 2.28 is further modified to:

$$\tau_e = \frac{p}{2}\left(\psi_{s\alpha}^k i_{s\beta}^k - \psi_{s\beta}^k i_{s\alpha}^k\right) \quad (2.29)$$

The α-β coordinate system is conceptually similar to the dq-reference frame, although this system is static and does as such not rotate with the rotor. The superscript k stipulate the orientation of the coordinate system along with an arbitrary axis.

With the stated aim for the torque control to allow for maximum torque per ampere, investigation of Equation 2.3, 2.5 and 2.7 reveal that with the stator resistance omitted,

the stator voltage leads the flux by 90°. Consequently, the stator current vector must be set such that it too leads the stator flux by 90°, with the purpose of controlling the power factor to unity and stator current and voltage in phase.
An issue arises when the machine is operating under opposite torque and speed. As discussed by Bolstad, it is impossible to achieve stator voltage and current in phase in the circumstances with opposing torque and speed vectors [18]. Therefore, the current vector is relocated by 180°such that it is directly opposing the voltage vector. As a result, unity power factor with negative sign is achieved.

Thus, orienting the α-axis along the stator flux linkage vector, the expression for the torque in Equation 2.29 simplifies to:

$$\tau_e = \frac{p}{2}\psi_{s\alpha}^{\psi_s} i_{s\beta}^{\psi_s} = \frac{p}{2}\psi_s i_s \tag{2.30}$$

As can be seen from Equation 2.30, the torque control to allow for maximum torque per ampere is realised by keeping the stator current fully in the β direction. Therefore, the current reference for the control system is calculated by Equation 2.31.

$$i_{s,ref} = \frac{\tau_{ref}}{\psi_s} \tag{2.31}$$

The Simulink model used in this Master thesis is based on previous work done by [2] and [18]. The control structure, as realised for the Simulink simulation, is depicted in Figure 2.2.

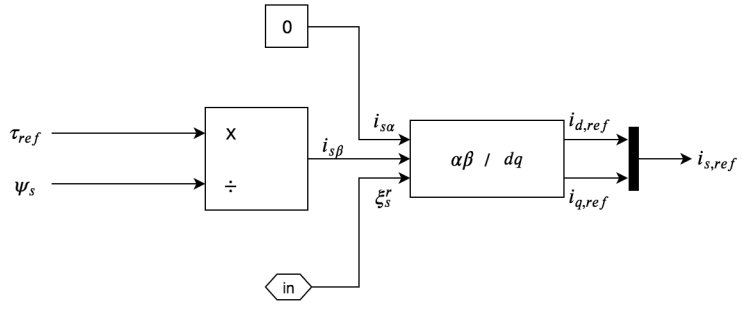

Figure 2.2: Scheme for calculating current reference for maximum torque per ampere. Reproduced from [3]

The parameter ξ_s^r is defined as the angle between the stator current vector and the stator flux linkage vector, and is elaborated upon in section 4.1.
Unless stated otherwise, the main control regiment for the majority of simulations will be under the stated aim of torque control.

Chapter 3

Simulation Model

In this chapter, the most significant parts of the Simulink model used in the master thesis will be elaborated upon. With the Simulink model utilized for the master thesis exactly the same as for the previously completed project thesis, no further explanation of the model will be given. As such, the following section is a verbatim reproduction from the same chapter from the project thesis [3].

Figure 3.1 depicts an overview of the main machine components.

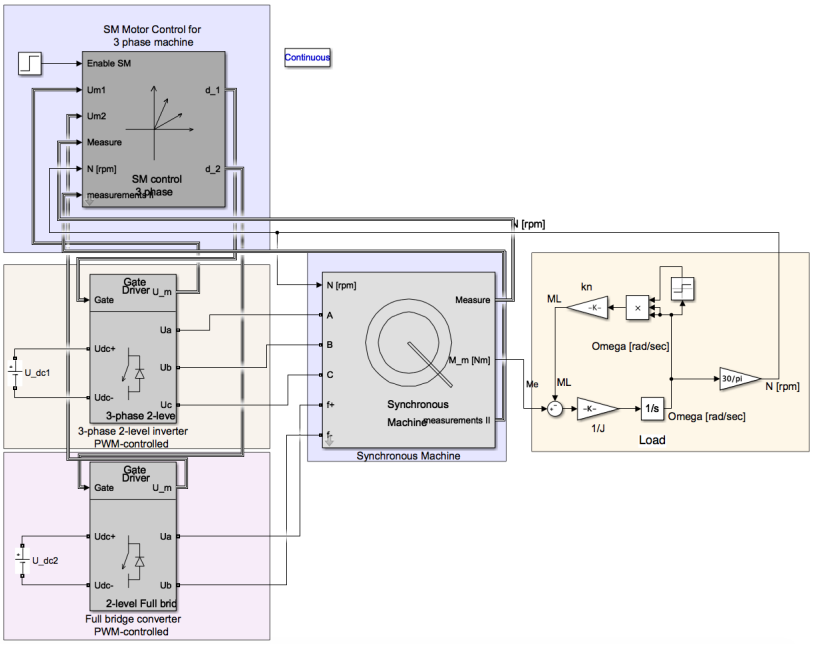

Figure 3.1: Simulink model. Reproduced from [3]

The rightmost block diagram represents the load modelling of the machine. As previously stated, the function of the given machine is to function both as a hydropower generator, as well as a pump to refill the reservoirs when needed. As such, the load is modelled with the general centrifugal pump characteristic shown in Equation 3.1.

$$M_{load} = k \cdot \omega_{mech}^2 \tag{3.1}$$

With regards to the machine, both the field and stator windings are supplied by a DC voltage passing through converters. For the stator voltage a three-phase, two-level inverter is used, while the field voltage is controlled by a full-bridge DC-DC converter. Both converters are controlled through pulse width modulation (PWM), which is handled by the motor control block. The output from this block is the required duty cycles for the inverter and DC-DC converter, required to achieve the desired voltages in the stator and field windings. The switching frequency of the system is set at 3000 Hz.

For the simulations, the ode23tb solver is used, with the simulation type set to continuous. The solver reset method is set to robust, with a maximum step size of 100^{-6} s.

3.1 Pulse width modulation

As previously mentioned, the converters are controlled through PWM. The DC-DC converter feeding the field voltage to the machine utilises unipolar voltage switching and consists of two bridge legs with each leg being fed a separate control signal. The modulation functions in such a way that a triangular signal is compared to a control voltage. In periods where the triangular signal is higher than the control signal, one leg is on while the other is turned off, and vice versa. The output to the field winding is subsequently given by the difference in the voltage between the bridge legs. Equation Equation 3.2 depicts the relations ship between the input DC voltage, V_d, and the output voltage V_0.

$$V_0 = \frac{V_d}{\hat{V}_{tri}} v_{control} \tag{3.2}$$

Where the period of the triangular signal V_{tru}, T_{tri} is given by $1/f_{tri}$, with the triangular switching frequency set at 3000 Hz. As previously mentioned, the stator voltage of the machine is being fed by the two-level three-phase inverter, consisting of three bridge legs where an individual control signal controls each separate legs. The modulation method used in this inverter is called sinusoidal modulation. The output line-to-line voltage of the inverter is given by Equation 3.3.

$$U_{ab} = \frac{\sqrt{6}}{4} \cdot U_{dc} \cdot M \approx 0.6124 \cdot U_{dc} \cdot M \tag{3.3}$$

For both the DC-DC converter and the two-level, three-phase inverter synchronised sampling is utilised to measure the required currents. As there is no current ripple, in the beginning, middle and end of the triangular wave period used for control, the use of filters

can be avoided by measuring the current at these time instances [2]. As such the sampling time is given by Equation 3.4.

$$T_{sampling} = \frac{T_{tri}}{2} \tag{3.4}$$

An advantage of using the synchronised sampling is that no delay is added to the signal.

3.2 Moving average filters

As there are significant ripple currents in the system, moving average filters have been added to the machine, in order to reduce the ripple's influence on the controllers. As presented in [2], the average current signal over a period of half the switching period is given by Equation 3.5.

$$I_{avg}[kT_{sampling}] = \frac{1}{T_{sampling}} \int_{[k-1]T_{sampling}}^{kT_{sampling}} I(t)dt \tag{3.5}$$

Where $T_{sampling}$ is given by T_{tri}/2. By taking the average of the current signal the current ripple is negated due to its symmetry, given that the integral is done over a period T_{tri}

3.3 Controllers

The controllers of the model where implemented and tuned in a previous project thesis, and will as such not be described in the present thesis. See [1] for more information. However, as they will influence the performance the gains and time constants of each controller is listed in Table 3.1.

Parameter	Symbol	Value
Field current controller gain	K_{p_f}	1.98
Field current controller time constant	T_{i_f}	0.03
Stator d-axis current controller gain	K_{p_d}	0.54
Stator d-axis current controller time constant	T_{i_d}	0.01
Stator q-axis current controller gain	K_{p_q}	0.72
Stator q-axis current controller time constant	T_{i_q}	0.01
Flux controller gain	$K\psi$	4
Flux controller time constant	T_{i_ψ}	0.18
Speed controller gain	K_ω	247.26
Speed controller time constant	T_{i_ω}	0.004

Table 3.1: Controller parameters, retrieved from [1]

As specified by Bolstad, all controller parameters are functions of actual machine values, meaning any changes to the machine will results in automatically tuned controllers [1, p.20].

Chapter 4

Identification

In this chapter an adapted version of the identification methods explored in the project thesis is given, with the inclusion of the current model for the present thesis. See [3] for more information.

Given that the self-sensing method is solely reliant on the additional field excitation signals and its response on the stator currents, the method will be employed for standstill and lowspeed operation. The self-sensing model is an adaptation of the work presented in [5]. The model will be utilized in unison with the current model for low-speed operation, when sufficient back-EMF information is available.

For higher-speed operation the voltage model, as presented in [18, 19], will be utilised.

4.1 Voltage model

The voltage model is based on calculating the stator flux linkage vector, which due to being independent of the position is a well-suited state observer for the rotor position and speed. The calculation of the stator flux linkage from the stator current and voltage is given by Equation 4.1.

$$\underline{\psi_s^s} = \int_0^t (\underline{u_s^s} - r_s \underline{i_s^s}) dt \tag{4.1}$$

The Simulink model used throughout the present thesis is based on the work done by Bolstad, and as such no detailed explanation of the method used to estimate the position and speed from the stator flux linkage will be given, but rather a cursory overview of relevant equations and methodologies. For more information see [1, 18].

The connection between the stator current and flux linkage to the dq-coordinate system and the a-phase, as presented in [18], is presented in the phasor diagram shown in Figure 4.1.

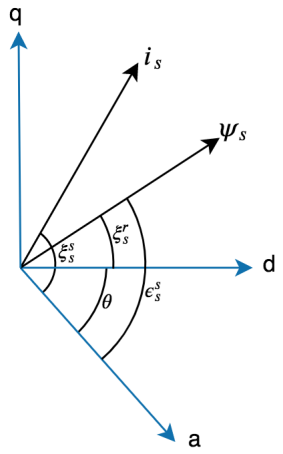

Figure 4.1: Phasor diagram showing the relation between ψ_s, i_s, dq-coordinate system and the a-phase. Reproduced from [3]

Extraction of the relations depicted in Figure 4.1 was extracted in [1] and is shown in Equation 4.2.

$$sin(\xi_s^s - \theta) = \frac{\left(\sigma_{qQ} x_q + \frac{x_{Mq}}{1+T_{Qs}}\right)}{\psi_s} i_s sin(\epsilon_s^s - \theta) \tag{4.2}$$

As can seen in Equation 4.2, the rotor position is estimated by employing the preceding position as feedback into the rightmost sine function. As a delay is present in the input position, the product of sampling time and estimated rotor speed is added to the position, given that this is approximately the rotational distance of the rotor covered during the preceding sample.

With the rotor position estimated, the rotor speed is obtained by Equation 4.3.

$$\omega[k] \approx \frac{\theta[k] - \theta[k-1]}{T_{samp}} \tag{4.3}$$

4.2 Current model

The current model is an oft used method used for calculating the stator flux linkage, from which the position and speed of the rotor can be extracted. The model uses the measured stator and field current, in the dq-axis system by Equation 2.17 and 2.19 to calculate the stator flux linkage, as shown in Equation 4.4.

$$\underline{\psi_s^s} = \psi_d^s + j\psi_q^s \tag{4.4}$$

As discussed by Nestli, the current model's efficacy concerning position estimation is dependent on the speed of the machine, wherein the highest resolution estimates occur for

low speed and decreases as the speed increases [20]. Consequently, the current model is used for low-speed operation.

Same as for the voltage model, the Simulink model used in the master thesis is based on previous work by Bolstad with the current model already implemented, as such no detailed extraction of the current model equations will be given. For more information see [18].
The extraction of the rotor speed and position from the stator flux linkage is the same as for the voltage model, as explained above.

4.3 Self sensing

The self-sensing model will, as discussed above, be utilized for standstill and operating in unison with the current model for low-speed operation. The model is based on the work of Uzel et al., with some noteworthy differences. In [5], the additional excitation signal is a 300 Hz AC component of the field winding, arising from the feeding of the field circuit from a three-phase bridge rectifier. In contrast, the present model feds the field winding using pulse width modulation, which in turn means that a wide range of frequencies may be employed.

Although the same exploration of the self-sensing model discussed below have been discussed in the project thesis [3], the relative novelty of the approach means that an adapted version is warranted a reproduction in the present Master thesis.

The extraction of the relevant motor equations used to explain the fundamentals of the self-sensing methodology is directly extracted from [5].

Employing Equation 2.11 and 2.8, referring the stator voltage equations to the dq-reference frame is given by Equation 4.5 and 4.6.

$$u_{sd} = r_s i_{sd} - \omega\psi_{sq} + \frac{d\psi_{sd}}{dt} \qquad (4.5) \qquad u_{sq} = r_s i_{sq} + \omega\psi_{sd} + \frac{d\psi_{sq}}{dt} \qquad (4.6)$$

Where the stator flux linkage vectors are given by Equation 4.7 and 4.8, neglecting the damper windings reactances.

$$\psi_{sd} = x_{sd} i_{sd} + x_{ad} i_f \qquad (4.7) \qquad \psi_{sq} = x_{sq} i_{sq} \qquad (4.8)$$

Initial investigation of the viability of utilizing the additional excitation signal from the field current did not include the damper windings, as there were some concern of the windings functioning as filters, diminishing the rotor-stator magnetic coupling used to extract

the rotor position. However, as no significant issues for the propagation of the excitation signal was detected with the damper windings connected, their respective reactances will be omitted from the explanation of the self-sensing model.

By only modelling the high-frequency constituents of the machine equations, the stator voltage vector expression simplifies to Equation 4.9 and 4.10.

$$u_{sdi} = \frac{d\psi_{sdi}}{dt} \tag{4.9}$$

$$u_{sqi} = \frac{d\psi_{sqi}}{dt} \tag{4.10}$$

Where the subscript *i* denotes the high-frequency component of a given signal. Due to the stator voltage vectors being zero for the field excitation frequency, Equation 4.7 and 4.8 simplifies to the following.

$$x_{sd}\frac{di_{sdi}}{dt} + x_{ad}\frac{di_{fi}}{dt} = 0 \tag{4.11}$$

$$x_{sq}\frac{di_{sqi}}{dt} = 0 \tag{4.12}$$

Using Equation 4.11 and 4.12 the relationship between i_{sdi} and i_{fi} are given by Equation 4.13.

$$\frac{di_{sdi}}{dt} = -\frac{x_{ad}}{x_{sd}}\frac{di_{fi}}{dt} \tag{4.13}$$

Moreover, assuming equivalent initial condition integration of Equation 4.13 the high-frequency component of the stator current is given as:

$$i_{sdi} = -\frac{x_{ad}}{x_{sd}}i_{fi} = -k_{rs}\frac{x_{ad}}{x_{sd}}i_{ri} \tag{4.14}$$

With k_{rs} denoting the rotor to stator ratio, and i_{ri} the high-frequency component of the rotor field excitation current. Finally, the stator current vector's high frequency constituent is given by Equation 4.15.

$$\begin{bmatrix} i_{s\alpha i} \\ i_{s\beta i} \end{bmatrix} = \begin{bmatrix} cos(\theta) & -sin(\theta) \\ sin(\theta) & cos(\theta) \end{bmatrix} \begin{bmatrix} i_{sdi} \\ 0 \end{bmatrix} = \kappa \cdot i_{ri} \begin{bmatrix} cos(\theta) \\ sin(\theta) \end{bmatrix}, \qquad \kappa = -\frac{x_{ad}}{x_{sd}}k_{rs} \tag{4.15}$$

From Equation 4.15 it is clear that the high-frequency components of the stator currents contain information on the position.
The connection between the field excitation current's high-frequency component and the stator currents are depicted in Figure 4.2, which depicts the modulation of the stator currents in the α-β reference frame, influenced by the high-frequency rotor current.

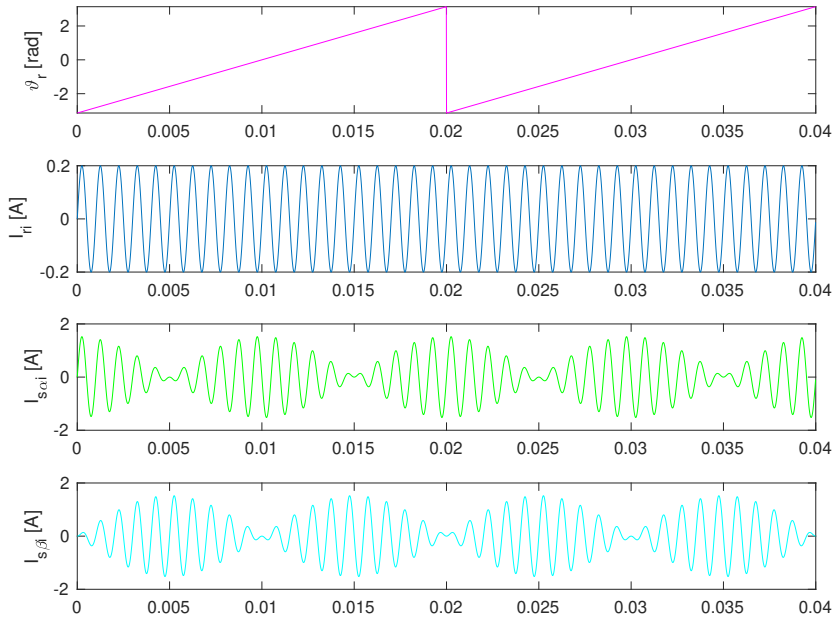

Figure 4.2: Rotor position, high-frequency rotor current and stator responses in the α-β frame. Reproduced from [3]

From the resulting high-frequency stator currents there are several estimation methods available to discern the rotor position and subsequently rotor speed.

4.3.1 Self-sensing results

In this section a presentation of the self-sensing and a summation of the most important results from the project thesis will be given [3].

In the project thesis, initial testing of the self-sensing sensorless estimation scheme was performed in Simulink, with the stator converter disconnected. Furthermore, the influence of the damper winding on the propagation of the high-frequency component of the field current was investigated.

There was some initial concern that the damper windings would act as a filter, diminishing the stator responses as the effect of the field current would be reduced. To verify the viability of including the damper winding an equivalent circuit of the synchronous machine was simulated in Simulink. The simulations showed no noticeable reduction in the stator responses were present, and as such the self-sensing estimation scheme was deemed viable for further testing.

As specified in section 4.3, the high-frequency stator current components contains the necessary information required for the estimation of the rotor position. Following [5], bandpass filters were implemented as a means to extract the high-frequency constituents of the field and stator currents. With the stator converter disconnected, a 300 Hz sinusoidal ripple was added to the field current to emulate the naturally occurring field excitation signals. Consequently, the bandpass filters were designed for a centre frequency of 300 Hz, which serve to allow for easy propagation of the excitation signal, meanwhile filtering out any undesired harmonics. Initially, an infinite impulse response (IIR), sixth-order Butterworth filter was designed in Matlab and subsequently implemented in Simulink, as per the specification laid out in [5]. However, as the filter did not yield a satisfactory performance, the embedded second-order filter block in Simulink was utilised.

With the high-frequency components established, initial estimation efforts were executed, with the rotor position initialised to a position of 22.5 °and zero torque to simulate standstill operation. As described in the literature, the simplest way to estimate the rotor position is to utilise the four-quadrant inverse tangent function, denoted as atan2 in Matlab [5, 21]. The position of the rotor is given by the relation between the high-frequency components of stator currents in the α- and β-direction, as shown in Equation 4.16.

$$\theta = tan^{-1}\left(\frac{i_{s\beta i}}{i_{s\alpha i}}\right) \tag{4.16}$$

The usage of the self-sensing sensorless control utilising the atan2-function for position estimation was successfully validated for standstill operation with and without the inclusion of damper winding, as shown in Figure 4.3.

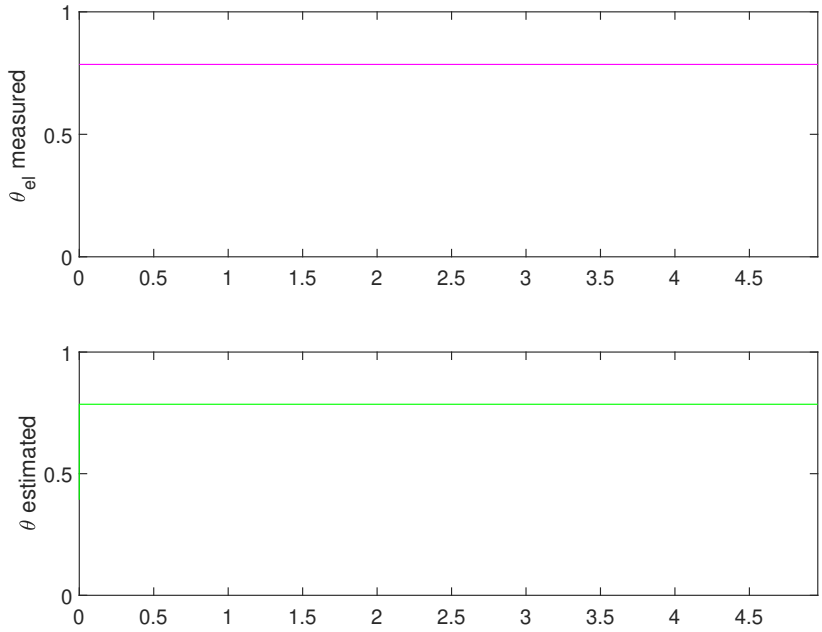

Figure 4.3: Measured and estimated electrical angle, with damper windings [rad]. Reproduced from [3]

However, it is essential to specify that the resulting position from the atan2-function contains significant noise which could lead to controller issues without additional filtering. The noisy output when using the four-quadrant inverse tangent function is anticipated, as the literature states that although the method is simple and easy to implement, its applicability for sensorless control is limited due to high sensitivity to measurement noise [5].

With the self-sensing sensorless estimation verified for standstill operation, a low torque was applied to the model, as a means to simulate low-speed operation. Instead of a fixed position, the rotor now rotates, leading to a time-varying angular position.

As shown in Figure 4.4, the angle is successfully estimated for one period, notwithstanding the significant signal ripple. However, the estimation breaks down in the subsequent period.

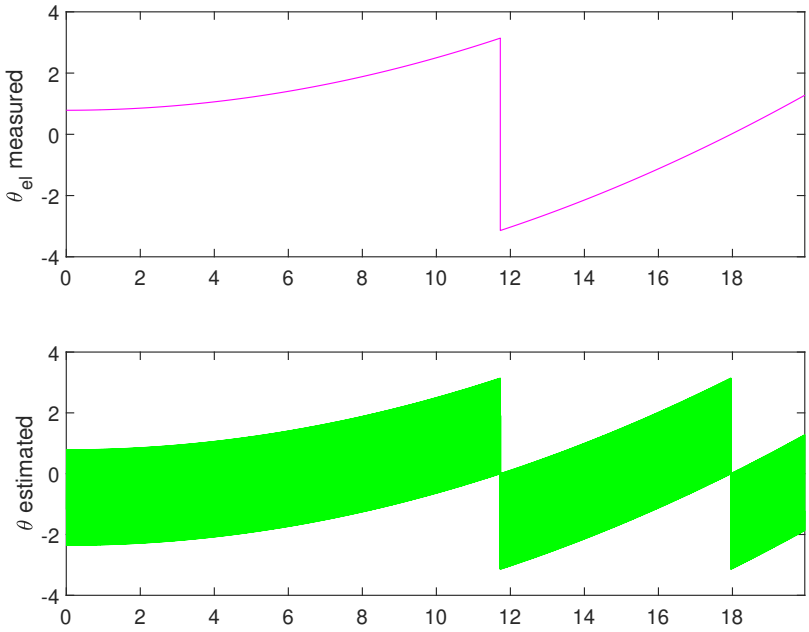

Figure 4.4: Electric measured and estimated electric angles, with the inclusion of damper windings [rad]. Reproduced from [3]

The erroneous estimation of rotor position was in the project thesis assumed to be the result of the high-frequency stator current components, $i_{s\alpha i}$ and $i_{s\beta i}$having a too fast fundamental frequency [3, p.33]. However, further investigation and comparison with [5] show that the error does not lie with the fundamental frequency.

As discussed above, the atan2-function is highly sensitive to measurement noise, and even-though several filters have been utilised to clean up the high-frequency components, significant noise remains in the signal, which could serve to explain the issue.

Nevertheless, although some alterations can be made to the noisy output from the atan2-function, such as additional filtering, this would only serve to increase the complexity of the system; meanwhile, other estimation techniques are available.

4.3.2 Phase-locked loop

As a consequence of the issues mentioned above concerning the usage of the four-quadrant inverse tangent function, it was decided to implement a phase-locked loop (PLL) for position and speed estimation. Due to time limitations in the project thesis, only a brief introducing and explanation of the PLL was given, and therefore a more thorough exploration will be presented in this section, in addition to the results from the project thesis.

Any PLL is a circuit comprised of three basic elements, namely a loop filter, phase-detector (PD) and voltage-controlled oscillator (VCO) [4]. The primary function of a PLL is to vary a VCO frequency, and as a consequence, the phase, corresponding to an input until a match of the input signal occurs [22].

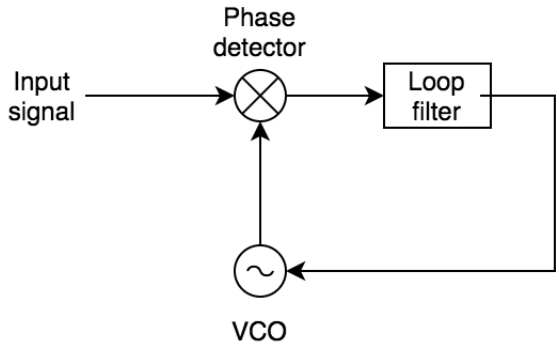

Figure 4.5: Basic PLL. Adapted from [4]

Figure 4.5 depicts the most basic form of PLL. As explained by Gardner, supposing that an input signal contains information in its frequency or phase, the signal is assured to be corrupted by additive noise. The function of the PLL is then to get rid of as much noise as possible while reproducing the input signal [4, p.2].

Phase-locked loops have been widely utilised in synchronization and control of grid-connected converters and have garnered increasing interest in sensorless control of motor drives, specifically in conjunction with high-frequency signal injection. The PLL estimation scheme offers simplicity and relative ease of implementation [5, 23, 24].

Concerning the sensorless control, the most basic form of the phase-locked loop was at first tried implemented. The synchronous reference frame phase-locked loop (SRF-PLL) involves the transformation from the static $\alpha\beta$-coordinate system to the previously mentioned dq-reference frame, rotating at synchronous speed.

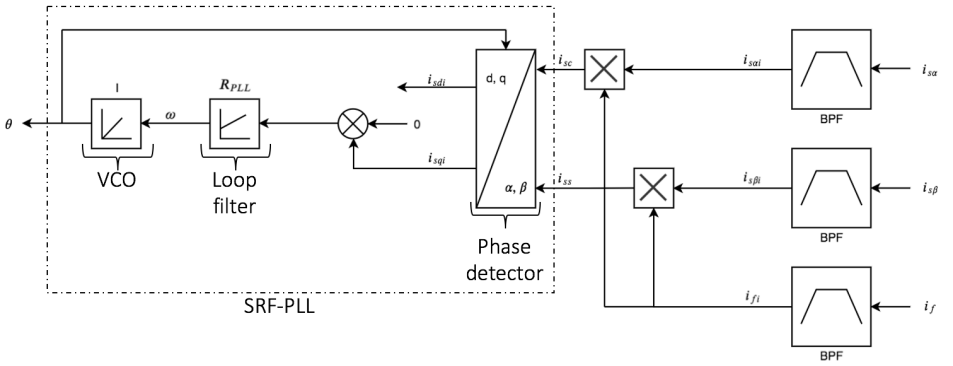

Figure 4.6: Established rotor position evaluation by a PLL. Source: adapted from [5]

.

Figure 4.6 shows the SRF-PLL as implemented in [5]. As described in subsection 4.3.1, the bandpass filters depicted in Figure 4.6 are dimensioned for a centre frequency of 300 Hz. However, to achieve the required half-wave envelopes for the dq-transformation, the phase of i_f needed to be altered. Adjusting the centre frequency of the field current bandpass filter showed that a frequency of 600 Hz resulted in the desired phase-shift, wherein i_f is 180°phase-shifted compared to $i_{s\alpha}$ and $i_{s\beta}$. Bode plots of the implemented Simulink bandpass filter are shown in Appendix C.

Concerning position estimation, initial testing with the SRF-PLL did not yield satisfactory results. The performance of the second-order system utilised in Figure 4.6 is limited by the bandwidth of the system, as the selection of bandwidth is a compromise between fast dynamic response or good filtering performance. According to Barbosa Rolim et al., a well-designed PLL meets the criteria of narrow bandwidth for increased noise rejection, and a relative damping of $\zeta = 0.707$ [25].

Utilising the criteria above, the gain and time constant of the PI-controller were calculated using Equation 4.17 and 4.18 per the specifications in [24], based on the required damping ratio, and choosing a natural frequency facilitating a low bandwidth and ability to filter out the 300 Hz component from the excitation signal.

$$K_i = \omega_n^2 \tag{4.17}$$

$$K_p = 2 \cdot \zeta \sqrt{K_i} \tag{4.18}$$

Although a low bandwidth did yield satisfactory filtering performance in the estimated rotor position, the trade-off in dynamic response resulted in a too low rise-time compared to measured position, as seen in Figure 4.7. Furthermore, an increase in the bandwidth to allow for a faster dynamic response did little to mitigate the slow rise-time; in addition, the estimated position slope became markedly different than the measured position, as depicted in Figure 4.8. Further increase in bandwidth only resulted in higher signal noise, as well as significant initial transients.

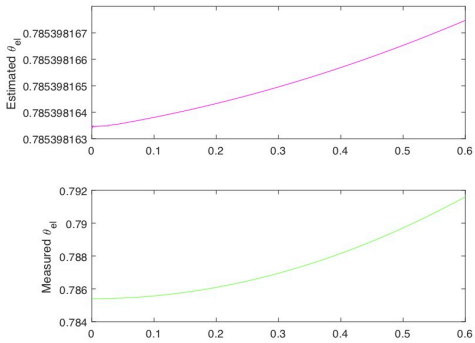

Figure 4.7: Estimated/measured electric angles. Bandwidth=0.21 Hz, ζ=0.707

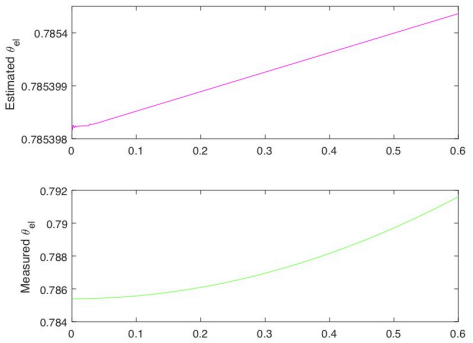

Figure 4.8: Estimated/measured electric angles. Bandwidth=105.74 Hz, ζ=0.707

The issues with the PLL discussed above may be explained by a failure to lock on to the input signal during the start-up transient. A narrow bandwidth PLL may fail to get a lock on an input signal if the following criteria are met concurrently:

- Higher-order or subharmonics in the input signal
- One of the above harmonics have a frequency close in range to the initial PI-controller output.
- A larger difference in target fundamental frequency and PI-controller output than lock range.

As discussed in [22, p.22], adjusting the loop bandwidth may in some cases be insufficient to rid the loop system of unwanted signal pollution. Given that some harmonics still were present in the estimated rotor position, coupled with the problems with the dynamic response, a first order lowpass filter was inserted after the phase-detector.

With the lowpass-filter added to the system, Equation 4.17 and 4.18 is no longer viable for calculating the gain and time constant as the system is a sixth-order loop. The open-loop transfer function of the PLL, with the inclusion of the lowpass filter, is given by Equation 4.19.

$$H_{ol}(s) = K_p \frac{1 + T_i \cdot s}{T_i \cdot s} \frac{1}{1 + T_f \cdot s} \frac{1}{s} \tag{4.19}$$

As described by Abdelrahem et al., symmetrical optimum can be used to calculated the gains of the PI-controller as shown in Equation 4.20 and 4.21 [23, p.3099].

$$T_i = \beta T_f \tag{4.20}$$

$$K_p = \frac{1}{\sqrt{\beta} T_f} \tag{4.21}$$

Given that the lowpass-filter should be able to filter out the 300 Hz component from the excitation signal, a cut-off frequency of 10 Hz was utilised. Consequently, the only parameter available for tuning is β.

In the project thesis, due to time limitations, a torque reference of 0.1 pu was applied to the machine, to speed up the rotation and consequently to achieve a broader swath of data points for comparison between estimated and measured rotor position. After running numerous simulations, it was shown that a β-value of 0.00125 gave a reasonably accurate estimated rotor position, resulting in the PI-controller parameters shown in Table 4.1.

β	0.00125
Ti	2 μs
Kp	1777.2

Table 4.1: PLL PI controller values from symmetric optimum

The estimated and measured rotor position is depicted in Figure 4.9.

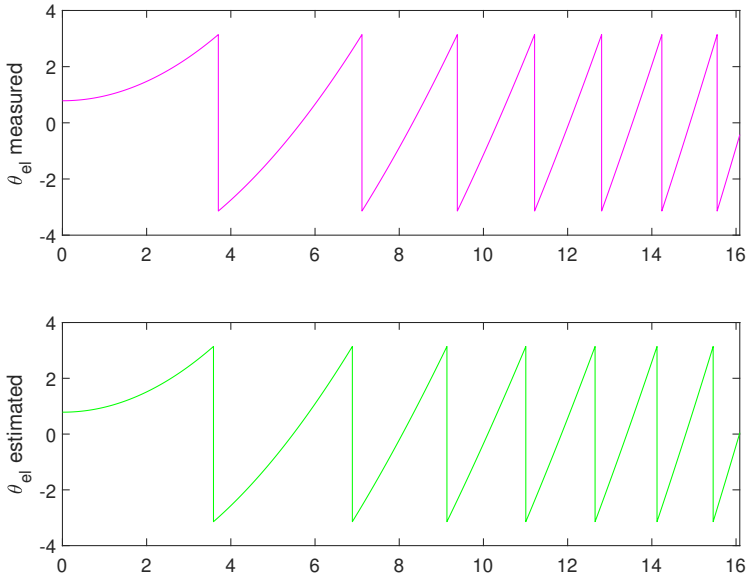

Figure 4.9: Measured and PLL estimated electrical angle. Reproduced from [3]

The position is accurately tracked over the entire time-span; however, the estimated position has a slightly faster periodicity, which can be remedied by more rigorous tuning.

It is essential to specify that by choosing β=0.00125, the resulting PLL closed-loop transfer function is unstable for all frequencies, as is apparent from the phase margin shown in Table 4.2.

Gain margin	∞
Phase margin	-170°
Relative damping $\left[\zeta = \frac{\beta^2-1}{2}\right]$	≈-0.5
Bandwidth	289.37 Hz

Table 4.2: Closed loop PLL transfer function results for SRF-PLL

In addition to the negative phase margin, the tuning results in negative relative damping meaning the placement of a pole in the right half of the S-plane, see Figure D.1 of the root locus plot.

Although the closed-loop instability does not influence the rotor position estimation for the given torque reference of 0.1 pu, further testing revealed that the tuning is only valid for slight variations in torque references and therefore speeds, as shown in Appendix E. Simulations showed that variations of $\pm$ 10% in applied torque gave accurate tracking of rotor position; however, further variations in applied torque lead to significant deviations between estimated and measured position.

The inability of the PLL to operate in a broad range of drive operating conditions is somewhat expected, as Uzel et al. discuss how a fixed tuning of the PI-controller resulting in successful rotor position estimation across a range of speed demands is impossible [5].

4.3.3 Atan2-based phase-locked loop

The iteration of the PLL described above was deemed sufficient during the project thesis analysis, however, for the master thesis the stability issues discussed above and the inability of the PLL to track the rotor position accurately across a broader speed range, meant that a third alternative approach for position estimation was evaluated.

The proposed estimation scheme is depicted in Figure 4.10. The estimation method is based on the same principles described in section 4.3, wherein the position of the rotor can be extracted from the high-frequency components of the stator currents. Furthermore, the same SRF-PLL structure described above is utilised to improve the atan2-based estimate rotor position.

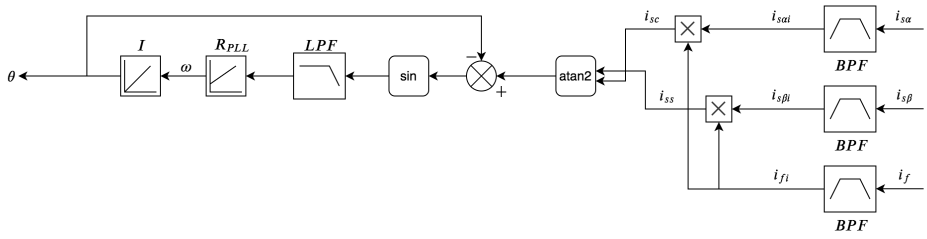

Figure 4.10: Block diagram for atan2 function in conjunction with SRF-PLL for position estimation

The input to the PLL is the error between the estimated rotor position and the preceding atan2 based position. The method is an adaption of the work of Iepure et al., wherein a similar approach is used on a permanent magnet brushless dc motor [26].

The open loop transfer function of the PLL is the same as shown in Equation 4.19, meaning that symmetric optimum is still valid for tuning of the PI-controller. Initial testing showed that by using the atan2 function in conjunction with the PLL observer, the β-value is no longer needed to be tuned to values resulting in a closed loop instability in order to achieve accurate tracking. The lowpass filter cutoff frequency was once more set to 10 Hz to filter out the 300 Hz excitation signal, while β was set to 8 for narrow bandwidth and stability purposes. The resulting PI-controller parameters are shown in Table 4.3.

β	8
Ti	0.1273 s
Kp	22.2144

Table 4.3: PLL PI controller values for atan2 based SRF-PLL

The estimated and measured electric angle is are depicted in Figure 4.11.

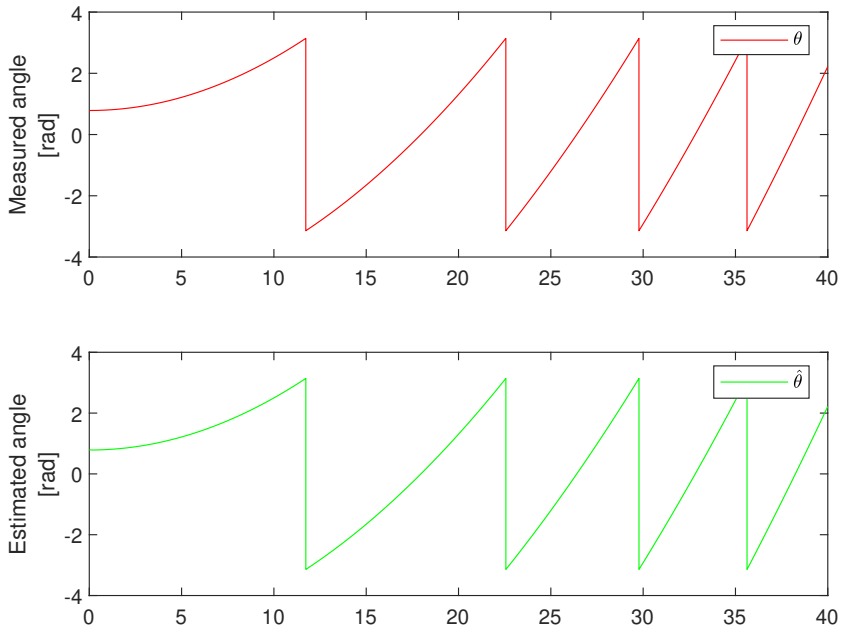

Figure 4.11: Estimated electric angle using atan2 function in conjunction with SRF-PLL and measured electric angle, with an applied torque reference of 0.01 pu.

The position of the rotor is accurately tracked for the entire duration of the simulations.

Compared to the estimation process utilising only the SRF-PLL, the atan2-based PLL allows for a more accurate position estimate and negates the need for an unstable and sensitive tuning of the PI-controller.

As expected, the PLL takes some time to lock on to the incoming signal, as shown in Figure 4.12.

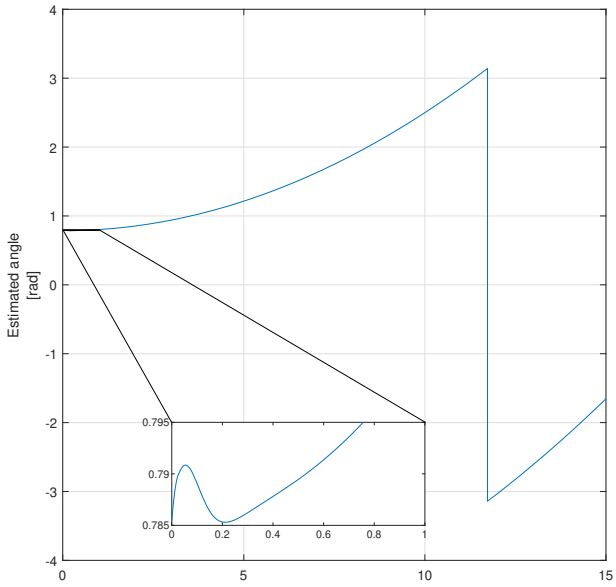

Figure 4.12: Estimated electrical angle, with lock-on response

As can be seen from Figure 4.12, it takes approximately 0.5 seconds for the PLL to lock on to the incoming signal, and accurately track the rotor position. Further tuning could prove to reduce the lock-on time, however, the relatively short time interval may be inconsequential for control purposes, and will only be revised if undue influence on the machine control is detected.

Furthermore, as the atan2-based PLL is significantly less constrained concerning fine-tuning of the controller, which in turn allows for choosing a β-value fulfilling the PLL criteria of narrow bandwidth, the closed-loop instability issues are countermanded, as shown in Table 4.4.

Gain margin	∞
Phase margin	101°
Relative damping $\left[\zeta = \frac{\beta^2-1}{2}\right]$	31.5
Bandwidth	5.8596 Hz

Table 4.4: Closed loop PLL transfer function results for atan2 based SRF-PLL

The benefit of a wider dynamic range of the PLL, meaning high performance position estimation for multiple drive conditions, is highlighted in Figure 4.13.

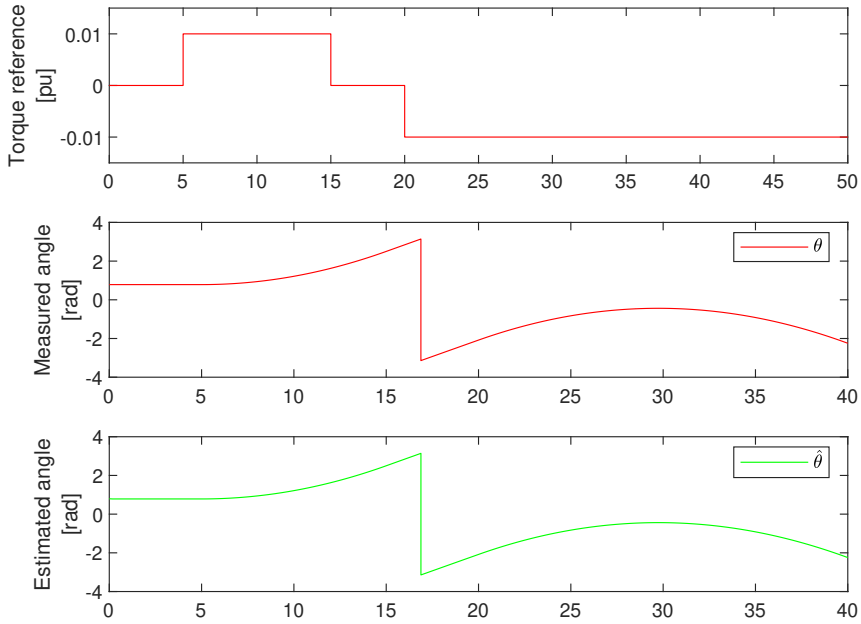

Figure 4.13: Estimated electric angle using atan2 function in conjunction with SRF-PLL and measured electric angle, with variable torque reference.

As seen in Figure 4.13, the estimation method can accurately track the rotor position from standstill to positive torque, and through zero crossings.

As such, utilising the additional excitation signal in the rotor field winding in conjunction with the estimation process described above should prove highly useful for standstill and low-speed operation.

Chapter 5

Stator converter reconnected

Having established the viability of utilising the combination of the four-quadrant inverse tangent in conjunction with a PLL for position estimation, the three-phase, two-level stator inverter was reconnected. Consequently, the switching of the inverter will have an impact on the stator responses used for estimation purposes. Furthermore, as the stator current controller has not been tuned for the addition of the 300 Hz component, a potential issue arises in relation to the propagation of the high-frequency field excitation and current controller being too fast, meaning the additional excitation signal not causing the desired stator responses.

To investigate that no undue influence from the stator inverter on the additional field excitation signal propagation is occurring, the 300 Hz component was once more applied to the system. The benchmark for verification of signal propagation was to achieve the same high-frequency stator currents as described in Figure 4.2. Once more a low torque reference of 0.01 pu was applied to the Simulink model.

As can be seen from Figure 5.1, which depicts the nominal, high-frequency and demodulated stator currents in the alpha-direction, the high-frequency component of $i_{s\alpha}$ has the form of a modulated signal with an upper and lower envelope and a 300 Hz ripple. Consequently, the impact of the stator inverter and concurrently the stator current controller seems negligible with regard to achieving the required stator responses for estimation purposes.

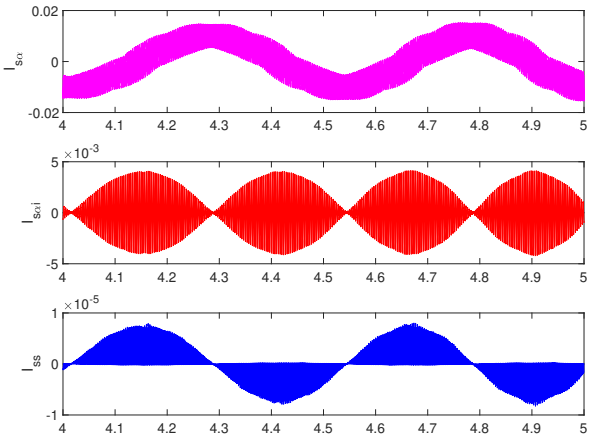

Figure 5.1: Stator currents in alpha-direction. From top to bottom: nominal, high-frequency and demodulated.

The negligible impact of stator current controller on the field excitation signal's magnetic coupling with the stator converter is reflected in the Figure 5.2, wherein the electrical angle is correctly estimated, notwithstanding an error at each full rotation and some initial transient error seen as a ripple at the beginning of the plot.

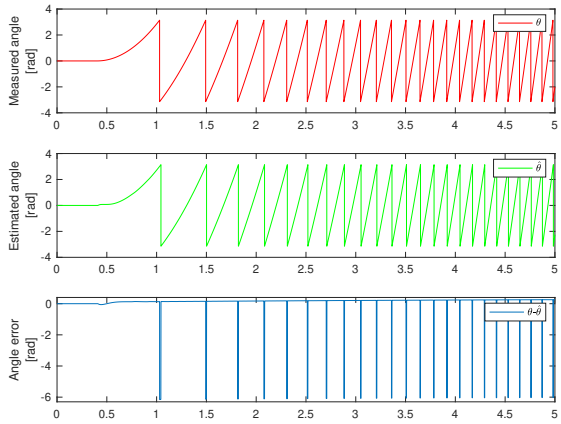

Figure 5.2: Measured and estimated electric angle, with estimated angle error

It is important to note that the atan2 SRF-PLL combination has not been tuned further with the stator converter connected. As a result, there may be room for improvements with regard to mitigating the error in the estimated angle shown in Figure 5.2.

Chapter 6

Self-sensing and voltage model combination

6.1 Motivation for combining the self-sensing and voltage model

Having established that the inclusion of the stator converter in the system model, does not lead to undue influence on the propagation of the field current excitation signal, further utilization of the self-sensing model for position estimation was tested.

As previously discussed in chapter 1, the voltage model, an estimation technique based on utilizing information from the back-EMF, is well suited for medium- to high-speed operation, but fails at lower speeds and standstill due to a lack of back-EMF generation. However, the self-sensing model being solely reliant on the information extracted from the stator responses due to the high-frequency field current signal does not need any back-EMF information. As a result, the method may be used to increase the range of usability for the voltage model by utilizing the position estimate from the self-sensing method to calculate an estimated stator flux, $\hat{\psi}_{ss}$. The resulting stator flux may then be used as a comparator for the estimated voltage model stator flux, and serve to improve the flux estimate. As the voltage model is self-sufficient at higher speeds, this self-sensing and voltage model combination will be utilized for standstill and low-speed operation.

6.2 Stator flux linkage estimate by self-sensing method

In order to calculate the stator flux linkage using the self-sensing method, an alternative per-unit model of the machine will be utilised. The model is based on work done in the master thesis of Grøvan, which was further modified in the project thesis of Bolstad [1, 27]. The alternative pu model modifies the machine flux and voltage equations such that the ex-

pressions only consists of measurable stator currents, due to the damper windings currents having been eliminated from the expressions.

The complete derivation of the alternative pu model is presented in [18], while a summary is given in Appendix F with the equations used to estimate the stator flux linkage reproduced in Equation 6.1 to 6.4 below.

$$\frac{d\psi_{Rd}}{dt} = -\frac{\psi_{Rd}}{T_D} + \frac{x_{Md}}{T_D}(i_d + i_f) \tag{6.1}$$

$$\frac{d\psi_{Rq}}{dt} = -\frac{\psi_{Rq}}{T_Q} + \frac{x_{Mq}}{T_Q} i_q \tag{6.2}$$

$$\psi_d = x_d \sigma_{dD} i_d + \psi_{Rd} + x_{Md} \sigma_D i_f \tag{6.3}$$

$$\psi_q = x_q \sigma_{qQ} i_q + \psi_{Rq} \tag{6.4}$$

The estimation process for the stator flux linkage involves feeding the stator currents in the alpha-beta reference frame and the field current into the self-sensing estimation method discussed in the previous chapter. The estimated rotor position is subsequently used to calculate the d- and q-axis stator currents required for calculating the flux linkages in Equation 6.1 to 6.4. A block diagram depicting the stator flux linkage estimation process based on the self-sensing method is shown in Appendix H.

6.3 Discretization

As all simulations up to this point has been performed for continuous-time operation, and the machine control structure operate under discrete-time the filters and PI-controllers implemented for continuous operation were needed to be discretized.

Using the embedded Matlab function ”c2d” for continuous to discrete-time model conversion, a script was implemented for the transformation process. As there are a plethora of different discretization methods, several tests were performed in order to ascertain which method gave the best results, comparing the estimation capabilites of each method. By trial and error, it was discovered a near negligible difference between the zero-pole matching equivalents and Tustin approximation discretization methods. However, according to Talha and Makda the Tustin method have been shown to give more optimal results compared to matched mapping and least-squared methods [28, p.3].

Consequently, the Tustin approximation method was utilized to discretize all filters and PI-controllers. Bode plots and transfer functions of the filters are shown in Appendix G.

6.4 Tuning

As mentioned in section 6.1, the stated aim of utilising the self-sensing model in conjunction with the voltage model is to provide an additional comparator as a means to correct the stator flux linkage estimate from the voltage model at low speed and standstill, in what is known as correction by feedback. The methodology is described in Figure 6.1, where the block denoted as self-sensing model is the same as discussed in the previous section.

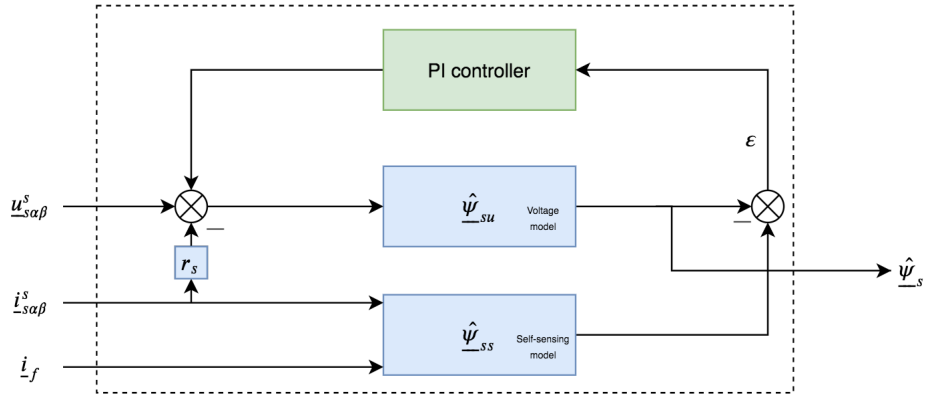

Figure 6.1: The voltage self-sensing model. Adapted from [6]

The operation involves feeding the error between the stator flux linkage estimation of the self-sensing and voltage model into a PI-controller tuned for zero dc-offset. The output from the PI-controller is then fed back into the voltage model to refine the stator flux estimate and consequently the rotor position and speed estimates.

As can be expected, the estimation of rotor position utilizing the correction by feedback methodology described above proved highly sensitive to the tuning of the feedback PI-controller. Slight variations in gain and integrator time constants gave highly varying estimation results, wherein some tuning configurations proved worse than with no PI-controller. Utilizing standard tuning normative for controllers proved insufficient for the given application, and as such a different approach was explored. In order to systematize the tuning, it was decided to utilize the root-mean-square deviation (RMSD), as a means to measure the deviation from measured rotor position for each tuning. RMSD serves to aggregate the magnitudes of the estimated rotor position at each time instance into a single measure. For instance, an RMSD value of zero, although rarely achieved in practice, shows a perfect correlation between estimated and measured values. The method for calculating RMSD is given in Equation 6.5.

$$RMSD = \sqrt{\frac{\sum_{t=1}^{T}(\hat{y}_t - y_t)^2}{T}} \tag{6.5}$$

Using Equation 6.5 initial tests were run with varying integrator time constant and gain to ascertain the best possible tuning of the feedback PI-controller. Given that the applicability of utilizing the self-sensing method is for low-speed and standstill operation, all initial tests were run with a small torque reference of 0.01 pu. The result of the simulations is given in Table I.1. The best initial tuning of the controller with regard to the RMSD value for θ was achieved for $K_p = 0.1$ and $T_i = 0.1$, however, the tuning resulted in significant initial oscillations, suggesting there are some difficulties for the self-sensing model PLL to lock-on and provide a robust position estimate.

As discussed in subsection 4.3.2, it takes approximately 0.5 seconds for the PLL to lock on to the incoming signal, causing some initial transient in estimated rotor position. This transient was initially deemed so small as to be negligible for control purposes, however, when combining the self-sensing model and the voltage model the lock on period followed an underdamped response with a long decay, leading to some time for the position estimate to stabilise itself around the correct path. With the aim of further improving the rotor position estimate, the RMSD methodology was employed concerning tuning of the PI-controller in the PLL. Maintaining constant integrator and gain in the feedback loop PI-controller, while varying the β-value and the lowpass filter cut-off frequency, which due to the usage of symmetric optimum will influence the PLL PI-controller, several simulations were run while calculating the RMSD value for both stator flux linkage and rotor position estimates for each simulation. The results are given in Table I.2. The simulations showed that changes to the lowpass filter cut-off frequency did not yield any improvement in estimated rotor position, while only providing a modest improvement for the flux linkage estimation. As a consequence, no adjustment was made to the lowpass-filter cut-off frequency.

With regard to β, it was found that the optimal value for low RMSD resulting in the best rotor position estimate occurred for $\beta = 20$. Although the value resulted in a slightly worse stator flux linkage estimate, as the aim is to achieve a control strategy allowing for the best overall rotor position estimate and subsequently rotor speed, it was deemed that a trade-off for more accurate position estimate over flux linkage estimate was beneficial. The finalised PI-controller parameters for the PLL is shown in Table 6.1, calculated using Equation 4.20 and 4.21

Finally, additional tuning was performed for the feedback-loop PI-controller in order to maximize the self-sensing model's position estimation capabilites. Again using RMSD to ascertain the relative efficacy of each tuning, it was shown that utilising $K_p = 0.005$ and $T_i = 50$ gave the best rotor position estimation, with the lowest initial oscillations and the fastest steady-state solution of zero estimation error. Table I.3 shows the RMSD values of different tuning configurations.

β	20
T_i (Self-sensing model)	0.3183
K_p (Self-sensing model)	14.0496
T_i (Feedback loop)	50
K_i (Feedback loop)	0.005

Table 6.1: Feedback PI-controller and PLL PI controller values for atan2 based SRF-PLL with 1nd order LPF

As can be seen from Figure 6.2, there are still some initial transients in estimated rotor position, however, given that the transient response is present irregardless of the different tuning configurations and coupled with no dc-offset in steady-state error in estimated rotor position the present solution should prove viable for the given application.

Although utilizing RMSD to ascertain the overall best tuning of the PI-controller in the feedback loop and the PI-controller in the self-sensing model proved useful, the time-intensive nature of running numerous simulations pose a significant drawback with the methodology. As such, the method should only be used if other tuning methods fail to give the desired results. Furthermore, although a given tuning may provide a low RMSD value, it does not take into account other aspects such as ripple and settling time. For instance, although as seen in Table I.2 setting $\beta = 2$ and $T_f = 10$, gave a quite significant reduction in the RMSD value for both the stator flux linkage and rotor position estimates, both signals suffered from a dramatic increase in noise levels. As such, it is recommended utilising the RMSD for tuning purposes as a means to achieve a general overview of the relationship between controller tuning and the desired estimates.

6.5 Results

6.5.1 Low-speed and standstill operation

With the viability of combining the self-sensing and voltage model validated, a comparison utilising the voltage model in conjunction with the current model is warranted. Employing the work of Bolstad, wherein the current model is used in the same manner as the self-sensing model, a simulation was run for the same low torque reference of 0.01 pu.

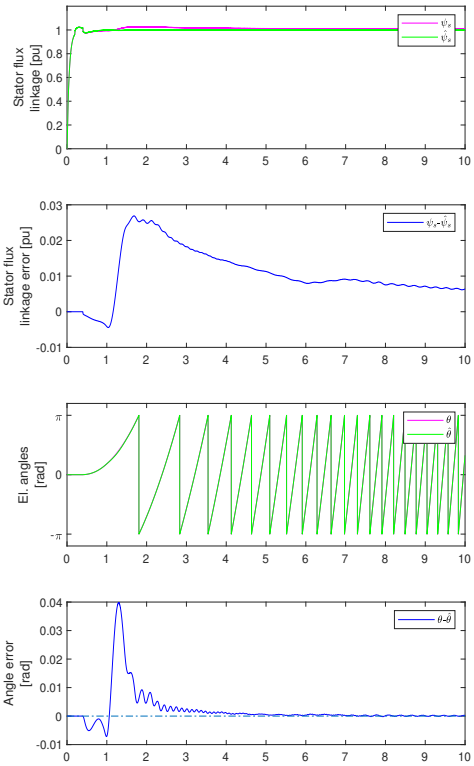

Figure 6.2: Sensorless control with voltage and self-sensing model combination, at low-speed operation

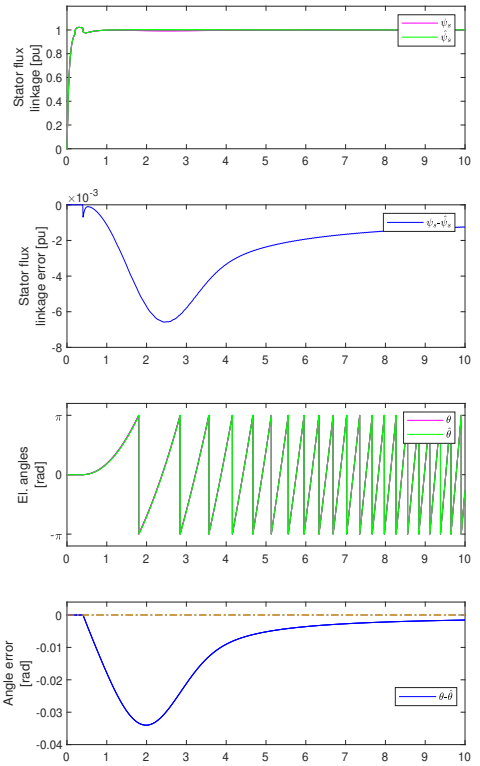

Figure 6.3: Sensorless control with voltage and current model combination, at low-speed operation

As can be seen from Figure 6.2 and 6.3, showing the estimation outputs from the sensorless control, the angle error for the self-sensing and voltage model combination yields a better steady-state response, achieving equilibrium at approximately five seconds, compared to no apparent steady-state for the current-voltage model combination, as it has a

constant dc-offset. There is, however, a larger degree of noise in the self-sensing combination. Yet, given the low amplitude of the noise coupled with the relatively short decay of the initial transients, the noise should not prove a significant challenge concerning control purposes. However, the fact that the peak error for both estimated stator flux linkage and position is higher for the self-sensing and voltage model combination points to some issue with the estimation. Yet, the complete elimination of the steady-state error for the position does pertain to the validity of utilising the voltage and self-sensing model combination.

As discussed above the stator flux linkage error is greater for the self-sensing combination for the entire duration of the simulation, in addition to containing a significantly more noisy signal. Although the increased error and noise does not cause any issues concerning position estimation, the erroneous flux linkage estimate will cause undue influence on the calculation of stator current reference for the current controller. As discussed in section 2.3 the stated aim of the control of the machine is to achieve maximum torque per ampere, which in turn leads to the relation between torque, stator flux linkage and stator current reference shown in Equation 2.31. As such, any error in flux linkage propagates throughout the system and may cause an erroneous stator current reference calculation. Therefore, it is expected for the more significant error and increased noise in the stator flux linkage from the self-sensing voltage model combination to cause a more substantial discrepancy in the stator current reference calculation. Given that the current reference is used as one of the inputs to the digital stator current controller which subsequently is used to decide the switching of the PWM modulator, erroneous flux linkage estimation may lead to controller issues.

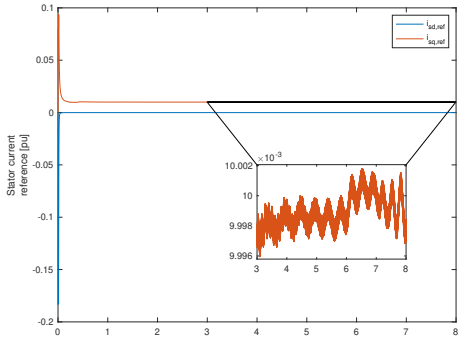

Figure 6.4: Calculated $i_{s,ref}$ from self-sensing and voltage model combination

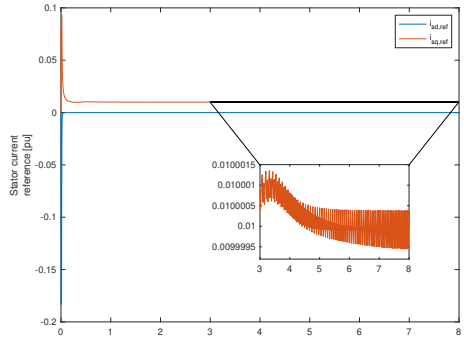

Figure 6.5: Calculated $i_{s,ref}$ current and voltage model combination

Figure 6.4 and Figure 6.5 shows the calculated stator current reference in the dq-reference frame from the two methods. The zoomed-in portion of $i_{sq,ref}$ shows that there is indeed a larger ripple amplitude and increased noise in the current reference produced by the self-sensing method. However, the difference in the results from the two different methods is sufficiently small enough, as to be deemed negligible. The same holds for the d-axis current, wherein the ripple in both cases are near zero.

Given the low magnitude of the ripple in current reference for the self-sensing voltage model combination, it is reasonable to assume that the stator current controller and subsequently the PWM will not see any noticeable challenges compared to the current voltage-model combination at low-speed operation.

Investigation of standstill operation revealed no additional challenges than discussed above. As shown in Figure 6.6 and 6.7, the angle error is sufficiently small for the entire simulation period to be virtually zero. However, the relative sharp increase could pose challenges in cases where the machine is operating under standstill conditions for long stretches of time. Yet, given the application of the synchronous machine in a pumped-hydropower plant it is unlikely that long instances of standstill operation should occur. With regard to the stator flux linkage error, the same conclusions as discussed above is still valid. Although the flux linkage error is substantial higher for the self-sensing voltage model combination, the error should prove sufficiently small enough to not pose any control issues at standstill.

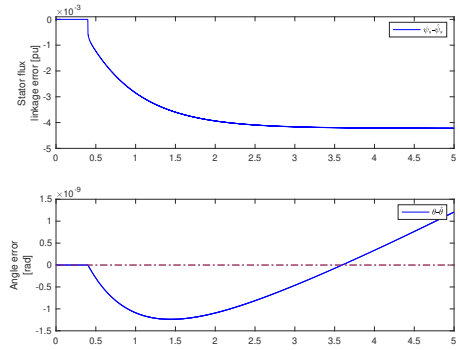

Figure 6.6: Stator flux linkage and position error under sensorless control utilising the voltage and self-sensing model combination, at standstill operation

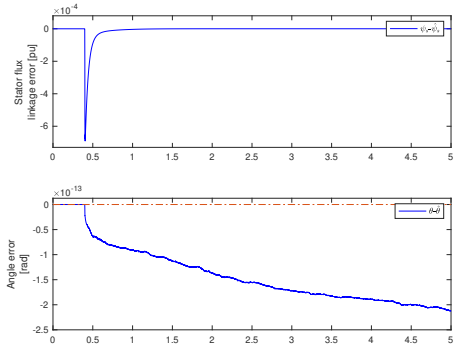

Figure 6.7: Stator flux linkage and position error under sensorless control utilising the voltage and current model combination, at standstill operation

In summation, based on the results discussed above, the difference in estimated stator flux linkage error is deemed sufficiently small as to no give rise to any considerable drawbacks with regard to machine control. Coupled with the enhanced angle tracking capabilities, the self-sensing voltage model combination is deemed validated for low speed and standstill operation.

However, it should be noted that further enhancements could be implemented to achieve a better overall system delivery. These enhancements could come in the form of further dampening of initial transients, which is the primary source of estimation error both for position and stator flux linkage.

6.5.2 Speed traversal

As the self-sensing voltage model combination has been validated for lowspeed and standstill operation, additional simulations were run aiming to investigate the combination's estimation results under more strenuous conditions. Accordingly, the torque reference was implemented to facilitate for a speed traversal as depicted in Figure 6.8.

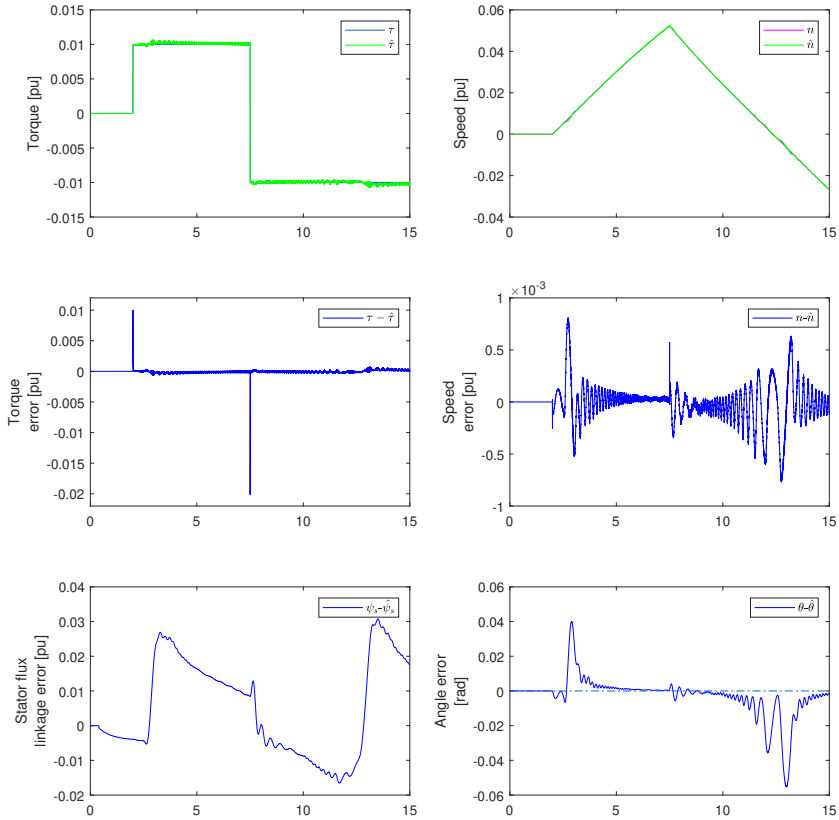

Figure 6.8: Sensorless operation with varying applied torque reference

Figure 6.8 shows the speed is estimated correctly for the entire simulation, notwithstanding oscillations at each step change in the torque. The oscillations in the form of an underdamped response after the step changes are to some degree expected, as the control system quickly attempts to dampen out the variation in speed. However, the time it takes for the response to approach zero suggests that the relative damping of the PI-controller in the feedback may benefit from a higher value, ideally allowing for critical damping

to diminish the oscillations rapidly. Nevertheless, given that the peak error in estimated speed, occurring at the first positive step in torque reference, is approximately $8 \cdot 10^{-4}$ pu coupled with a relatively quick damped response the speed estimate should in theory prove sufficiently accurate.

Examining the stator flux linkage error, shows no notable difference concerning peak values compared to the low-speed operation shown in Figure 6.2, once more suggesting no apparent issues with regard to stator current reference calculation, as discussed in subsection 6.5.1. However, given the amount of time it takes the error to stabilise itself, no apparent steady-state solution is achieved.

Concerning position estimation, it can be seen from Figure 6.8 that the position is successfully estimated for the entirety of the simulation. However, it is explicitly clear from the figure that the source of the most substantial errors is due to the speed crossing through zero. The zero-crossing is a well-known issue for the estimation techniques based on the back-EMF, due to a lack of EMF information at standstill. Part of the motivation for utilising the voltage model in combination with the additional signal from the field excitation current is that no-back emf at standstill and speed zero-crossing should be required to estimate the rotor position accurately. Alas, as discussed in the previous chapter, no inherent issue with the combination is apparent at standstill with zero torque applied. Meanwhile, the resulting oscillations in Figure 6.8 shows that the problems at zero-crossing are present, which in some sense negates the usage of the self-sensing model.

Once more utilising the voltage-current model combination as a reference point, it is clear from Figure J.1 that the self-sensing voltage model combination does achieve an overall more accurate rotor position estimate, with a peak error of 0.06 rad or 3.44° compared to 0.08 rad or 4.58° for the current-voltage model combination, alluding to a slightly more robust zero-crossing characteristic. Moreover, the dc offset is once more completely eliminated with the self-sensing method. However, the increased harmonics in estimated position and subsequently stator flux linkage is directly correlated to the increased noise in torque and estimated speed. The connection between torque ripple and stator current and flux linkage is reflected in Equation 2.29, while the connection between speed ripple and estimated position is given by Equation 4.3.

Although torque ripple will naturally occur in any electrical machine due factors such as rotor asymmetry or mechanical imbalances within acceptable limits, the added torque ripple as a result of the stator flux linkage and current harmonics from the self-sensing voltage model combination may pose a challenge for drive operation. One of the challenges imposed by the increased torque ripple is increased vibrations, which, in turn, may lead to a reduction in the lifespan of the machine, as well as needing more maintenance. As one of the reasons for the implementation of sensorless control is to reduce system costs, it is clear then that the risk of increased vibrations may serve to lead to higher compounded overall system costs, once more negating the usage of the self-sensing methodology.

Notwithstanding the enhanced position estimation of the self-sensing voltage model

combination, the fact that the speed estimate is significantly worse than for the current-voltage model combination alludes to the need for a better system tuning.

In an attempt to mitigate the signal noise in estimated position and stator flux, the cut-off frequency of the PLL lowpass filter was lowered as the noise had a frequency of approximately 2 Hz. However, a problem with the inherent lack of combining both good filtering performance and fast dynamic response, which has been extensively discussed in subsection 4.3.2, was encountered. As the bandwidth of the PLL becomes lower, decreasing the cut-off frequency and increasing the filtering capabilities, the dynamic response becomes slower. With the slower dynamic response, the PLL is unable to lock-on to the incoming signal causing constant erroneous position estimation in the self-sensing model, which translates through the system to worse estimation performance for the voltage model. The relation between the lowpass filter cut-off frequency and the dynamic response can be visualised by plotting the step response of the PLL.

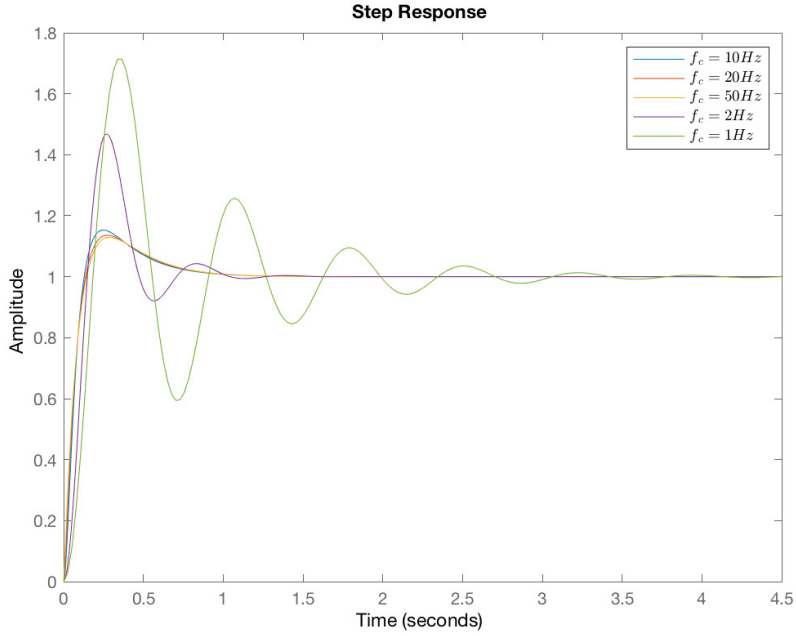

Figure 6.9: Step responses for closed loop PLL, with varying lowpass filter cut-off frequency

Figure 6.9 shows the step responses of the closed-loop PLL. It is clear that the higher the cut-off frequency of the lowpass filter, the lower the overshoot of the closed-loop response. Furthermore, a higher cut-off frequency gives a significantly faster settling time as well as nigh on no oscillatory behaviour, more closely resembling a critically damped response. Relating the step responses to the duality of good filtering and fast dynamic

response for the PLL, it is clear from Figure 6.9 that achieving the desired filtering of the 2 Hz component while still having a fast dynamic response is highly challenging for the present configuration.

6.6 Second-order lowpass filter

In an attempt to remedy the issues discussed in the previous section, a second-order lowpass filter was implemented instead of the first-order filter previously used. Given that the only available parameters available for tuning using the first-order filter is the filter time constant and β-value as a result of symmetric optimum, the reasoning behind introducing a second-order filter is the ability to tune the relative damping of the filter which could lead to better relation between filtering and the dynamic response. The transfer function for the second order lowpass filter is given in Equation 6.6.

$$h(s) = \frac{\omega_n}{s^2 + 2\zeta\omega_n s + \omega_n^2} \tag{6.6}$$

The relative damping, ζ, was set to $1/\sqrt{2}$ to facilitate for critical damping, aiming for the criteria of a well-designed PLL laid out in [25] and discussed in subsection 4.3.2.

Moreover, extensive tests were run to ascertain the natural frequency, ω_n, which resulted in the lowest PLL bandwidth allowing for the most accurate position estimation. A too-small ω_n resulted in a highly unstable system. At the same time, a higher natural frequency reached a point of diminishing return wherein no added benefits with further increases to ω_n concerning the dynamic response of the PLL were experienced.

Thus, the second-order lowpass filter natural frequency was set to 10 Hz, resulting in a cut-off frequency of 10.0264 Hz.

With the second-order lowpass filter parameters set, further changes were done on the PLL PI-controller. Once more running extensive simulations in order to facilitate for a best overall tuning. Due to the introduction of the second-order lowpass filter, symmetric optimum is no longer valid as a tuning regiment. As such trial and error was employed, utilizing a combination of step responses to ascertain the dynamic response of the PLL and Simulink simulations to verify accurate position estimation. The tuning of the PI-controller resulting in the best overall angle tracking capabilities of the PLL is shown in Table 6.2.

The resulting bandwidth of the PLL as a result of the tuning given in Table 6.2 is set at 3.5059 Hz, meaning that the 2 Hz harmonic in estimated position and stator flux linkage has not been eliminated. Yet, seemingly no other tuning offered a similarly low bandwidth while providing a sufficiently accurate PLL rotor position estimate.

Finally, having altered the PLL, an additional round of tuning on the feedback PI-controller was performed. It was discovered that the lower the integrator, the better the estimation process became. In fact, complete omission of the integrator term gave the overall best result, with the steady-state stator flux error entirely eliminated as shown in Figure 6.10. As such, the feedback control consists solely of a single gain.

The connection between the omission of the integrator term and the improved estimation capabilities of the voltage self-sensing model combination does not align with the general knowledge on PI-controllers. As discussed by Kiam Heong Ang et al., increases in the integrator are directly correlated to a significant decrease in steady-state error [29]. However, by completely eliminating the feedback integrator the steady-state error in the stator flux linkage is eliminated. Furthermore, increasing the value of the integrator term is also correlated to an increase in settling time, which once more is the opposite result achieved with the single gain wherein the settling time for the position error has decreased.

ζ	$1/\sqrt{2}$
ω_n	$2 \cdot \pi \cdot 10$ rad/s
T_i (Self-sensing model)	0.1273 s
K_p (Self-sensing model)	22.2144
K_p (Feedback loop)	0.002

Table 6.2: Feedback PI-controller and PLL PI controller values for atan2 based SRF-PLL with 2nd order LPF

6.6.1 Results

The concern of the lack of integrator term in the feedback PI-controller notwithstanding, comparing Figure 6.2 and Figure 6.10 shows a marked improvement in both estimated stator flux linkage and rotor position.

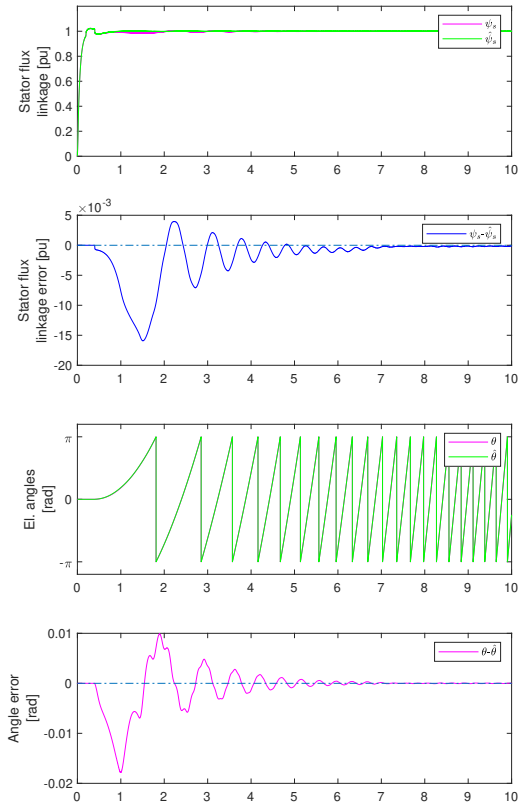

Figure 6.10: Sensorless operation with voltage model and self-sensing method combination after re-tuning. Torque reference of 0.01 pu

With regard to estimated flux linkage, the steady-state error has been eliminated, in addition to a reduction in peak error of almost half compared to using the first-order lowpass filter. The same trend is apparent from the estimated position, wherein the peak error also has been halved.

Concerning operation under varying torque reference, the new tuning regiment has

significantly enhanced the estimation processes across the broad. As seen in Figure 6.11, a marked improvement in the position estimate has in turn lead to a solid decrease in the speed error compared to the previous tuning depicted in Figure 6.8, with the error clustered around the range of $-2 \cdot 10^{-4}$ to $2 \cdot 10^{-4}$ pu.

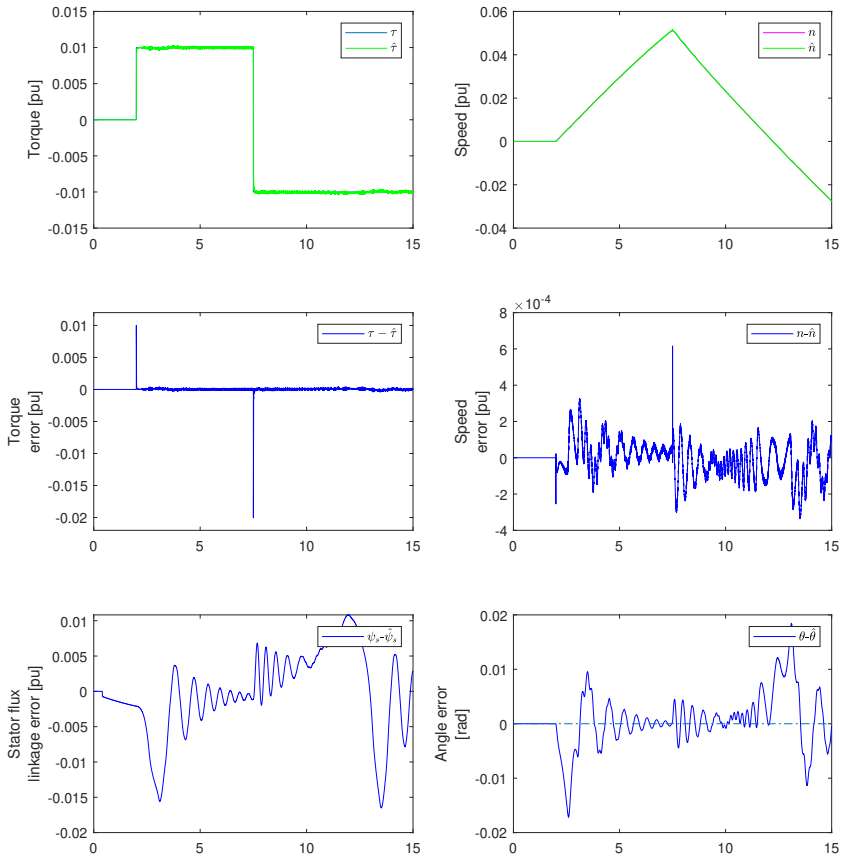

Figure 6.11: Sensorless operation with varying applied torque reference, after re-tuning

Similarly, removal of the stator flux linkage dc-offset is achieved notwithstanding the oscillations at steps in torque and speed zero crossings, once more alluding to a better configuration of tuning parameters.

Once more comparing the self-sensing voltage model combination to the current-voltage model, it is clear that a sufficiently low position error has been achieved validating

the usage of the self-sensing model, instead of the more commonly used current model at low-speed operation. As can be seen from comparing Figure 6.11 and J.1 the usage of the self-sensing model reduced the peak error by a factor of 4, with peak error of 0.02 compared to 0.08 for the current model.

Yet, the enduring problem of the harmonics presents a seemingly insurmountable obstacle to attack. Having pushed the PLL bandwidth to the lowest possible frequency, while still maintaining accurate position estimation, suggests that the usage of the PLL in itself may not be the best technique available. As noted by Uzel et al., the arctan calculation of position is highly sensitive to measurement noise [5]. With the further addition of the sine function in the PLL, it is clear that there is the potential for added noise as a result. Furthermore, although the SRF-PLL is the epitome of simplicity, it also suffers from a constraint in the form of the PI-controller. As discussed in subsection 4.3.2, without the inclusion of the atan2 function it was impossible to acquire a tuning for the controller which allowed for a broader range of operation than $\pm 10\%$ of initial tuning. With the atan2 function this range was extended, which as a consequence allowed for accurate position estimation in the case of speed traversal. Alas, this is reflected in the literature wherein it is noted that the traditional PLL suffers from a lack of good dynamic performance [30]. While the utilised PLL with atan2 has been shown to increase the range of operability compared to the other tested PLL structures, it still lacks sufficient dynamic range to be called a complete success.

Yet, the drastic reduction in peak error for both stator flux linkage and position estimates does pertain to the usage of the additional field excitation signal for position estimation. While the magnitude of the oscillatory behaviour of the harmonics is pronounced at the immediate onset of machine rotation, the settling time of the signal is such that after four seconds the peak to peak error for the self-sensing voltage model is set at approximately 0.001 rad or 0.057°, for the case with 0.01 pu torque reference shown in Figure 6.10. Compared to the current-voltage combination, the error at the same time instance is approximately 0.01 or 0.57°, a tenfold reduction. Coupled with the fact that both the stator flux linkage and position estimate show no sign of a steady-state no DC offset solution, it is clear that the usage of the additional field excitation signal for estimation purposes is well justified.

Chapter 7

Self-sensing, current and voltage model combination

Having established the foundation for utilising the self-sensing methodology as a corrector for the voltage model at standstill and low-speed operation, and proven how the combination gives an overall better result with regard to estimation than the current-voltage model combination, an aggregate of all three models operating under different speed regiments was implemented.

The methodology utilizes the self-sensing model as a corrector for the voltage model at standstill and low-speed operation, and it includes a hand-off to the current model at a speed wherein the current model estimation outperforms the self-sensing model. The motivation for combining all three methods for estimation purposes is to achieve a full range of drive operability. The self-sensing model, utilizing the additional field excitation signals is not reliant on any back-EMF information, as opposed to current and voltage model, making the model perfect for standstill and very low-speed operation. The current model's estimation efficiency is dependent on the speed of the rotor, with the highest resolution estimates occurring at low speed, as discussed in Equation 4.4. Finally, the voltage model performs best in the higher speed range where sufficient back-EMF information is available. By combining all three methods, the aim is to allow for complete operability of the synchronous machine, regardless of its speed.

7.1 Speed dependent gain

As the self-sensing model has been proven more robust for estimation purposes at standstill and low-speed operation compared to the current model, a speed-dependent gain was implemented wherein the estimated speed of the rotor will be used to concurrently initialise and increase the current model as the rotor speed increases and decrease the self-sensing model. The aim of increasing the current model linearly rather than a hard switch-over at

a given speed is to achieve synergistic effects as both models may serve to increase the robustness of the estimations.

The hand-off procedure from self-sensing model to the current model is depicted in Figure K.1. The output to the voltage model consists of a combination of both the self-sensing and current model, with the partitioning of each model's influence decided by the desired speed for hand-off, denoted as n_{ho}.

A potential drawback of making the stator flux linkage input to the voltage model dependent on estimated speed is that any error in speed estimate will cause undue influence on the voltage model estimation process which may serve to exacerbate any errors in the estimation process. However, as discussed in the previous chapter, the error in speed estimate is so small as to suggest a negligible impact on the voltage model estimation.
The hand-off speed was set to 0.125 pu, due to the current model estimation capabilities increasing with the speed of the motor and the self-sensing model having better tracking capabilities for low-speed operation.

7.1.1 Results

Figure 7.1 depicts lowspeed operation with the combination of self-sensing, current and voltage (SSCMVM) model.

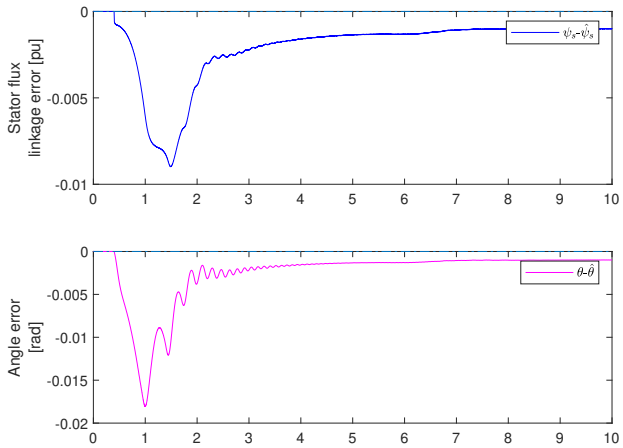

Figure 7.1: Sensorless operation with voltage, current and self-sensing model. Torque reference of 0.01 pu

As seen in Figure 7.1 by combining the self-sensing and current model the desired synergistic effects is clear with regard to estimated stator flux linkage, as the peak error has been approximately halved when compared to only running the self-sensing model as shown in Figure 6.10. Concerning position estimation, no discernible difference in peak error can be seen; however, the oscillations have been markedly reduced. An additional point present in the above figure is that there seems to be a reduction in the movement

toward zero steady-state error in the time range of 5-6 seconds, which is directly correlated to the current controller providing the bulk of the output to the voltage controller. As one of the main points in the rigorous tuning of the self-sensing PLL and the feedback PI-controller has been to reduce the steady-state error, it is clear then that the hand-off speed could be set somewhat higher. However, given the narrow bandwidth of the PLL, the problem of dynamic performance and proper filtering once more pose a challenge. A higher hand-off speed for switching between the two models would mean that the self-sensing model would be required to operate and provide the bulk of the feedback to the voltage model for a larger speed range. Seeing as the PLL is severely limited by its balance between dynamic performance and filtering, a higher hand-off speed would require other means of angle tracking, for instance, a secondary PLL with the lowpass filter attuned for higher frequencies.

Having validated the combination off all three models for low-speed operation, a more complex motor operation was implemented. As the bandwidth of the PLL in the self-sensing model as of now has limited the simulations to low-speed and standstill operation, the inclusion of the current and voltage model now allows for a significantly larger swath of speed operation.

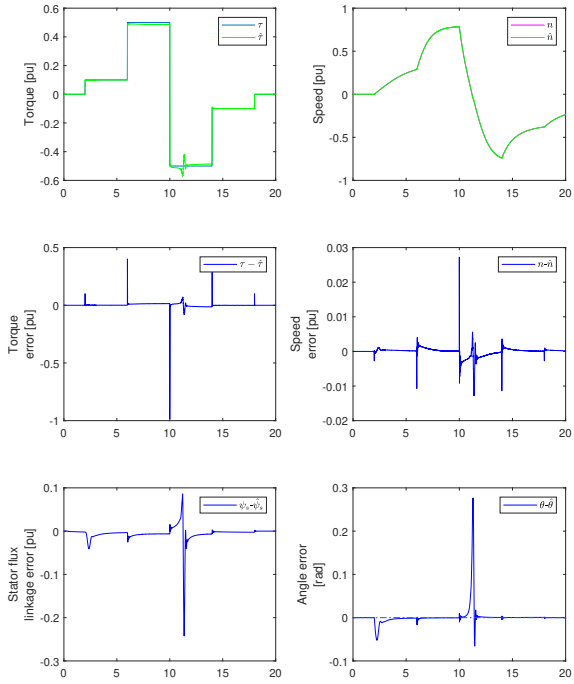

Figure 7.2: Sensorless operation with varying applied torque reference for wide speed range operation, self-sensing, voltage and current model combination

Figure 7.2 depicts the results of the sensorless operation with the self-sensing model running solely as a corrector to the voltage model at standstill, with the inclusion of the current model for low-speed operation.

All relevant values are, for the most part, successfully estimated for the entirety of the simulation. The notable standouts are the rather significant spikes in torque and speed error at the critical points, i.e. step-change in torque and discontinuity in speed estimated. It should be noted that for both cases the largest deviation is eliminated after approximately 2 ms, and should as such not pose any significant issues.

The same large spikes in deviation are also present in the stator flux linkage and position error, both occurring at the time of speed zero crossing. As the main point of utilizing the self-sensing model in the current configuration is precisely to mitigate estimation errors at zero crossings, given the low resolution of back-emf information, the presence of large spikes in error suggests some malfunction in the self-sensing PLL. Alas, this fact is reflected when comparing the case above with the model only utilizing the current and voltage model shown in Figure J.2. Inspection of the two figures shows a lower estimation error in the position estimate at the initial ramping up of speed with the self-sensing model

utilised, while a comparatively high difference in peak estimation error for both stator flux linkage and position can be seen as the speed approaches zero with the step from positive to negative torque reference, alluding to positive feedback from the self-sensing PLL.

Specifically, it was revealed that the enduring issue at the zero crossing is manifested as the PLLs inability to resynchronize as the speed once more is within the tuned PLL bandwidth. The resynchronization failure caused a complete distortion of position estimate from the self-sensing model, making it useless at speed zero-crossing. With the main point of using the additional field excitation signal to estimate the position at precisely speed zero-crossing, makes the resynchronization error a fatal flaw of the self-sensing model in its present state.

Given that the PLL has been rigorously tuned to achieve the best possible combination of dynamic performance and good filtering capabilities, there is no apparent solution to enable the PLL to lock on the incoming signal once the speed and consequently frequency is within the PLL bandwidth. As such other avenues of attack once more had to be considered.

7.2 PLL alternatives

Due to the failure of the PLL to resynchronize once the speed of rotor and as such the frequency of the estimated position signal is within the PLL attuned bandwidth, it was clear that the PLL in its present configuration was not a viable option allowing for machine operation in a wide variety of drive requirements. Given the substantial amount of work done on the PLL, it was decided to focus on estimation processes within the same classification. Consequently, other estimation methods, such as Kalman-filter will not be considered.

Building on the idea of the hand-off procedure from the self-sensing to the current model, an attempt were made at implementing a speed-dependent gain for the PLL PI-controller. The reasoning was that by making the gain dependent on speed, the bandwidth of the PLL would be dynamic, meaning as the speed increases and thus the electric frequency, the bandwidth would increase appropriately. However, it became immediately clear that the coupling of PI-controller gain and speed drastically increased the complexity of the tuning of the PLL. As previously discussed, the PLL tuning has mostly consisted of trial and error, based on the relevant controller theory and RMSD-values. With the increased system complexity with the speed-dependent gain, this tuning regiment proved too time consuming. However, utilizing the D-partitioning technique which was implemented in the finalised design, could serve to provide a foundation for the implementation of the speed-dependent gain.

Given the proclivity of PLL for estimation purposes in sensorless control schemes, a brief literature study gave numerous alternative PLL configurations. One option which did seem promising was to utilise two PLLs in conjunction in what is known as a Dual Phase-locked Loop (D-PLL) estimation scheme. As discussed in [7], many traditional SRF-PLL estimation schemes may fail to lock on to the incoming signal with no steady-state in cases where the input is a frequency ramp, which is the exact case with the failure of resynchronization discussed in section 7.1. The authors posit the D-PLL as an alternative

to combat the issue described above.

The block diagram of the implemented D-PLL is shown in Figure L.1. The implementation aimed to maintain as much as possible of the previous PLL iterations, i.e. the values shown in Table 6.2, to mitigate the complexity of the tuning regiment. As such, no changes were made to the second-order lowpass filter and PI-controller.

However, simulations with the implemented D-PLL showed no improvement from the single PLL iteration, suggesting no transferability of PI-controller gain and time constant. Instead of the second-order filter, [7] utilize a cascading pre-filter where each filter is tuned to accommodate a different bandwidth. According to the authors, a direct application of the D-PLL may serve to degrade the performance of the system as a whole, with the cascading pre-filter implemented in order to reduce the effects of non-linearities. As such, the implementation of the D-PLL, based on the previously extracted tuning was deemed too simplistic to allow for good estimation capabilities.

As the main point of contention with regard to achieving an efficient PLL has been the rigorous tuning of the lowpass filter and PI-controller, to find the best combination of dynamic performance and good filtering it was decided to omit the transfer-function based lowpass-filter entirely in favour of a moving-average filter (MAF).

7.3 MAF-PLL

As discussed in [8], the tuning of the lowpass filter used in the PLL is in itself a contradiction, as there exist two competing necessities simultaneously; a larger bandwidth to accommodate a fast dynamic response and a reduced bandwidth to minimise the high-frequency harmonic elements, which the authors describe as "...contradictory and torturous" [8, p.44].

As a solution to this paradox the authors in [8] suggests the omission of transfer-function based lowpass filter is substituted with a MAF. The block diagram for the specific MAF utilised is depicted in Figure M.1. The difference equation in the discrete time domain is thusly given by Equation 7.1.

$$\hat{X} = \frac{1}{N}\frac{1-z^{-N}}{1-z^{-1}}X(z) \tag{7.1}$$

As can be seen from Figure M.1 and Equation 7.1, the structure of the MAF is simple, and contains only one parameter, N, which is given by Equation 7.2.

$$N = \frac{T_w}{T_s} \tag{7.2}$$

Where T_w is the windows length of the MAF, for the present case, the windows length is set at $1/300$ s, i.e. related to the frequency of the high-frequency field excitation current signal. With a sampling time of $1/6000$ s, the N value is thus set at 20. By the usage of the MAF as a phase detector instead of the lowpass filter, the harmonics are eliminated, while avoiding the negative effect of the filters. Furthermore, as will be further discussed

in conjunction with the D-partitioning technique, the MAF allows for a greatly increased tuning availability while maintaining the stability margins.

7.3.1 D-partition technique

In [8], the authors present an improved method of visualising the tuning of the PLL PI-controller with regard to stability margins known as the D-partitioning technique. The technique allows for controller design which ensures closed-loop stability with the required phase margin.

The methodology consists of calculating the gain and time constant of a closed-loop feedback system transformed to the frequency domain with PI controller and single-input single-output (SISO) plant, for a large range of natural frequencies. A D-curve can subsequently be plotted for parameters of gain and time constant. The extraction of the part of the D-curve which corresponds to desired phase margin can finally be calculated by moving an intersection point from unity circle by an amount set by said phase angle.

According to [8], the transfer function for the MAF is set as shown in Equation 7.3, where the integrator has been included for the present case.

$$h_{MAF}(s) = \frac{2T_w^2\omega_h^2}{(T_w s + 2)\left((T_w s + 2)^2 + 4T_w^2\omega_h^2\right)} \cdot \frac{1}{s} \tag{7.3}$$

Where ω_h is the frequency of the additional signal in the field excitation winding, and T_w is the windows length of the MAF, which is given by ω_h.

As presented in [31, 32], by transforming Equation 7.3 to the frequency domain, denoting the numerator of $h_{MAF}(s)$ as $B(j\omega)$ and the denominator as $A(j\omega)$ and $\omega \in [0, 6000]$ Hz, the PI-controller parameters can be calculated by Equation 7.4 and 7.5.

$$K_p = real\left\{(-x - jy)\frac{A(j\omega)}{B(j\omega)}\right\} \tag{7.4}$$

$$K_i = imag\left\{(-x - jy)\frac{A(j\omega)}{B(j\omega)}\omega\right\} \tag{7.5}$$

Where K_i is the integrator constant commonly used instead of the time constant for controllers, and the relation between gain, time constant and integrator constant is given by Equation 7.6.

$$T_i = \frac{K_p}{Ki} \tag{7.6}$$

x and y serve the purpose of moving the intersection point from unity circle to the region provided by the phase angle ϕ and is given by Equation 7.7 and 7.8.

$$y = sin(\phi) \tag{7.7}$$

$$x = \sqrt{1 - y^2} \tag{7.8}$$

Choosing the desired phase margin of 60°, the Neimarks method can be utilised to calculate the PI-controller parameters of the MAF based phase-locked loop, MAF-PLL. Furthermore, in order to compare the MAF-PLL to the other PLL versions, the D-partitioning technique has been utilized to calculate the stable controller parameters for the first-order and second-order lowpass filter, henceforth denoted as FOLPF-PLL and SOLPF-PLL, with the same values as presented in the previous chapters. The controller parameters for the different PLLs are shown in Figure 7.3.

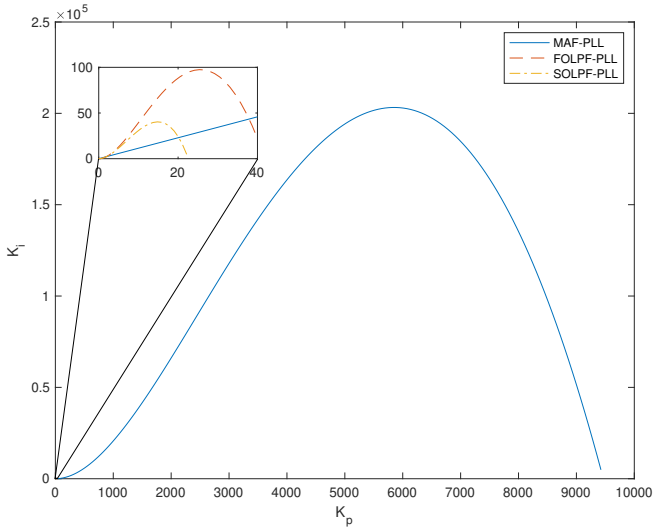

Figure 7.3: Calculated PI-controller parameters by Neimarks D-partition method

The usefulness of the D-partitioning technique cannot be overstated, as the tuning of the PLL now has reference points for the stability of the system, greatly reducing the amount of guessing involved. In Figure 7.3, all controller parameters under the graphs is ensured to lead to a stable closed-loop system, with a phase margin of 60°. It is seen that the MAF-PLL offers a significantly larger range of stable controller parameters than is available for the traditional lowpass filters, with the SOLPF-PLL having the lowest stable range of controller parameters. As a result of the increased choices for controller parameters, a larger range of PLL stable bandwidths for the closed-loop system may be implemented, which in turn should lead to a lessening of the issues discussed previously regarding good filtering and fast dynamic response.
Having calculated the PI-controller parameters, which is within a stable region, the bandwidth of the closed-loop system as a function of the gain and time constant can be plotted, as shown in Figure 7.4.

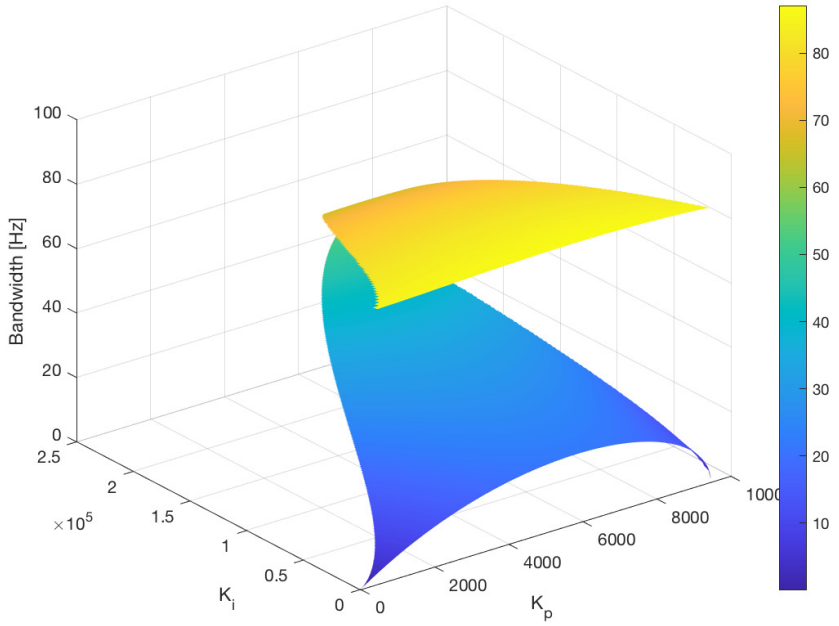

Figure 7.4: PLL bandwidth as a function of K_p and K_1, calculated using the D-partitioning technique

As the bandwidth has been calculated to accommodate only stable controller parameters, all values depicted in Figure 7.4 should in theory result in a stable closed-loop system. However, testing with different controller values revealed that as with the FOLPF-PLL and SOLPF-PLL a too high bandwidth resulted in deteriorating rotor position estimation, as is to be expected given the inherent limitations of the PLL-structure. Yet, compared to the FOLPF-PLL and SOLPF-PLL, shown in Figure N.1 and N.2, where the maximum allowable stable bandwidth is set at approximately 0.6 Hz and 0.3 Hz respectively, the MAF-PLL offers the ability to choose from a significantly larger range of stable PI-controller parameters for higher bandwidths. As the bandwidth of the PLL is closely related to angle tracking capabilities at different speeds this larger range should then offer a remedy to the desynchronization issues faced with the second-order lowpass filter.

7.3.2 Speed traversal

With the D-partitioning technique tuning of the MAF-PLL was vastly simplified, as the amount of guesswork involved in finding compatible controller parameters is greatly reduced. However, the process of tuning the PLL is still a time-consuming process requiring substantial running of simulations to find the best possible combination of parameters. Us-

ing the plot depicted in Figure 7.4, the MAF-PLL values were set as shown in Table 7.1.

N	20
K_p	225.4
K_i	1249
Bandwidth	2.2 Hz

Table 7.1: MAF-PLL values

With the MAF-PLL values set as above, the sensorless control scheme was tested for a new wide speed range operation. Alas, it became immediately clear that the MAF-PLL did not solve the issue of re-synchronising at zero-crossing when the speed is within the PLL bandwidth, as discussed in section 7.1. Although the rotor position estimation was somewhat improved at zero-crossing from the case with the second-order lowpass filter validating its usage, the MAF-PLL performed significantly worse than the current model, which once more negates the use of the self-sensing model. Given that the same issue has manifested itself for several different versions of PLLs, the question necessarily arises as to what is causing the lack of resynchronization.

It was noted that the degree of synchronization is directly correlated to the magnitude of the torque reference through the zero-crossing, as the position estimate was proven increasingly accurate running several simulations at decreasingly lower step magnitudes in torque. A smaller step in magnitude means that the acceleration of the rotor through zero-crossing is lower, which could mean more time for the PLL to latch on to the incoming signal.

As discussed in subsection 4.3.2, there are specific conditions that must be meet if a PLL fails to lock on to the incoming, reproduced below for ease of reading.

- Higher-order or subharmonics in the input signal.
- One of the above harmonics have a frequency close in range to the initial PI-controller output.
- A larger difference in target fundamental frequency and PI-controller output than lock range.

An investigation into the inputs to the self-sensing model, namely stator current and field current, revealed no significant changes in harmonics at the time of zero-crossing, testing for several different magnitudes of torque references. Further investigation revealed that the issues stem from an increasingly erroneous position estimate from the atan2-function, of such a magnitude that the lowpass-functionality of the PLL is insufficiently able to filter out the noise.

As previously discussed the atan2-function is highly sensitive to measurement noise, and as will be discussed in the next section a complete omission of the atan2 function massively improved the position estimation capabilities of the PLL at zero crossing.

7.4 Re-calibration of self-sensing model and new method for improved zero-crossing estimation

Having tested an extensive amount of different PLL topologies, it was clear that the PLL would not provide an accurate estimate for rotor position in a wide variety of speed operations without some alterations. Hence, starting with the bandpass filters, an effort was made to extract the best performance from each self-sensing model section.

The bandpass filters have been tuned with a quality factor of 0.4, which results in a relatively shallow passband, which in turn may lead to a reduced ability to suppress harmonics. As discussed above, the presence of harmonics in the input signal is directly correlated to the PLLs ability to lock on to the incoming signal. However, a too narrow bandwidth will cause a reduction in the self-sensing model's capacity to derive useful information. After extensive tests, it was found that a quality factor of 0.707, gave the overall best results concerning position estimation from the PLL. While a higher quality factor would serve to decrease input harmonics to the PLL, it was found that further increases reduced the quality of the position estimation.

Furthermore, regarding the feedback PI-controller from the self-sensing to the voltage model, the introduction of the MAF-PLL has solved the conundrum discussed in section 6.6. Previously, it was discovered that a complete omission of the feedback integrator gave the best estimation capabilities for the voltage model. As one of the functions of the integrator is to decrease steady-state error, the fact that eliminating it gave the best result goes counter to the theory of control systems. However, with the MAF-PLL it was discovered that the introduction of the integrator did yield the expected reduction of steady-state error, resulting in improved estimation.

Concerning the issue of resynchronization at speed zero-crossing, several attempts were made at implementing a reinitialization control, wherein the integrator of the MAF-PLL was disabled for frequencies higher than the bandwidth of the PLL and re-enabled when the frequency once more approaches PLL attuned values. The control strategy involved utilising the position estimate from the current model as the initial angle for the PLL integrator at a time instance decided by the speed of the rotor at which the electric frequency is within PLL bandwidth.

Although the methodology did offer some reprieve at the immediate onset of reinitialization, as the estimated position initially followed accurately along the measured angle, it quickly lost synchronicity once more at the onset of zero-crossing.

Finally, a solution to the zero crossing issue presented itself in the implementation of the strategy presented in [8], by completely bypassing the bandpass and lowpass filters. Instead, the stator currents are fed directly into $\alpha\beta$ to dq-transformation block, where the resulting q-axis stator current is multiplied with the sine of the field current. The complete Simulink topology is presented in Figure O.1. Although this method leads to a highly unstable initial position estimate, after the initial transients has been eliminated the PLL never loses synchronicity and thus solves the problem with the previous methodologies.

A peculiarity with the methodology shown in Figure O.1 is that the position estimate becomes out of phase-dependent on the derivative of the rotor speed. For a positive speed derivative, the PLL estimated position is 180° phase-shifted from the measured position, while a negative speed correlates to measured and estimated position entirely in phase.

To remedy this, a solution is to estimate the position in two separate loops with one adding π to the field current before the sine-function in order to phase shift the estimated position by 180°. To decide which of the loops is correct at any given time step, a hand-off method dependent on the slope of the speed estimate was tested. For a positive speed slope, the normal sine-function is utilized and vice versa. However, given that the estimated speed is prone to sudden dips due to estimation errors, this hand-off procedure causes some unwanted results wherein the wrong PLL loop was initialized wrongly due to a slight sign shift in the slope of the speed.

A more robust hand-off procedure was therefore implemented by using the RMSD value for both loops. Using Equation 6.5 and the voltage model position output as the comparably stable comparator, the RMSD values of each loop is calculated and continually compared. When each loop is in phase its RMSD value, as it is a measure of deviation from a baseline, is necessarily the lowest. When a change in speed derivative occurs and the phase changes the hand-off procedure then changes from the PLL loop out of phase to the in-phase loop.

Figure 7.5 shows the position estimation of the MAF-PLL, where the top plot depicts the loop without phase-shifting, and the middle the one where the sine of i_f has been phase-shifted by 180°.

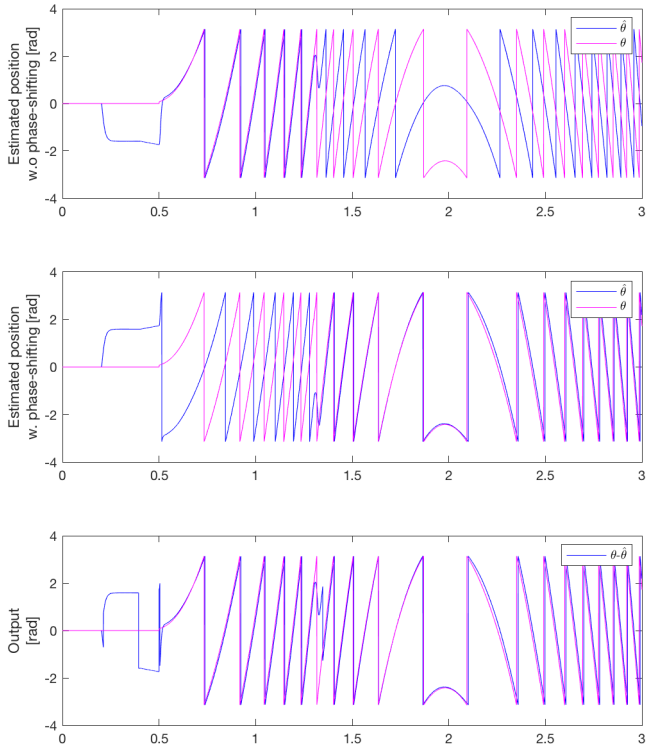

Figure 7.5: Sine of i_f based MAF-PLL, with and without phase-shift, and output when corrected by RMSD calculation

Figure 7.5 shows that by combining the two loops, the range of position estimation has been dramatically extended, compared to the atan2-based MAF-PLL, notwithstanding the initial transients. The initial transients were attempted eliminated through changing the enable-signal to the PLL integrator to occur at a later time instance, to no avail. However, given that the MAF-PLL utilising the atan2-function as input has been proven to offer good estimation at startup, by combining the two methods, a complete estimation process for the self-sensing model may be implemented. The methodology involves utilizing the atan2-based PLL at initial ramping up of speed, and switching to the sine of i_f based PLL at higher speeds. By once more utilising the RMSD calculation, the hand-off procedure from atan2-based to the sine of i_f based estimation, is performed by comparing the RMSD-value of each method and switching between them when each achieves the lowest value.

A possible drawback of utilising the RMSD calculation for the hand-off procedure is the need for storing various values, namely the estimated position of each loop, the elapsed time and the current model estimate. Consequently, as the running of the control

system progresses the amount of storage needed is ever increasing. However, given that the atan2-based estimation only outperforms the other techniques at startup a toggle may be designed which turns the memory storage on and off dependent on different modes of operation greatly reducing the need for memory storage. Furthermore, the presence of three different PLLs will increase the computational costs of the control system if it is to be run as a software-based digital signal processing based (DSP) motor drive. Nevertheless, the relative simplicity of the PLL compared to other estimation methods may alleviate some of the extra computational costs if compared to other techniques such as angle-tracking observer (ATO) or Kalman filters.

As seen in Figure 7.5, there are some discontinuities at the hand-off from the different loops, which will cause an added error in the position estimate. However, as these discontinuities occur for peaks in the speed of the rotor, positive and negative, either at a low speed wherein the atan2-function is operating solely, or at higher speeds where only the current and voltage model is operating, no added problem related to estimation should occur. The complete self-sensing model with the two different PLL methods is depicted in Figure O.2.

Concerning tuning of the different loops, the atan2-based MAF-PLL was kept the same as in Table 7.1. Regarding the sine of i_f PLLs, the bandwidth as a function of K_p and K_i calculated using the D-partitioning technique plot shown in Figure 7.4 was used once more. It should be noted that in [8], the authors include an additional constant gain in the expression for the MAF phase detector, which takes into account the mean and differential inductances of the machine. However, as the authors in [8] utilize an IPMSM, the translation of the mean and differential equations to the same values of the separately excited synchronous machine used in the present case is challenging to obtain. Nonetheless, the stability margins that are given by K_p and K_i still holds, with the only difference being in the closed-loop bandwidth.

The summarized self-sensing model parameters is given in Table 7.2.

N	20
K_p (sine of i_f based MAF-PLL)	525.2
K_i (sine of i_f based MAF-PLL)	618
K_p (atan2 based MAF-PLL)	225.4
K_i (atan2 based MAF-PLL)	1249
K_p (Feedback loop)	$7.0715 \cdot 10^{-3}$
K_i (Feedback loop)	$1.1747 \cdot 10^{-3}$

Table 7.2: Summarized self-sensing model parameters

7.5 Finalized results for torque-controlled operation

With the self-sensing model parameters set as shown in Table 7.2, several simulations were run with varying torque steps trough zero. It is clear from the previous simulations that the most challenging region for estimation is at zero-crossing, with the faster the speed

through zero, the higher the estimation error.

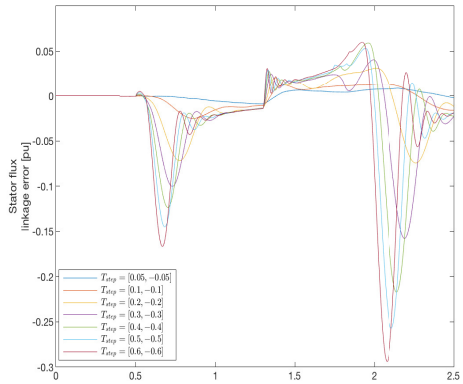

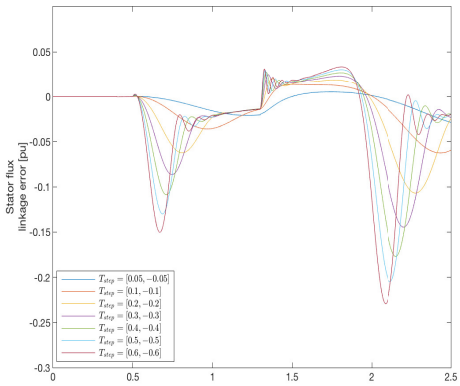

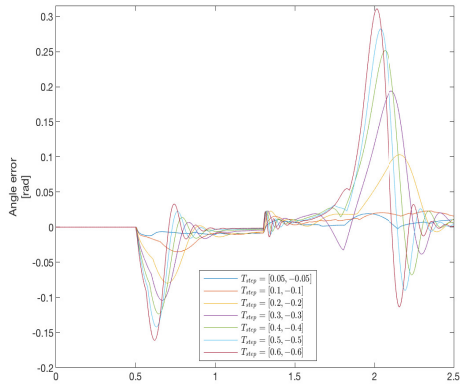

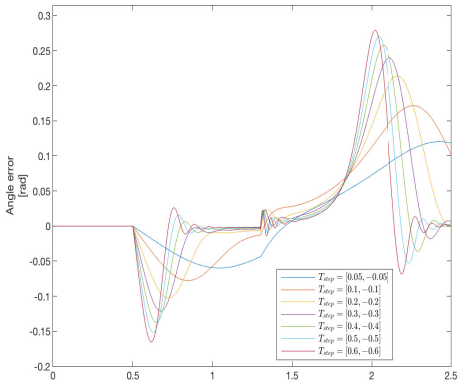

Figure 7.6: Stator flux linkage and position error under sensorless control utilising the self-sensing, current and voltage model for varying steps in torque

Figure 7.7: Stator flux linkage and position error under sensorless control utilising the current and voltage model for varying steps in torque

The conjecture of the relation between a faster speed, i.e. a higher slope or derivative of the speed, through zero, the higher the error in the output estimation from the self-sensing, current and voltage model, henceforth denoted as SSCMVM, is reflected in Figure 7.6. A higher torque step through zero is correlated to a higher speed derivative through zero, and it is seen that as the magnitude of the torque step is reduced so is the peak error for both

stator flux linkage and position estimates. This correlation is especially marked for the SSCMVM model, having a substantially more robust declination of peak error compared to the CMVM model. It should be noted that the robust declination also works the other way, meaning that the SSCMVM model is significantly more sensitive to estimation errors at higher speed derivatives through zero. The sensitivity to a higher speed derivative through zero is reflected in Figure 7.6 and 7.7, wherein it can be seen that the peak estimation error for the SSCMVM model is higher for the two highest step-changes in torque, with the highest position error for the SSCMVM model at 0.3113 rad or 17.84°and 15.98°for the CMVM model, an increase in estimation error of 11.62%. The sensitivity is even more noticeable concerning the stator flux linkage estimation, wherein the peak error is given at -0.2942 pu and -0.2275 pu for the SSCMVM and CMVM model respectively, an increase of 29.32%.

Nevertheless, while the peak estimation errors for the SSCMVM model is higher for the largest step-changes in torque, for each reduction in the magnitude of the step-change and consequently the magnitude of the speed derivative through zero, the peak error is declining substantially faster for the SSCMVM model. As shown for the lowest step change of 0.05 pu, the peak error is reduced by approximately 83.92%, 1.11°for the SSCMVM model compared to 6.89°for the CMVM model.

The same behaviour is also shown for the initial ramping up of torque, wherein the SSCMVM model outperforms the CMVM model substantially for the lower torque step magnitudes, with the lowest step-change in torque resulting in a reduction in position estimation similar to that of the zero-crossing at 80%. It can be seen that for the torque steps in the range of 0.05 to 0.1 pu, the position error for the CMVM model has insufficient time to stabilize itself around zero, causing a longer stretch of erroneously estimated position at the onset of the step-change through zero. The same prolonged state of erroneous estimation is noticeable for all torque references. However, as SSCMVM model is prone to a larger negative overshoot, some of the same tendency is present in this model. Yet, given the fact that the overshoot goes into an underdamped response centred around zero means that in overall the SSCMVM is in a lower error state than the CMVM model.

Concerning stator flux linkage estimation, it is clear that SSCMVM model's sensitivity to a large speed derivative through zero-crossing is more marked than for the position estimate. While at the initial ramping up of the speed no significant increases in error are noted compared to the CMVM model, the error in stator flux linkage error is significantly higher for the SSCMVM at the onset of the speed zero-crossing for the highest torque references. As a result, the effect of the self-sensing, current and voltage model is less marked for the stator flux linkage estimation. However, as the magnitude of the speed derivative approaches zero, so does the efficacy of SSCMVM model increase. As can be seen from Figure 7.6 and 7.7, the peak error in stator flux linkage from the SSCMVM model outperforms the CMVM model for torques equal to and less than 0.2 pu. For the step trough zero from 1 pu to -1 pu, the peak error has been reduced by 25%, meanwhile achieving a constant lower error across the duration of the simulation.

In summation, the self-sensing, current and voltage model combination has been proven to improve both position and stator flux linkage estimation in cases when the speed derivative through zero is sufficiently small enough for the SSCMVM model to overcome its sensitivity.

The SSCMVM model's sensitivity to a high speed-derivative through zero harkens back to the discussion on the loss of synchronicity for the PLL. Given the ever-present duality of dynamic performance and good filtering, the sensitivity of the SSCMVM model is most likely the result of the PLLs insufficient ability to latch on the incoming signal when the speed derivative and consequently frequency is too high. Even for very low frequencies, the PLL takes some small amount of time to latch on to the incoming signal. This small time interval without a locked phase will then necessarily prove too large when the frequency is sufficiently out of bounds for the PLL bandwidth. Furthermore, the fact that the SSCMVM model significantly outperforms the CMVM model, the lower the speed derivative through zero becomes, aligns with the knowledge on back-EMF based identification methods. Both the voltage and current model are heavily reliant on the generation of back-EMF to be able to obtain accurate position estimates. The slower the speed derivative through zero, the larger the period without sufficient back-EMF information becomes. The self-sensing model being solely reliant on the connection between the additional field excitation signals and its response in the stator windings, is then necessarily a much better candidate for low back-EMF information operation, explaining the SSCMVM model's drastic decrease in estimation errors in this operating region.

Due to the sensitivity of the SSCMVM model to a high derivative of the speed through zero-crossing, a control structure was implemented with the expressed aim of only running the SSCMVM model at times when it outperforms the CMVM model. The control was implemented by continually calculated the derivative of the speed and comparing it against a set maximum and minimum constant value given by the highest speed derivative achieved for a step in torque from 0.2 pu to -0.2 pu, which was chosen based on all lower steps providing significantly better estimation than the CMVM model.

As discussed for the hand-off procedure between the different loops in the self-sensing model, the process of extracting the speed derivative is challenging due to sudden dips in speed estimate causing large spikes in the derivative, making it difficult to utilize as a benchmark for hand-off procedure. Yet, by using a combination of a first-order lowpass filter with 10 Hz cut-off frequency and a dynamic rate limiter the issue of the spikes were for the most part overcome, with some spikes still present at speed discontinuities. The block diagram for the self-sensing, current and voltage model, with the speed-dependent gain and speed derivative hand-off procedure is depicted in Figure O.3.

With the hand-off procedure dependent on the slope of the speed implemented the SSCMVM model's sensitivity to a high speed derivative through zero has been eliminated. As can be seen from Figure 7.8 for the highest steps in torque and as such highest speed derivatives through zero, the estimation of stator flux linkage and position is governed by the current model, meaning no increased error. For the lower torque steps, the self-sensing and the current model is operating in unison which serves to reduce the error.

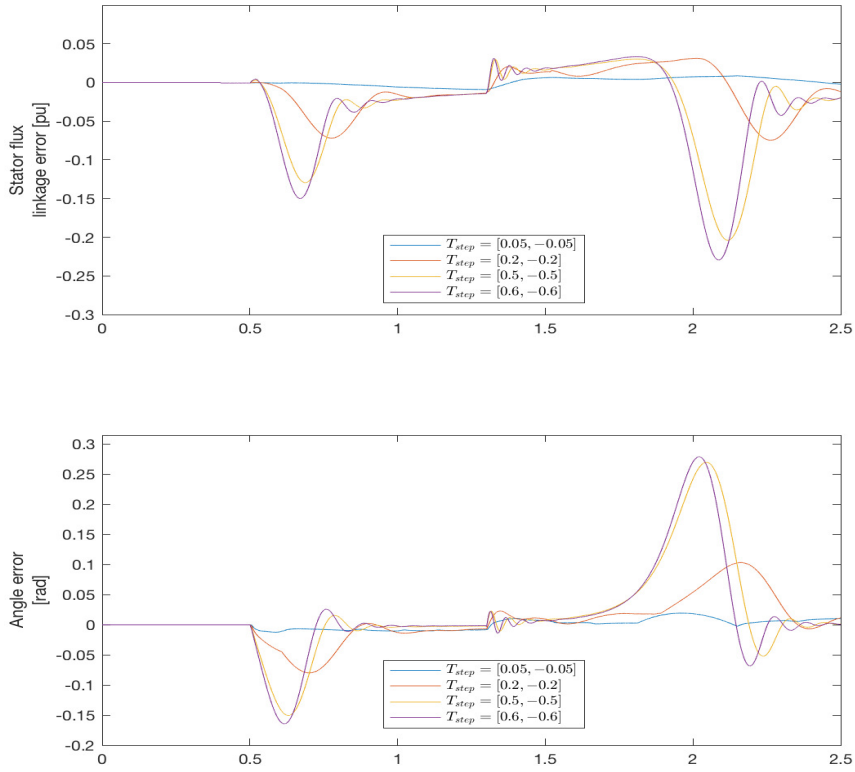

Figure 7.8: Stator flux linkage and position error under sensorless control utilising the self-sensing, current and voltage model for varying steps in torque, with hand-off procedure dependent of the slope of the speed

It should be noted that the hand-off procedure based on the derivative of the speed may prove insufficient for real-world application, due to high sensitivity to errors in the speed estimate. Although the methodology has been proven successful for the simulations, testing on an actual synchronous machine could introduce added error in speed estimate, making the hand-off procedure void. If the machine were to be run under speed controlled regiment, as opposed to the torque control used, the procedure could utilize the applied speed reference to calculate the derivative with no chance of erroneous switching between the current and self-sensing model. However, under a torque control regiment, where no speed reference is available, other procedures may be considered due to the aforementioned sensitivity to small speed errors.

Figure 7.9 shows the results for the SSCMVM combination with the synchronization

failure fixed.

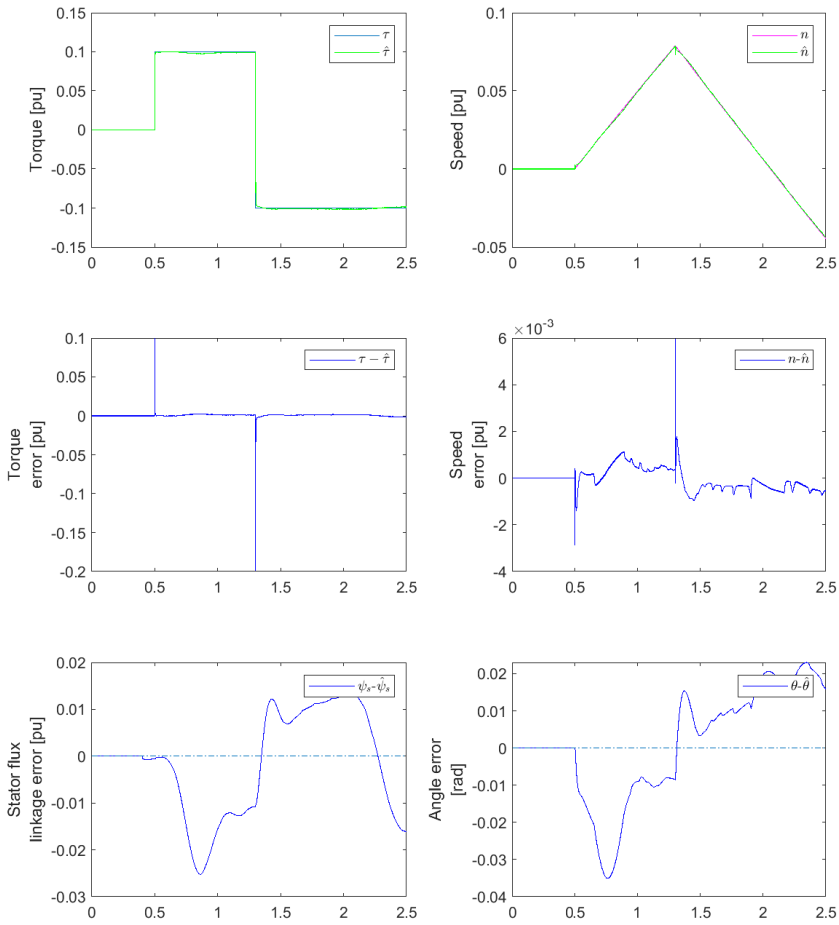

Figure 7.9: Sensorless operation with the SSCMVM combination, with the synchronization failure fixed under torque-controlled operation

Comparing Figure 7.9 with the previous iterations of the self-sensing, current and voltage model combinations it is clear that the combination of the atan2- and sine of i_f based PLLs has reduced the majority of the noise, most notably for the torque and speed error. Further efforts can be taken to increase the settling time for the stator flux linkage and position error, as the relatively rapid changes in torque reference mean that no steady-state is achieved at the first step instance. However, the overall reduction in noise coupled with

the low peak error for the estimates validates the implemented self-sensing methodology.

In conclusion, the combination of the self-sensing, current and voltage model has been proven a viable solution for sensorless operation with torque control enabled. The degree of error reduction at zero crossings for low-speed derivatives points to a more robust position estimate from the self-sensing model than the current model, which is to be expected given the low resolution of the back-emf information at low speeds. The sensitivity to a high speed through zero, which as discussed above is most likely the result of the inherent lack of the PLL to latch on the signal under challenging conditions, was ultimately remedied by the design of a hand-off procedure dependent on the slope of the speed as it approaches zero. While the solution may prove inadequate in the eventuality of physical testing of the sensorless control on the machine, it should suffice for simulation purposes.

Chapter 8

Sensorless operation under speed control

With the self-sensing, current and voltage model combination having been proved efficient for sensorless operation of the synchronous machine under torque-controlled regiment, further investigation into the viability of using the scheme for speed-controlled operation was performed.

The aim of running the machine in speed-controlled mode is to investigate whether the same improvements achieved in estimation for torque-controlled operation is accomplished with the usage of the additional excitation signals utilized in the self-sensing model under speed-controlled operation.

8.1 Tuning of speed controller

As all simulations have been performed under torque-controlled conditions in the present thesis, there are some issues with regard to the speed controller, which will need to be addressed before further investigations can take place.

Initial testing revealed a highly unstable steady-state response in the output from the speed controller, with the addition of a high-frequency harmonic component, both of such magnitudes as to make any meaningful interpretation from the results of the speed-controlled operation investigation impossible. As such, alterations to the controller was needed before further testing.

Concerning the high-frequency harmonics, the introduction of a first-order lowpass filter for the speed error input to the controller designed for a cut-off frequency of 50 Hz served to remove all higher-order harmonics. However, the introduction of the filter means that symmetric optimum, which is the most commonly used tuning method for speed controllers, is no longer valid. Before further tuning, a few key aspects is vital to take into account to achieve the desired response from the speed controller. Firstly, given

that the machine runs in a cascaded control system, with the stator current controllers in the inner loop and the speed controller in the outer loop, the stator current controllers must be ensured faster in order to ensure sufficient time for the speed controller to compensate for loop disturbances. As such, special care will need to be exerted concerning the bandwidth of the speed controller.

Furthermore, as is to be expected, the phase margin of the controller will need to be within the region resulting in stable controller output.

While symmetric optimum may be invalid for tuning the speed controller with the addition of the first-order lowpass filter, the D-partitioning technique discussed in subsection 7.3.1 is the perfect tool to ensure that the two criteria for tuning discussed above are met. Using the D-partitioning technique the controller parameters ensuring stable phase margin are easily calculated, and by calculating the bandwidth from the same parameters, a controller configuration guaranteeing a slower speed- than stator current-controller can be obtained.

The complete open-loop transfer function of the speed-controller is given in Equation 8.1.

$$h_o(s) = \frac{1}{J} \cdot \frac{1}{1+2T_{sum}s} \cdot \frac{1}{1+T_f s} \cdot \frac{1}{s} \cdot K_p \left(1 + \frac{K_i}{s}\right) \tag{8.1}$$

Utilizing Equation 8.1 and the procedure laid out in subsection 7.3.1, and once more aiming for a phase margin of 60°, the calculated bandwidth of the closed-loop speed controller as a function of stable controller parameters is shown in Figure 8.1.

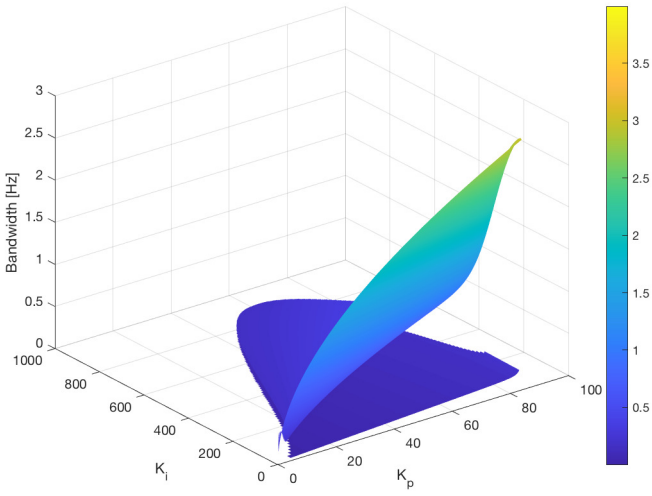

Figure 8.1: PLL bandwidth as a function of K_p and K_i, calculated using the D-partitioning technique for the speed-controller

Initial testing with different tuning configurations with a step applied to the speed reference revealed the need for a substantially lower gain than used with the symmetric optimum, due to a high ripple with speed in steady-state. The lower gain will come at the expense of slower control; however, no useful information could be extracted from Simulink without the significant alteration to the gain. While the slower control will impact the settling time with a step applied to the speed reference as the controller output will take some time reaching the reference, seeing as the remainder of the simulations will be run for speed ramps, the high settling time will not cause undue influence on the results in the present investigation. However, if further work is to be done under speed controlled conditions with steps in speed reference, alterations will be needed to achieve acceptable control.

Concerning the bandwidth of the speed controller, it must be ensured lower than the stator current controller bandwidth set at 16.12 Hz. Using the rule of thumb of one decade lower bandwidth for the speed controller to allow for sufficient time to combat inner loop disturbances and Figure 8.1, the implemented speed controller parameters are shown in Table 8.1.

K_p	54.691
K_i	827.8211
Bandwidth	0.154 [Hz]

Table 8.1: Speed controller parameters

With the controller parameters set as shown in Table 8.1, the ripple in steady-state speed controller was removed, in addition to the controller being able to fully follow speed ramps references as input, with no noticeably slower control. However, as discussed above, the lower gain does result in a slower controller response with steps in speed reference as input.

8.2 Results

8.2.1 Speed-controlled operation under no-load conditions

With the speed controller tuned, simulations were run with varying speed references to discern the efficacy of the self-sensing, current and voltage model combination for different speed-controlled conditions. The aim is to investigate that the same improvements achieved for torque-controlled conditions are noticeable for the speed controlled regiment, as well as increased robustness at holding zero-speed for more extended periods.

The analysis revealed that the overall improvements achieved for torque-controlled conditions, still holds with speed control enabled. The same reduction in peak error was gained for the SSCMVM model for the lower speed derivatives through zero, wherein the current and self-sensing model is operating in unison. Furthermore, it was noted that the slower the speed through zero, the lower the peak error becomes, compared to the CMVM

model. As the resolution of back-EMF information is proportional to the magnitude of the speed, the fact that the SSCMVM model is improving as the slope of the speed decreases does point to improved angle estimation from the self-sensing model in this operating region.
Figure 8.2 shows the results of the speed-controlled operation under no-load conditions. Concerning operation wherein the speed is kept constant zero for more extended periods, it was found that a marked 70% reductions in steady-state error when holding zero speed were achieved for the SSCMVM model compared to the CMVM model.

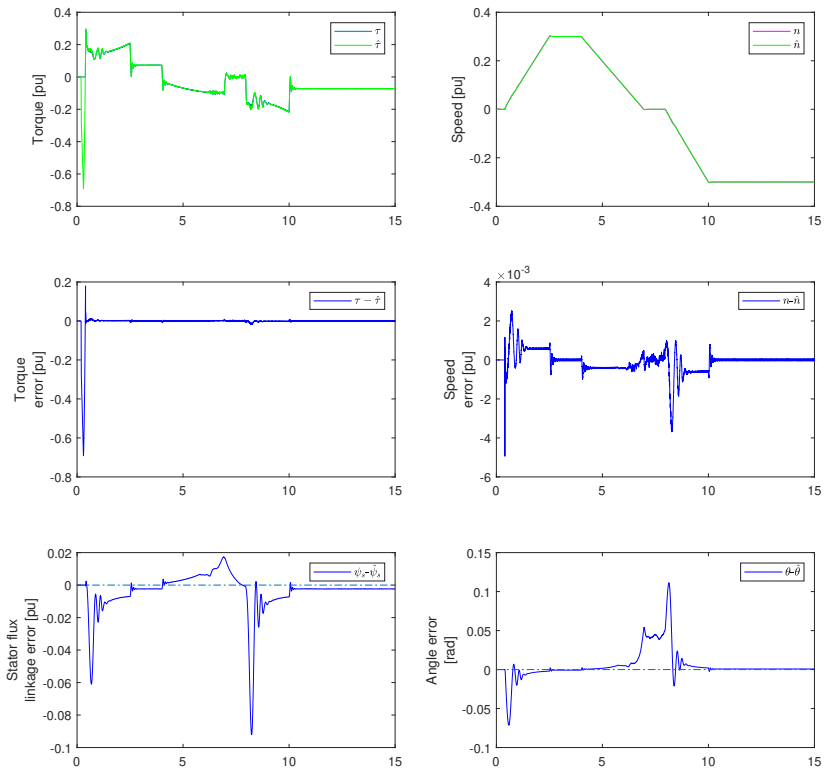

Figure 8.2: Sensorless operation with varying speed reference for the self-sensing, voltage and current model combination, under speed-controlled conditions and no-load

As can be seen from Figure 8.2 there are quite substantial transients at each change of the derivative of the speed, most notably in the flux linkage, position and speed error, which may cause some unwanted drive results, such as increased torque ripple and noise. The increased ripple may come as a result of the quite aggressive tuning of the feedback

PI-controller from the self-sensing to the voltage model, wherein settling-time has been sacrificed for reduced steady-state error.

Conferring with Figure 8.2 shows that the same underdamped is present in all estimates, and further comparison with Figure 7.2, shows an increase in the transients compared to torque-controlled operation, alluding to a connection to the tuning of the speed-controller. Given that the gain of the speed-controller has been drastically reduced to eliminate the noise in its output, the conventional wisdom on controller tuning dictates an increase in the output signal's settling time. As such, further measures concerning the tuning of the speed-controller may serve to mitigate the severity of the transients. Nonetheless, as the aim is to investigate the efficacy of utilizing the additional field excitation signal for standstill and low-speed operation with speed-control enabled, the relatively fast decay of the transients should result in a negligible impact on the present investigation.

8.2.2 Speed-controlled operation under load conditions

Having validated operation in speed-controlled enabled operation for no-load conditions, testing was done with a torque applied at the zenith of the speed reference. This operating scenario is especially challenging for the CMVM model if a high torque is applied to the machine, with a breakdown of estimation capabilities causing the switching of the PWM to lead to complete system failure. As such, the aim is to verify the degree of which utilizing the additional field excitation frequency allows for accurate tracking of the rotor position for this challenging drive condition.

Initial testing revealed that the RMSD calculation used for hand-off between the atan2- and sine of i_f did not function adequately with speed control enabled under load conditions. The issue seemed to stem from the discontinuity at the onset of negative speed, causing erroneous switching between the two models. However, further investigation directly into the self-sensing position output revealed that under the present regiment the atan2-based PLL was able to regain synchronicity for speeds around zero, negating the need for the additional PLL. The ability of loop to regain synchronicity under speed-controlled operation may come as a result of the speed holding constant zero and consequently zero change in frequency in the estimated position signal, allowing time for the PLL to latch on to the incoming signal. Testing with different magnitudes of speed derivatives up to steps in speed from zero to negative speed showed no discernible difficulties for the atan2-based PLL to latch on to the incoming signal, regardless of speed derivatives.

With the atan2-based PLL able to regain synchronicity under to given speed reference, the complexity of the self-sensing model is greatly diminished, seeing as the need for two separate PLL structures are removed.

With the new self-sensing model structure, testing with several different torque values applied to the zenith of the speed reference revealed a substantial improvement at the zero-crossing compared to only running the current and voltage model. Whereas the CMVM model breaks down with regard to estimation of stator flux linkage and position, causing complete system failure, the SSCMVM model was able to provide estimates for the entirety of the simulation. It was noted that for applied torques over 0.85 pu, the SSCMVM

also suffers from the same problems with system failure. However, this is most likely due to the current model being fully initialized before enough back-EMF information is available, which may be remedied by increasing the hand-off speed in the speed dependent gain. However, without testing on a physical machine, it is difficult to recommend any set tuning of the speed-dependent gain which can be utilized for a large swath of different drive characteristics.

Nonetheless, the aim is to present a cursory investigation of the viability of running the synchronous machine in speed-controlled operation using the SSCMVM combination. Given the fact that the model can conclusively perform the necessary estimation processes under conditions where the CMVM cannot serve as a proof of concept for the utilization of the additional field excitation signal for estimation purposes.

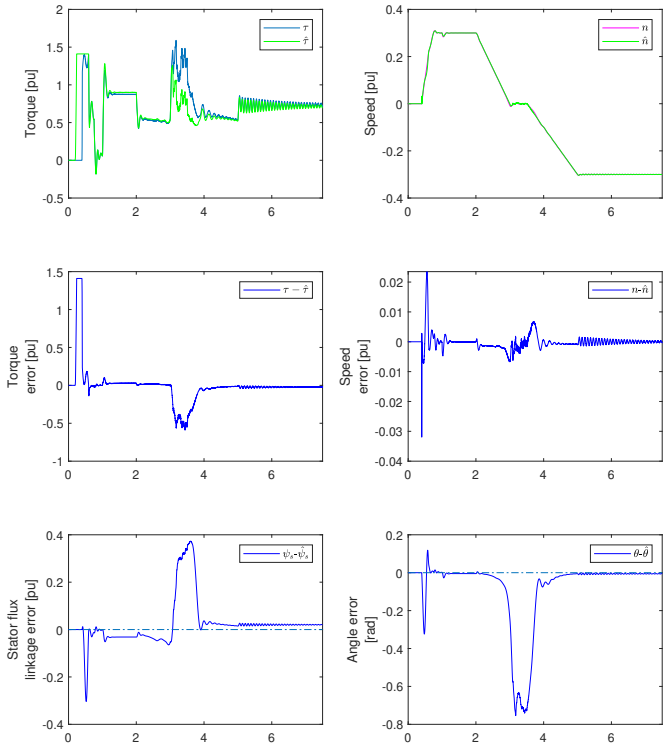

Figure 8.3: Sensorless operation with varying speed reference for the self-sensing, voltage and current model combination, under speed-controlled conditions and applied torque of 0.8 pu

As seen from Figure 8.3, where a torque of 0.8 pu has been applied to the machine after one second, while all relevant parameters are estimated correctly there is a substantial issue concerning the error at constant zero speed, with the error being most marked for the stator flux linkage and position estimates. The peak error of approximately 0.7 rad or 40° for the position estimate suggests that although the SSCMVM can follow the applied speed reference without system collapse, as is the case for a comparative speed reference and applied torque with the CMVM model, there is still significant room for improvement. Testing with a different speed-dependent gain, functioning the same as the previous iteration, with the addition of a dead-time wherein the self-sensing model is operating in isolation, under the assumption of minimizing the current model's influence around zero speed revealed a slight reduction in the peak error across the board. In addition, it was noted that with the new speed-dependent gain, the SSCMVM was able to maintain a higher applied torque through zero. However, seeing as the current speed-dependent gain has been optimized for torque-controlled operation, the need for an additional gain for a different mode of operation will once more increase the overall complexity of the system.

In addition to the sizeable steady-state error in estimated stator flux linkage and position there are substantial oscillations at the onset of steady-state negative speed, most pronounced for the torque and speed estimates. It was found that both the amplitude and decay of the underdamped response is dependent on the amount of torque applied to the machine, with lower torque correlating to a lower amplitude and faster decay. As discussed above, the reduction of the speed controller gain has inevitably lead to increased oscillatory behaviour in the form of underdamped response. While the response was quickly extinguished under no-load conditions, it is clear that under load conditions, the severity of the oscillations has increased manifold. The fact that the oscillations are most marked for the speed, and torque estimates reinforce the assumption of the issue stemming from the speed-controller tuning.

In conclusion, while there is still room for improvements concerning operating the machine under speed-control, the viability of using the additional field excitation signal for sensorless control has been validated. Given the inherent limitations of model-based simulations, there is a clear need for further testing on a physical machine to verify the best method for hand-off between the self-sensing and current model. Furthermore, the fact that the atan2-based PLL is able to regain synchronicity for speed-controlled operation, but not for torque-controlled operation alludes to a possible solution for the method to operate with the ability to regain synchronicity under both modes of operation.

Chapter 9

Discussion

In this master thesis, an investigation into the viability of utilizing the additional field excitation signal for estimation purposes, in what is known as the self-sensing methodology, has been performed. As far as the author is aware, no other research has been done using the self-sensing method for a separately excited synchronous machine with damper windings. By the combination of the self-sensing, current and voltage model it has been proven that the goal of achieving a sensorless control strategy, able to operate in a large array of torque requirements and with a drastic increase in speed control operability has been achieved. The self-sensing model, being entirely reliant on the additional field excitation signal and its response on the stator currents has been shown to diminish the errors in the estimation process at very low-speed and standstill operation, regions of operation wherein the current and voltage model is limited due to a lack of back-EMF information. The main point of contention throughout the investigation has been to acquire a sufficiently efficient method for extracting the necessary information from the field and stator current to allow for the self-sensing methodology to function. Even though a method based on the moving-average filter and phase-locked loop did achieve the goal of utilizing the additional field excitation signal for estimation purposes for both speed- and torque-controlled operation, it is the opinion of the author that the usage of the PLL in itself, while relatively easy to implement, is lacking in the required combination of dynamic range and filtering capabilities. This limitation manifests itself in the enduring problem of resynchronization as the electric frequency of the machine moves in and out of the PLL attuned bandwidth. The same issue is noticeable at the initial ramping up of speed, wherein the PLL is unable to acquire lock-on with a rapidly increasing speed.

While a solution was found, with the stacking of several PLLs operating in different speed regions, the added system complexity may come at the detriment of additional computational costs if the sensorless control strategy is to be implemented in DSP motor-drive. Therefore other methods for extracting the required self-sensing information, such as Kalman filters, may be considered.

The limitations of the PLL notwithstanding, the work has shown that the self-sensing model is highly useful working in unison with the current and voltage model. Compared

to other methods which have been proven to function well at very low-speed and standstill operation, such as high-frequency signal injection, the benefits of using the additional field excitation signal can not be understated. As the signal is naturally occurring due to the feeding of the field converter, there is no need to add signals to the system, which is known to cause increased ripple and harmonics.

The thesis is a continuation of the specialization project completed in December 2019, wherein the foundations for a complete sensorless control regiment were explored. While a cursory sensorless control strategy based on the SRF-PLL with lowpass filter was implemented in the project thesis, with the stator converter disconnected, further investigation in the master thesis revealed severe limitations concerning the range of speeds in which the self-sensing method successfully estimated the rotor position. It was shown that for variations in torque reference of approximately $\pm 10\%$ the SRF-PLL was able to latch on to the incoming signal but applied torques outside this range caused complete desynchronization. The problem was alleviated in the present thesis by the interchanging of the $\alpha\beta$-dq transformation method for the four-quadrant arctangent as input to the SRF-PLL, allowing for a much more comprehensive range of operation. With the atan2 function, the issue of a required unstable closed-loop tuning to achieve the necessary balance between dynamic response and filtering capabilities of the previous iteration was solved, as the new tuning allowed for a broader range of stable controller parameters. While the wider range and the more stable tuning availability did yield an adequate position estimate for continuous mode operation, further testing in discrete operation and comparison with the current model showed that under speed traversal conditions the voltage and current model performed markedly better than the self-sensing voltage model combination. The introduction of the second-order lowpass filter did reduce the error under both standstill and low-speed operation, yet, the inherent limitations of the PLL was ultimately shown to cause a complete desynchronization for higher speed operation with all three models implemented.

The synchronization error may have been foreseen given the PLLs high degree of sensitivity to variations in the acceleration of the rotor. When tuning the controllers and filters of the model, the same torque reference and speed was used for each iteration in order to have a comparative baseline for tuning and RMSD calculation. As such, while a given tuning may prove highly efficient at achieving low steady-state error and reducing the overshoot and the settling time, the lack of a wide dynamic range means that the same tuning regiment may prove lacking under different operating circumstances. By increasing the dynamic range to allow for a wider range of operability, the subsequent trade-off results in a degradation of the filtering capabilities, which in turn leads to more noise in the estimated position. Coupled with the atan2-functions inherent sensitivity to noisy input signals may come some way in explaining the PLLs inability to latch on to the incoming signal at speed zero-crossing, as too much noise passing through the PLL propagates through the control structure feeding back into the atan2-function.

Another possible culprit of the issue of resynchronization may lie in the discretization of the PI-controller and filters of the self-sensing model. It was noted that the ease of implementing the model was significantly greater for continuous mode operation, as

the sensitivity of the tuning was lower. Some of the sensitivity may be explained by the fact that testing in continuous operation was performed with the stator converter disconnected, as the switching of the said converter may cause undue influence on the propagation of the field excitation current. Nevertheless, with the stator converter reconnected the high-frequency components of the field and stator currents showed the required wave envelopes as discussed in section 4.3 with the correct phase-shift obligated for the self-sensing method to function.

Furthermore, while special care was taken when calculating the discretized transfer functions, testing with all available discretization methods in the Matlab suite, it was noted that even minute shifts in the transfer functions gave severe variability in the self-sensing model's estimation capabilities. Consequently, there may be potential for further improvements in the self-sensing model concerning discretization.

With the contradictory requirements for tuning the PLL lowpass filters of a larger bandwidth to accommodate a fast dynamic response and a reduced bandwidth to minimize the high-frequency harmonic elements, the MAF-PLL was implemented to bypass the strenuous tuning of the filter. By using the MAF instead of the lowpass filter, no guesswork is involved in achieving the best tuning as the only unknown variable, N, is directly correlated to the relation between the additional excitation signals in the field current and the sampling rate.

While the MAF-PLL did not solve the resynchronization error, its combination with the D-partitioning technique drastically reduced the complexity of tuning. By only calculating the controller gains which results in closed-loop stability with a set phase-margin, and further calculating its bandwidth, keeping in mind the conventional controller paradigm for optimal tuning, the ease of implementing a robust PLL is drastically improved.

The method was also used for tuning the speed controller, where dual constraints of stable margins and low bandwidth, coupled with symmetric optimum unviable as a tuning regiment, made it the perfect solution to achieve the desired output response quickly.

While the MAF-PLL using the atan2 calculation of the high-frequency stator current did not succeed at solving the issue of resynchronization at speed zero crossing, by bypassing the bandpass filters and instead using the $\alpha\beta$-dq transformation of the stator currents multiplied with the sine of i_f the issue was resolved. As the two separate loops were needed with each phase-shifted 180° in order to account for the change in phase dependent on the slope of the speed, coupled with a high sensitivity to start-up transients meaning the atan2 based MAF-PLL was needed for start-up, the system is in some sense unnecessarily complicated. As previously discussed RMSD calculation is used to decide which loop to give as output continuously, drastically increasing the computational costs of the control strategy. In addition, it was noted under speed-controlled operation that the sine of i_f method was significantly more sensitive to changes in the field and stator currents at zero-crossing, which is natural given that the bandpass filters are used to extract the exact information from the stator responses due to the additional field excitation signals making the atan2 based PLL more reliant on the frequencies of the input signal than the amplitude.

The results achieved under torque-control with the self-sensing, current and voltage

model, has unequivocally shown the usefulness of using the additional signals in the field current for low-speed and standstill. The drastic reduction in error across the board means that the implemented sensorless control strategy is well-positioned for further testing on physical machines. As the self-sensing method was proven sensitive to the slope of the speed through zero, an important caveat is that the gains achieved with the model are dependent on how fast the speed moves through zero. The high degree of sensitivity to the slope of the speed has been deemed caused by the inherent difficulty of the PLL to latch on to the incoming signal when the change in electric frequency is too fast. As the present thesis has looked solely at various PLL structures, it is challenging to decide conclusively whether other methods would allow for lower sensitivity. A great deal of literature point to Kalman filters as a more robust estimation technique allowing for a broader range of operation, which is apparent considering the lack of PI-controller which limits the dynamic range to its tuning. It may, therefore, be beneficial to test other estimation methods in an attempt at reducing the complexity of the self-sensing system. However, given the implementation of the secondary control dependent on the slope of the speed switching from the self-sensing to the current model, and the fact that the higher the slope through zero the shorter amount of time without sufficient back-EMF information for the current model means that the lack of acquisition ability for the self-sensing model is negligible.

Considering speed-controlled operation, it is clear that the presence of the self-sensing model at standstill and low-speed operation has markedly improved the operability of the motor drive. Running comparative simulations with only the current and voltage model showed that not only was the error at standstill and speed zero-crossing drastically diminished, but it was also found that the self-sensing model allowed for significantly higher applied torques without a complete system failure. For applied torques over 0.85 pu, the model did fail even with the self-sensing model; however, this is most likely due to the current model being initialized before sufficient back-EMF information is available. The error in the current model is then of such a magnitude that it permeates the system, affecting all subsequent controllers. Increasing the hand-off speed used in the speed-dependent gain would serve to increase the amount of torque the control system can handle, however; seeing as the hand-off speed has been optimized for torque-controlled operation would mean the need for two separate tuning regiment. It should be further noted that without actual testing on a physical system, it is difficult to recommend a set tuning of the speed-dependent gain, as actual conditions may vary widely.

The same holds for the entire designed sensorless control strategy. While previous research has looked at the influence on changes in machine parameters to the current and voltage model, a sensitivity analysis concerning the self-sensing model is outside the scope of the present thesis. While no evident sensitivity to changes in machine parameters is apparent for the self-sensing model, the method utilized to calculate the stator flux linkage from the position output is dependent on reactances and resistances of the machine, and consequently, changes in machine operation are bound the have an impact on the overall control strategy.

An additional point of interests for speed-controlled operation is the fact that the atan2-based PLL was able to regain synchronicity for the specific speed reference utilized in

the investigation. Given that due to the noise generated at zero-crossing meant that the RMSD hand-off procedure between the different PLLs in the self-sensing model proved inefficient, the ability to only utilized one PLL reduced the overall complexity of the self-sensing model. The atan2-based PLL's ability to regain synchronicity for the given speed reference may hint at the possibility for further action that can be taken with the self-sensing model, to allow for a single PLL to operate regardless of speed- or torque-controlled operation.

A potential limitation in the present study is the fact that in order to simulate the additional field excitation a 300 Hz component with an amplitude of 0.01 has been added directly to the field current. This was done in order to emulate the feeding of the field circuit from a three-phase bridge rectifier. Some preliminary testing forgoing adding the signal directly to the field current, opting instead for implementation of the three-phase bridge rectifier showed a drastic increase in the harmonics of the overall system. However, the self-sensing model was still able to function adequately. An important caveat is that the testing of the self-sensing model took place in continuous operation, and with the sensitivity under discrete operation discussed above, there is sure to be added challenges.

Chapter 10

Conclusion and further work

10.1 Conclusion

In this Master thesis, the goal of achieving a sensorless control strategy for a separately excited synchronous machine with damper windings has been accomplished. The control strategy is based on the novel technique of utilizing additional excitation signals in the field current to estimate the position of the rotor at low-speed and standstill, in what is known as the self-sensing method. When combined with the already established current and voltage models, the control strategy allows for operability of the electric machine in a large array of torque requirements and with a drastic increase in speed control operability.

Concerning torque-controlled conditions it has been concluded that the introduction of the self-sensing model, operating in isolation at standstill and unison with the current model for low-speed operation has drastically improved the resolution of the estimates required for a well-design control system. While the self-sensing model has been noted to be sensitive to the acceleration of the rotor at speed zero-crossing, due to the inherent limitations of the PLL, a control strategy has been implemented to ensure that when the rotor acceleration exceeds the self-sensing model's sensitivity threshold, no undue influence on the estimation process is caused.

With regard to speed-controlled operation the self-sensing, current and voltage model combination has been proven to drastically increase the amount of torque the machine is able to maintain at speed zero-crossing, where comparative tests running only the current and voltage model has shown complete system failure.

10.2 Recommendation for further work

With the foundation of utilizing the additional field excitation signal for estimation purposes explored in the present thesis, further work is warranted testing the sensorless control structure on a physical machine. While the methodology has been proven to work for model-based simulations, testing on a physical machine will give further invaluable information regarding utilizing the self-sensing model for estimation purposes.

In addition, the need for a separate tuning for the speed controlled dependent on whether the machine is run in torque- or speed-controlled operation means that a full sensorless control structure will need to find a balance point for the controller to be able to operate under both schemes.

Furthermore, while the MAF-PLL has been proven as a useful estimation technique, the inherent limitations of the PLL regarding the balance of dynamic response and good filtering thoroughly explored throughout this thesis mean that other estimation techniques, such as Kalman filters, may be explored.

Bibliography

[1] M. Bolstad, "Control of synchronous machines used in ash," Specialisation project, Norwegian University of Science and Technology, December 2017.

[2] R. Nilsen, "Electric drives," NTNU, Compendium 5, 2018.

[3] J. P. Hald, "Sensorless control of synchronous machines," Project thesis, Norwegian University of Science and Technology, December 2019.

[4] F. M. Gardner, "Phaselock techniques," New York, 1979.

[5] D. Uzel, Z. Peroutka, V. Šmídl, T. Košan, and K. Zeman, "Self-sensing control of wound rotor synchronous motor drive for mine hoist," *IEEE Transactions on Industrial Electronics*, vol. 65, no. 3, pp. 2009–2017, March 2018.

[6] R. Nilsen, "Modeling, identification and control of electrical machines," NTNU, Compendium, 2019.

[7] H. Wang, X. Ge, Y. Yue, and Y. Liu, "Dual phase-locked loop-based speed estimation scheme for sensorless vector control of linear induction motor drives," *IEEE Transactions on Industrial Electronics*, vol. 67, no. 7, pp. 5900–5912, 2020.

[8] H. Li, X. Zhang, C. Xu, and J. Hong, "Sensorless control of ipmsm using moving-average-filter based pll on hf pulsating signal injection method," *IEEE Transactions on Energy Conversion*, vol. 35, no. 1, pp. 43–52, 2020.

[9] L. Lia, A. Killingtveit, and M.N.Aas, "Increased generation from upgrading and extension projects," *International Journal on Hydropower and Dams*, vol. 24, 01 2017.

[10] T. Gjengedal, "Application of adjustable speed hydro (ash) machines in the norwegian power system," in *2001 IEEE Porto Power Tech Proceedings (Cat. No.01EX502)*, vol. 2, Sep. 2001, pp. 6 pp. vol.2–.

[11] P. Guglielmi, A. Yousefi-Talouki, G. Iabichino, and G. Pellegrino, "Sensorless direct torque control for pm-assisted synchronous motors with injection high-frequency signal into stator flux reference frame," in *2017 IEEE International Symposium on Sensorless Control for Electrical Drives (SLED)*, Sep. 2017, pp. 139–144.

[12] Baisong Li, Ruixia Ma, Fengchao Fu, Xinhai Jin, and Wei Chen, "A new sensorless control method for brushless permanent magnet dc motors," in *2013 IEEE International Symposium on Sensorless Control for Electrical Drives and Predictive Control of Electrical Drives and Power Electronics (SLED/PRECEDE)*, Oct 2013, pp. 1–7.

[13] F. Wang, S. A. Davari, D. A. Khaburi, and R. Kennel, "Sensorless model predictive torque control for induction machine by using the sliding mode full-order observer," in *2011 Symposium on Sensorless Control for Electrical Drives*, Sep. 2011, pp. 114–117.

[14] M. T. Joy and J. Böeker, "Sensorless control of induction motor drives using additional windings on the stator," in *2018 IEEE 9th International Symposium on Sensorless Control for Electrical Drives (SLED)*, Sep. 2018, pp. 162–167.

[15] J. Hong, S. Jung, and K. Nam, "An incorporation method of sensorless algorithms: Signal injection and back emf based methods," in *The 2010 International Power Electronics Conference - ECCE ASIA -*, June 2010, pp. 2743–2747.

[16] M. Alakula, "On the control of saturated synchronous machines," in *1994 Fifth International Conference on Power Electronics and Variable-Speed Drives*, Oct 1994, pp. 386–389.

[17] D. P. Kothari and I. J. Nagrath, *Electric machines*, 5th ed. Mcgraw Hill Education (India) Private Limited, 2018.

[18] M. Bolstad, "Sensorless control of synchronous machines used in adjustable speed hydro," M.S thesis, Norwegian University of Science and Technology, June 2018.

[19] R. Nilsen, "Modeling, identification and control of electrical machines," NTNU, Compendium, 2019.

[20] T. F. Nestli, "Modelling and identification of induction machines," Ph.D. dissertation, NTH, December 1995.

[21] J. Bergas-Jané, C. Ferrater-Simón, G. Gross, R. Ramírez-Pisco, S. Galceran-Arellano, and J. Rull-Duran, "High-accuracy all-digital resolver-to-digital conversion," *IEEE Transactions on Industrial Electronics*, vol. 59, no. 1, pp. 326–333, Jan 2012.

[22] D. Talbot, *Frequency Acquisition Techniques for Phase Locked Loops*. John Wiley and Sons, Ltd, 2012. [Online]. Available: https://onlinelibrary.wiley.com/doi/abs/10.1002/9781118383285.fmatter

[23] M. Abdelrahem, C. M. Hackl, and R. Kennel, "Finite position set-phase locked loop for sensorless control of direct-driven permanent-magnet synchronous generators," *IEEE Transactions on Power Electronics*, vol. 33, no. 4, pp. 3097–3105, April 2018.

[24] I. Isakov, V. Popović, I. Todorović, S. Grabić, and D. Marčetić, "Application of phase-locked loop in sensorless synrm drives," in *2018 International Symposium on Industrial Electronics (INDEL)*, Nov 2018, pp. 1–4.

[25] L. G. Barbosa Rolim, D. Rodrigues da Costa, and M. Aredes, "Analysis and software implementation of a robust synchronizing pll circuit based on the pq theory," *IEEE Transactions on Industrial Electronics*, vol. 53, no. 6, pp. 1919–1926, Dec 2006.

[26] L. I. Iepure, I. Boldea, and F. Blaabjerg, "Hybrid i-f starting and observer-based sensorless control of single-phase bldc-pm motor drives," *IEEE Transactions on Industrial Electronics*, vol. 59, no. 9, pp. 3436–3444, Sep. 2012.

[27] O. Grøvan, "Identifikasjon og regulering av en synkronmotordrift," M.S thesis, Norwegian University of Science and Technology, June 2004.

[28] M. Talha and I. A. Makda, "Frequency-domain modeling and tustin discretization method based controlling of dc step-up chopper," in *2019 4th International Conference on Power Electronics and their Applications (ICPEA)*, Sep. 2019, pp. 1–5.

[29] Kiam Heong Ang, G. Chong, and Yun Li, "Pid control system analysis, design, and technology," *IEEE Transactions on Control Systems Technology*, vol. 13, no. 4, pp. 559–576, 2005.

[30] X. Xiangshuai, F. Yaojing, and H. Shoudao, "Research on the sensorless control of pmsm based on the improved phase-locked loop and fluctuating high-frequency voltage signal injection method," in *2016 19th International Conference on Electrical Machines and Systems (ICEMS)*, Nov 2016, pp. 1–5.

[31] M. Hypiusová and A. Kozáková, "Pid controller design for magnetic levitation model," in *2017 21st International Conference on Process Control (PC)*, June. 2017, pp. 274–279.

[32] J. Osusky, "Pi controller design method with desired phase margin and settling time," Apr. 2014.

Appendix A

Machine parameters

Table A.1: Machine parameters

Parameter	Symbol	Value
Nominal line-line voltage	U_N	400 [Vrms]
Nominal stator current	I_N	21 [Arms]
Stator inverter supply	$u_{dc,s}$	1050 [Vrms]
Field converter supply	$u_{dc,s}$	500 [Vrms]
Nominal frequency	f_N	50 [Hz]
Triangular carrier period	T_s	1/3000 [s]
Number of polepairs	p	2
Moment of inertia	J	0.58 [pu]
Stator resistance	r_s	0.048 [pu]
Field winding resistance	r_f	0.02 [pu]
D-axis damper resistance	r_D	0.02 [pu]
Q-axis damper resistance	r_Q	0.03 [pu]
d-axis stator reactance	x_d	1.17 [pu]
q-axis stator reactance	x_q	0.57 [pu]
Field winding reactance	x_f	1.32 [pu]
d-axis damper reactance	x_D	1.12 [pu]
q-axis damper reactance	x_Q	0.59 [pu]
Leakage stator reactance	x_σ	0.12 [pu]

Appendix B

Measured and estimated electric angles at standstill

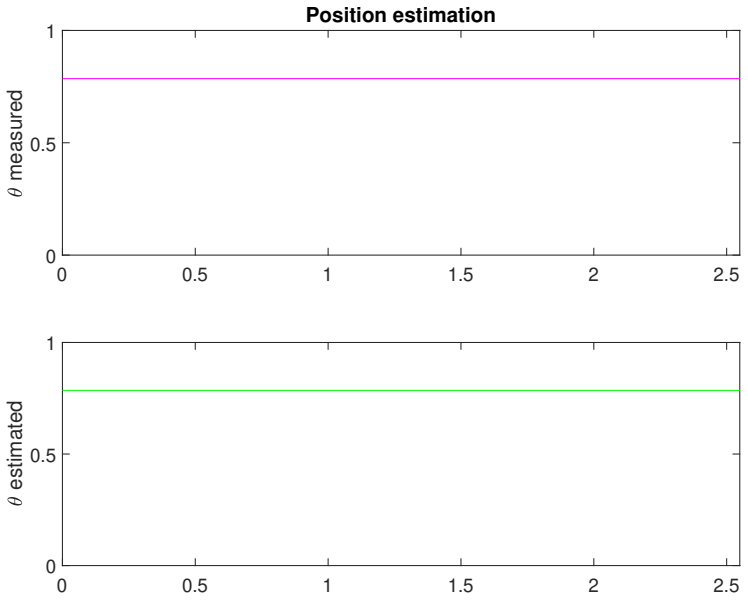

Figure B.1: Measured and estimated electric angles [rad]

Appendix C

Simulink bandpass filters

Bandpass filter $i_{s\alpha}/i_{s\beta}$	$G(s) = \frac{490.1s}{s^2+490.1s+3.553\cdot10^6}$
Bandpass filter i_f	$G(s) = \frac{980.2s}{s^2+980.2s+1.421\cdot10^7}$

Table C.1: Bandpass filter transfer functions for the self-sensing model

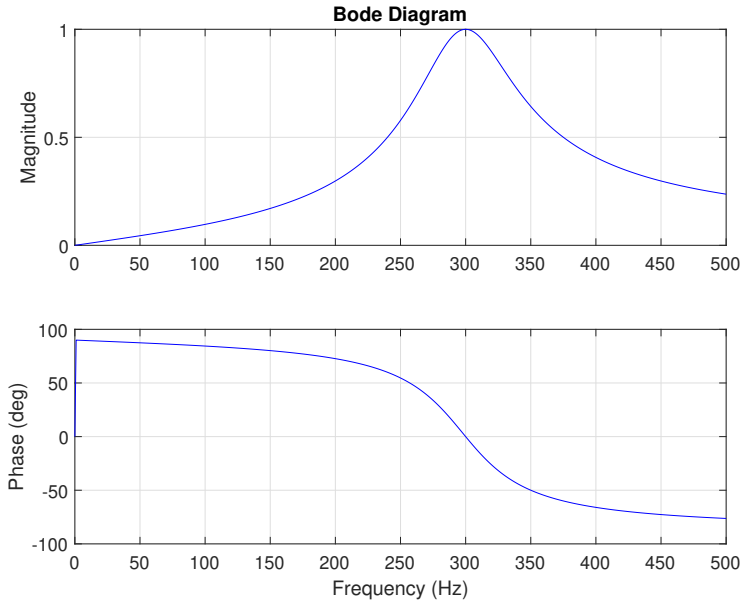

Figure C.1: Magnitude and phase response: Bandpass filter for $i_{s\alpha}$ and $i_{s\beta}$

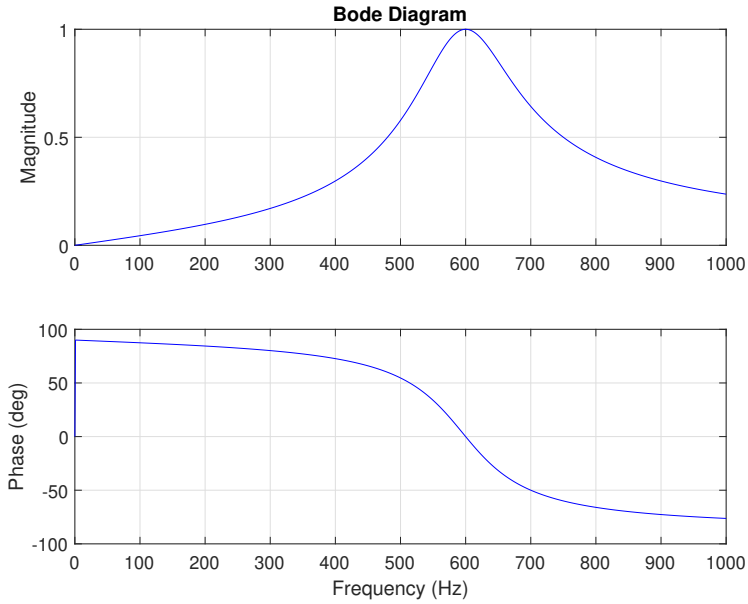

Figure C.2: Magnitude and phase response: Bandpass filter for i_f

Appendix D

Closed loop PLL

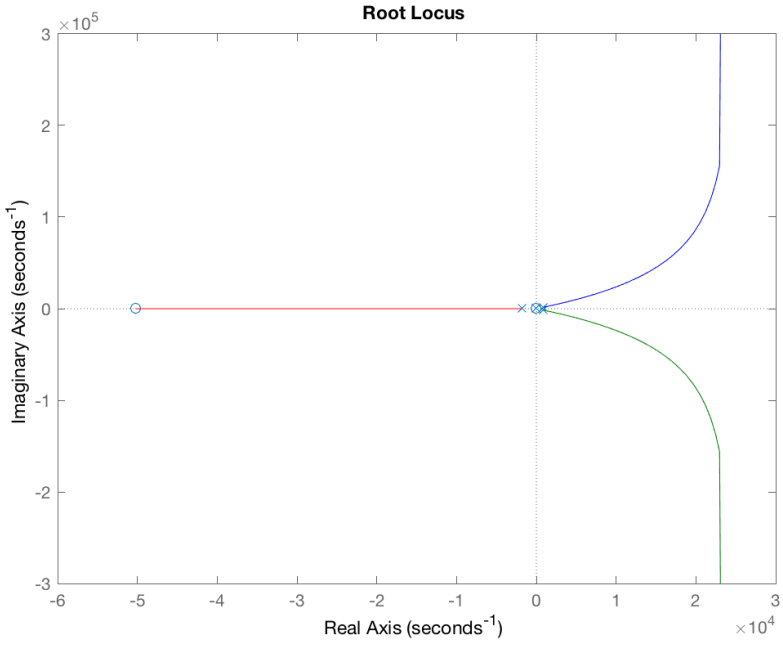

Figure D.1: Root locus plot of closed loop PLL transfer function

Appendix E

SRF-PLL results

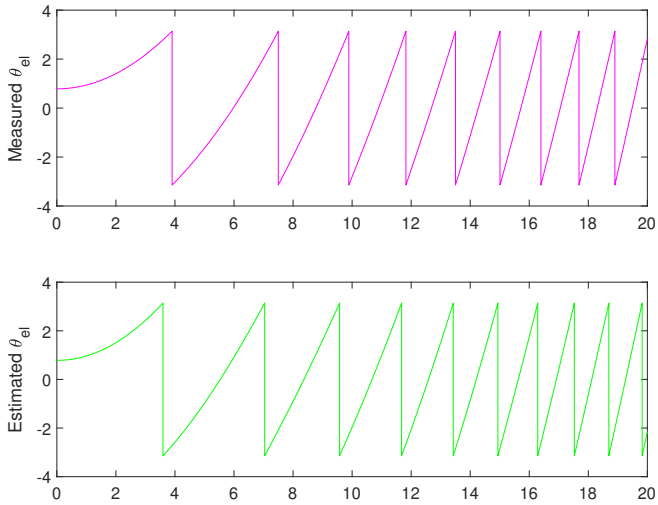

Figure E.1: Measured and estimated electric angles. Torque reference of 0.09 pu

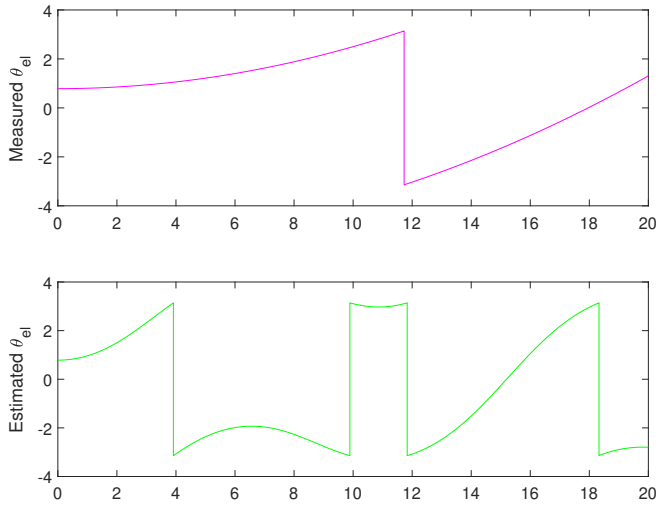

Figure E.2: Measured and estimated electric angles. Torque reference of 0.01 pu

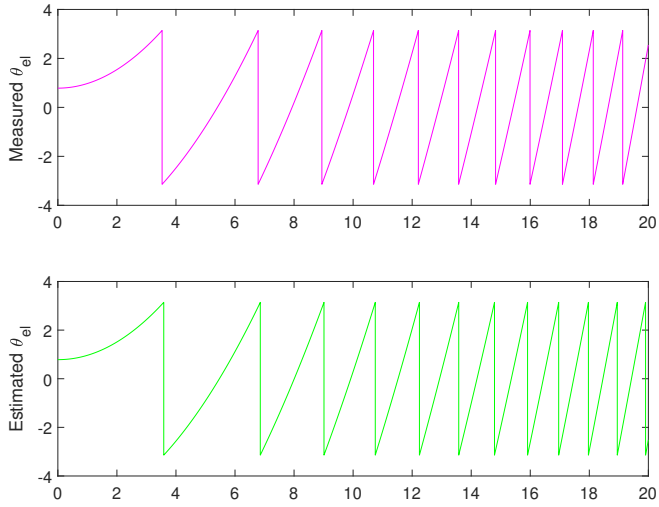

Figure E.3: Measured and estimated electric angles. Torque reference of 0.11 pu

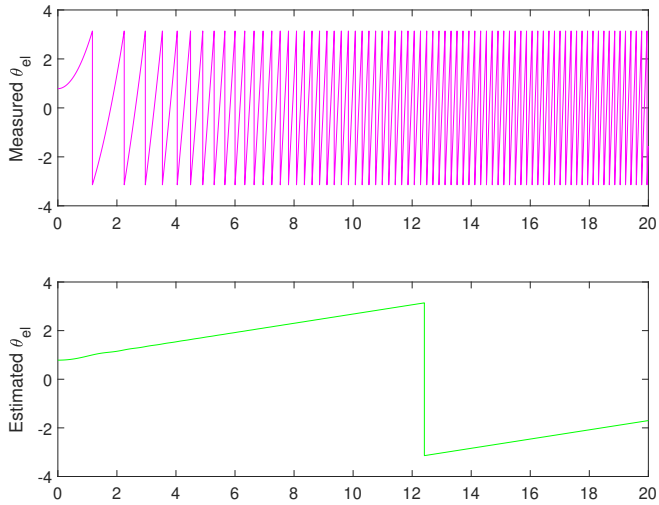

Figure E.4: Measured and estimated electric angles. Torque reference of 1 pu

Appendix F

Alternative pu-model

$$\sigma_{dD} = 1 - \frac{1}{(1+\sigma_d)(1+\sigma_D} \tag{F.1}$$

$$\sigma_{fD} = 1 - \frac{1}{(1+\sigma_f)(1+\sigma_D} \tag{F.2}$$

$$\sigma_{qQ} = 1 - \frac{1}{(1+\sigma_q)(1+\sigma_Q} \tag{F.3}$$

$$r_d^{'} = r_s + \frac{r_D}{(1+\sigma_D)^2} \tag{F.4}$$

$$r_q^{'} = r_s + \frac{r_Q}{(1+\sigma_Q)^2} \tag{F.5}$$

$$r_f^{'} = r_f + \frac{r_D}{(1+\sigma_D)^2} \tag{F.6}$$

$$r_d^{''} = r_s + (1-k_{fD})\frac{r_D}{(1+\sigma_D)^2} \tag{F.7}$$

$$r_f^{''} = r_f + (1-k_{dD})\frac{r_D}{(1+\sigma_D)^2} \tag{F.8}$$

$$k_{fD} = \frac{\sigma_D}{\sigma_f(1+\sigma_D+\frac{\sigma_D}{\sigma_f}} \tag{F.9}$$

$$k_{dD} = \frac{\sigma_D}{\sigma_d(1+\sigma_D+\frac{\sigma_D}{\sigma_d}} \tag{F.10}$$

$$\sigma_d^{''} = \sigma_{dD} - k_{fD}\frac{\sigma_D}{(1+\sigma_d)(1+\sigma_D)} \tag{F.11}$$

$$\sigma_f^{''} = \sigma_{dD} - k_{dD}\frac{\sigma_D}{(1+\sigma_f)(1+\sigma_D)} \tag{F.12}$$

$$\psi_{Rd} = \frac{\psi_D}{1+\sigma_D} \tag{F.13}$$

$$\psi_{Rq} = \frac{\psi_Q}{1+\sigma_Q} \tag{F.14}$$

$$r_{Rd} = \frac{r_D}{(1+\sigma_D)^2} \tag{F.15}$$

$$r_{Rq} = \frac{r_Q}{(1+\sigma_Q)^2} \tag{F.16}$$

$$x_{Md} = \frac{x_{md}}{1+\sigma_D} \tag{F.17}$$

$$x_{Mq} = \frac{x_{mq}}{1+\sigma_Q} \tag{F.18}$$

$$T_D = \frac{x_{Md}}{\omega_n r_{Rd}} \tag{F.19}$$

$$T_Q = \frac{x_{Mq}}{\omega_n r_{Rq}} \tag{F.20}$$

$$u_d = r_d^{''} i_d + \frac{\sigma_d^{''} x_d}{\omega_n}\frac{di_d}{dt} - (1-k_{fD})\frac{r_{Rd}}{x_{Md}}\psi_{Rd} + (1-k_{fD})r_{fD}i_f + k_{fD}(u_f - r_f i_f)n\psi_q \tag{F.21}$$

$$u_q = r_q^{'} i_q + \frac{\sigma_{qQ} x_q}{\omega_n}\frac{di_q}{dt} - \frac{r_{Rq}}{x_{Mq}}\psi_{Rq} + n\psi_d \tag{F.22}$$

$$u_f = r_f^{''} i_f + \frac{\sigma_f^{''} x_f}{\omega_n}\frac{di_f}{dt} - (1-k_{dD})\frac{r_{Rd}}{x_{Md}}\psi_{Rd} - (1-k_{dD})r_{Rd}i_d + k_{dD}(u_d - r_s i_d + n\psi_q) \tag{F.23}$$

$$\frac{d\psi_{Rd}}{dt} = -\frac{\psi_{Rd}}{T_D} + \frac{x_{Md}}{T_D}(i_d + i_f) \tag{F.24}$$

$$\frac{d\psi_{Rq}}{dt} = -\frac{\psi_{Rq}}{T_Q} + \frac{x_{Mq}}{T_Q} i_q \tag{F.25}$$

$$\psi_d = x_d \sigma_{dD} i_d + \psi_{Rd} + x_{Md}\sigma_D i_f \tag{F.26}$$

$$\psi_q = x_q \sigma_{qQ} i_q + \psi_{Rq} \tag{F.27}$$

$$\psi_f = \sigma_{Df} x_f i_f + \psi_{Rd} + x_{Md}\sigma_D i_d \tag{F.28}$$

Appendix G

Discretisation

	Discrete transfer function
Bandpass filter $i_{s\alpha}$ / $i_{s\beta}$	$G(z) = \frac{0.03833z^2 - 0.03833}{z^2 - 1.831z + 0.9233}$
Bandpass filter i_f	$G(z) = \frac{0.0692z^2 - 0.0692}{z^2 - 1.527z + 0.8616}$
Lowpass filter	$G(z) = \frac{0.0052z + 0.0052}{z - 0.9896}$
PI-controller	$G(z) = \frac{14.0533z - 14.046}{z - 1}$

Table G.1: Discretised transfer functions for the self-sensing model

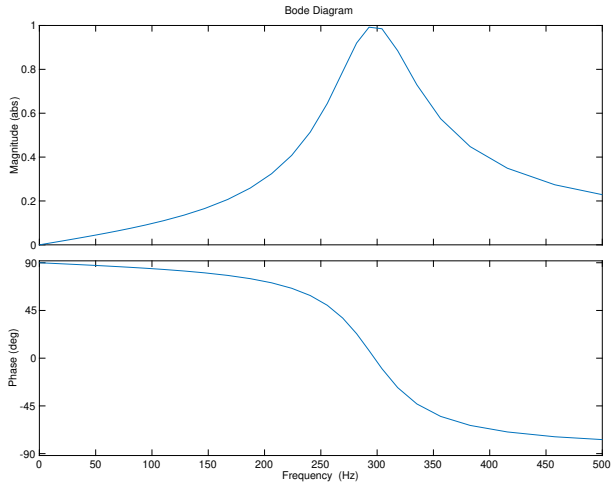

Figure G.1: Magnitude and phase response: Discrete bandpass filter for $i_{s\alpha}$ and $i_{s\beta}$

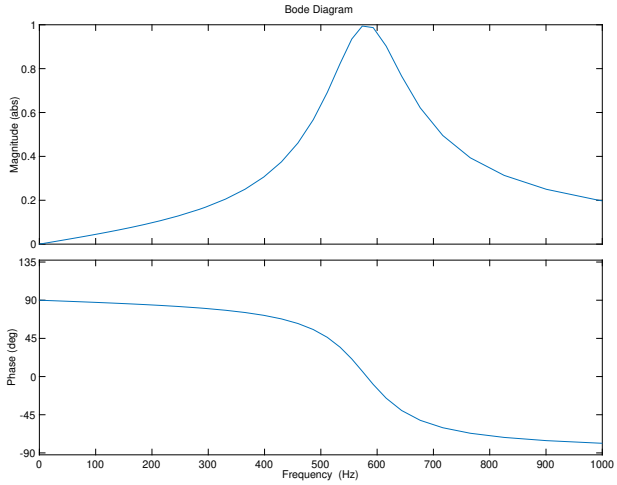

Figure G.2: Magnitude and phase response: Discrete bandpass filter for i_f

Appendix H

Self-sensing method for stator flux estimation

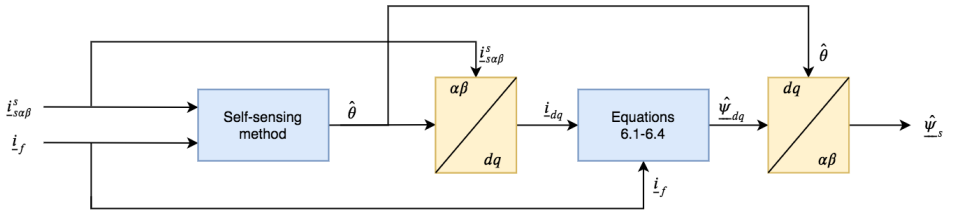

Figure H.1: Model for estimation of stator flux linkage using the self-sensing methodology

Appendix I

RMSD

Table I.1: RMSD calculations for estimated stator flux linkage and position with varying time constant and gain. $\beta = 4/T_f = 10$

P	I	RMSD θ	RMSD ψ
20	0.01	$1.875{\cdot}10^{-4}$	$1.434{\cdot}10^{-5}$
20	1	$1.857{\cdot}10^{-4}$	$1.446{\cdot}10^{-5}$
0.1	1	$8.547{\cdot}10^{-5}$	$7.0318{\cdot}10^{-5}$
0.1	10	$3.630{\cdot}10^{-4}$	$6.614{\cdot}10^{-5}$
0.1	25	$1.053{\cdot}10^{-4}$	$3.831{\cdot}10^{-5}$

Table I.2: RMSD calculations for estimated stator flux linkage and position with varying β-value and lowpass-filter time constant. $P = 20/I = 0.01$

β	T_f	RMSD θ	RMSD ψ
8	$1/(2\pi 10)$	$1.875{\cdot}10^{-4}$	$1.434{\cdot}10^{-5}$
10	$1/(2\pi 10)$	$2.216{\cdot}10^{-4}$	$1.409{\cdot}10^{-5}$
2	$1/(2\pi 10)$	$5.785{\cdot}10^{-5}$	$1.651{\cdot}10^{-5}$
4	$1/(2\pi 10)$	$9.654{\cdot}10^{-5}$	$1.603{\cdot}10^{-5}$
20	$1/(2\pi 10)$	$2.890{\cdot}10^{-6}$	$1.303{\cdot}10^{-5}$
40	$1/(2\pi 10)$	$7.666{\cdot}10^{-4}$	$5.401{\cdot}10^{-6}$
4	$1/(2\pi 5)$	$1.549{\cdot}10^{-3}$	$1.515{\cdot}10^{-5}$
4	$1/(2\pi 1)$	0.0025	$1.836{\cdot}10^{-5}$
4	$1/(2\pi 2)$	$6.116{\cdot}10^{-4}$	$7.938{\cdot}10^{-6}$

Table I.3: RMSD calculations for estimated stator flux linkage and position with varying time constant and gain. $\beta = 20/T_f$=1/(2π10)

P	I	RMSD θ	RMSD ψ
0.01	1	$4.185{\cdot}10^{-4}$	$3.11{\cdot}10^{-5}$
0.01	0.0001	$4.531{\cdot}10^{-6}$	$5.538{\cdot}10^{-5}$
0.003	0.0001	$1.656{\cdot}10^{-6}$	$1.329{\cdot}10^{-5}$
0.004	0.0001	$1.283{\cdot}10^{-6}$	$1.987{\cdot}10^{-5}$
0.005	0.0001	$1.073{\cdot}10^{-6}$	$2.596{\cdot}10^{-5}$

Appendix J

Sensorless control under speed traversal utilising the voltage-current model combination

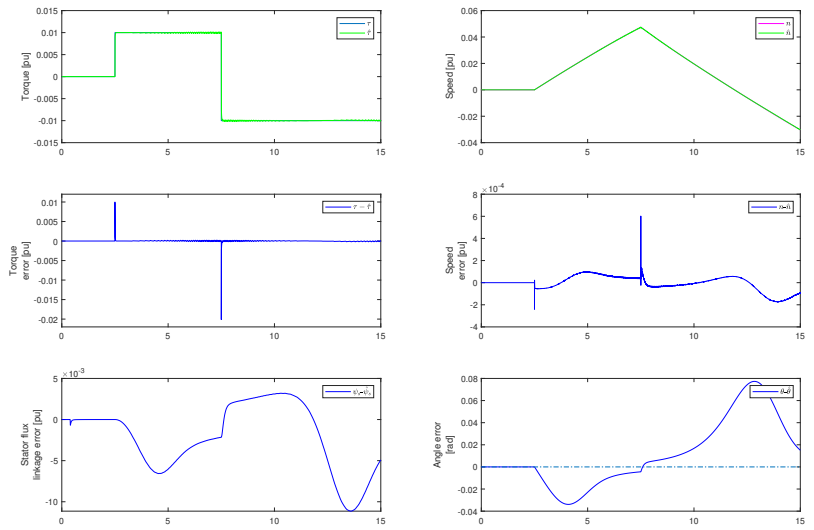

Figure J.1: Sensorless operation with low magnitude varying applied torque reference, voltage-current model combination

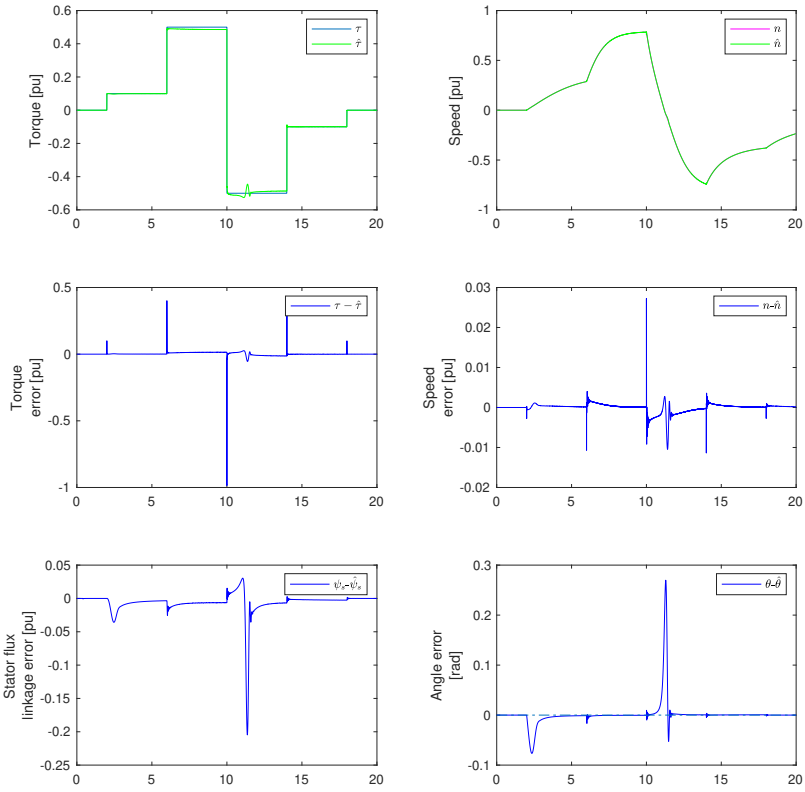

Figure J.2: Sensorless operation with varying applied torque reference for wide speed range operation, voltage-current model combination

Appendix K

Speed Dependent Gain

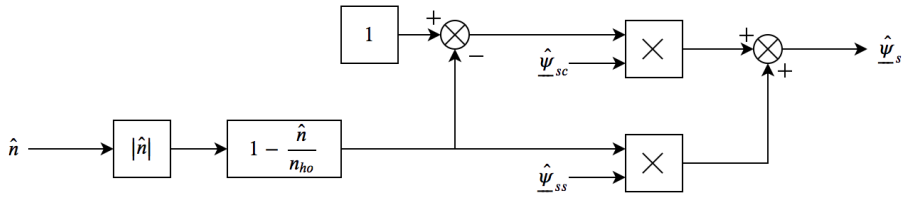

Figure K.1: Block diagram of hand-off procedure from self-sensing to current model, where $\hat{n}$ denotes estimated speed and n_{ho} the hand-off speed from the self-sensing to current model

Appendix L

Dual phase-locked loop

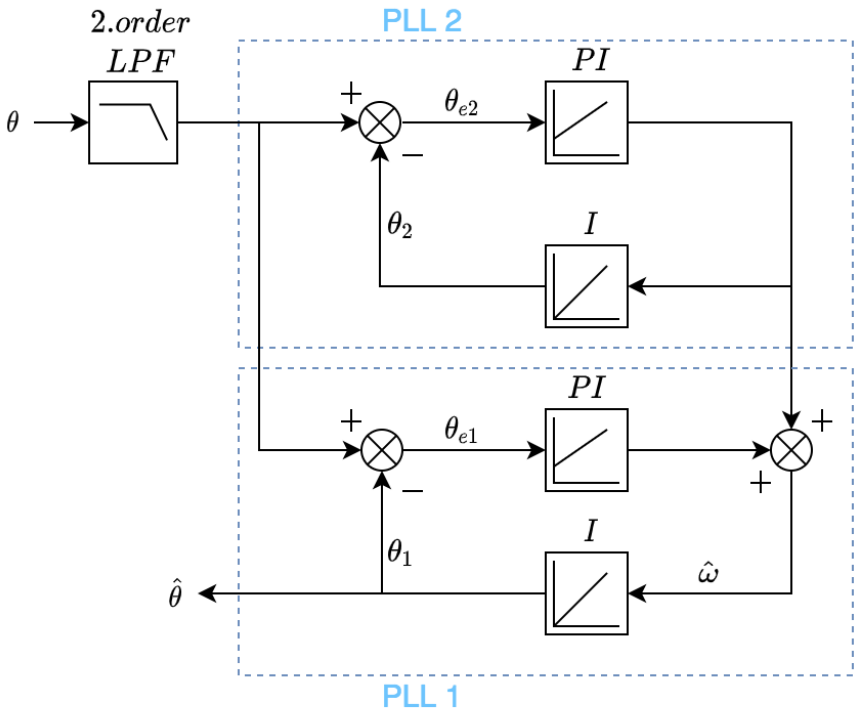

Figure L.1: Dual phase-locked loop. Adapted from [7]

Appendix M

Moving Average Filter

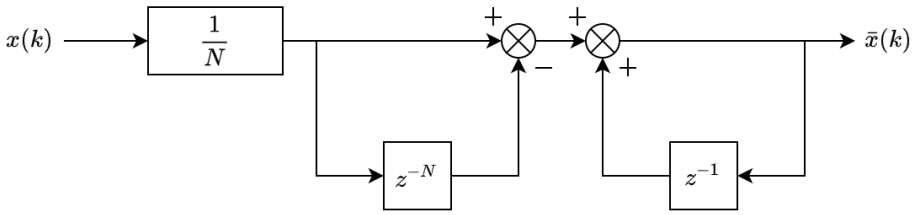

Figure M.1: Moving Average Filter. Adapted from [8]

Appendix N

Bandwidth as a function of controller parameters calculated using the D-partitioning technique

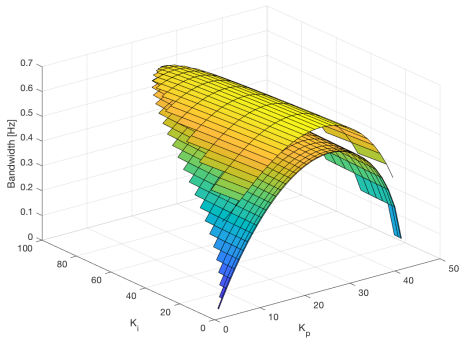

Figure N.1: Bandwidth as a function of controller parameters for FOLPF-PLL, calculated using the D-partitioning technique

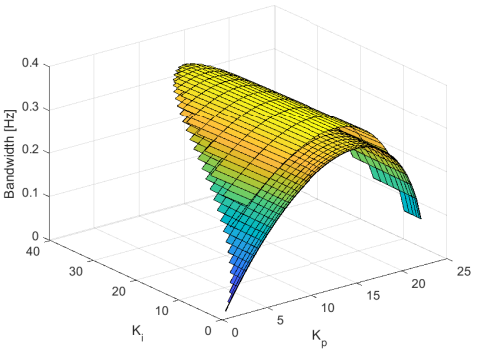

Figure N.2: Bandwidth as a function of controller parameters for SOLPF-PLL, calculated using the D-partitioning technique

Appendix O

Finalized design

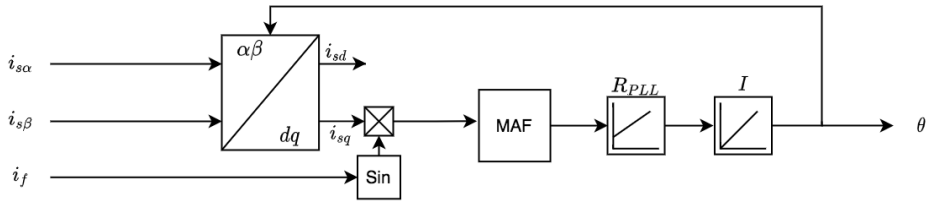

Figure O.1: Block diagram for the MAF-PLL which solves the desynchronization error at speed zero crossing

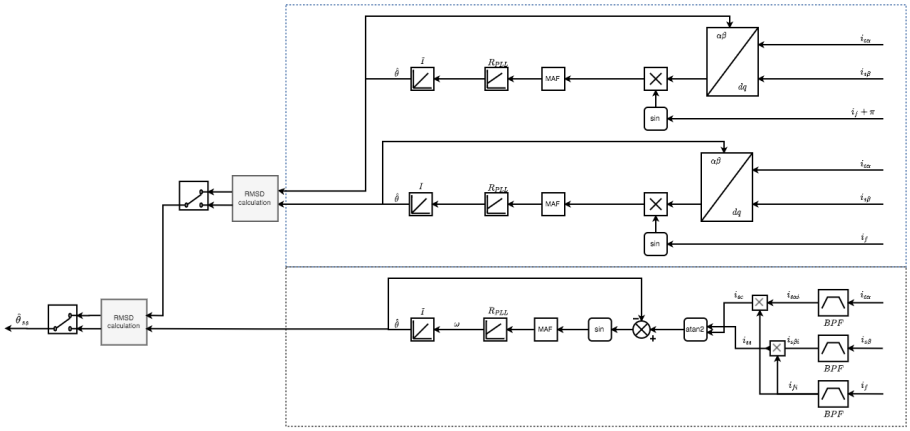

Figure O.2: Block diagram for the full sensing-model estimation methodology

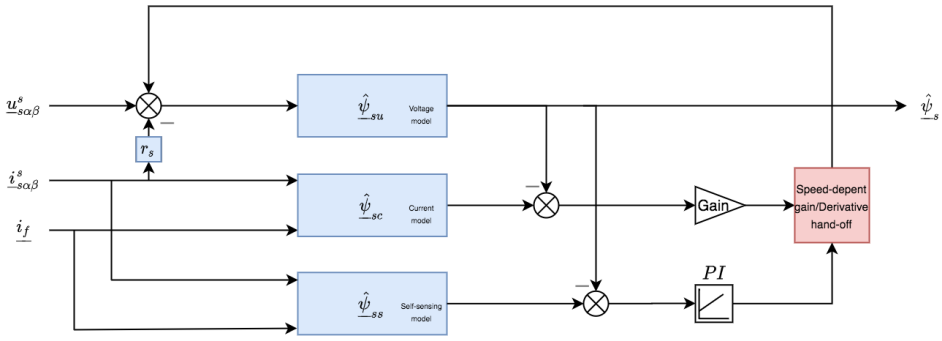

Figure O.3: Block diagram for self-sensing, current and voltage model combination, with the speed-dependent gain and speed derivative hand-off procedure